Upper Ocean Inertial Currents Forced by a Strong Storm*
I: Mixed Layer

ERIC A. D'ASARO

Applied Physics Laboratory, College of Ocean and Fishery Sciences, University of Washington, Seattle, Washington

PIM VAN MEURS, RUSS E. DAVIS, AND P. PETER NIILER

Scripps Institution of Oceanography, La Jolla, California

N00014-90-J-1104

20 December 1993

*Contribution Number ——— from the University of Washington School of Oceanography

ABSTRACT

A strong October storm generated 0.35–0.7 m s^{-1} inertial frequency currents in the 35 m deep mixed layer of a 300×300 km region of the northeast Pacific Ocean. We observed the evolution of these currents for a 23 day period of weak winds following the storm using a combination of 36 surface drifters drogued at 15 m and 3 moorings with acoustic Doppler velocity profilers. We use these observations, plus a CTD survey, to describe the subinertial, geostrophic flow in this same region. We then test whether linear internal wave theory combined with advection by the measured subinertial currents can explain the observed evolution of the inertial frequency currents.

The inertial currents initially have a horizontal scale much larger than the Rossby radius of deformation, reflecting the large horizontal extent and rapid translation speed of the storm. Although this scale is larger than that required for significant linear propagation of the inertial currents, it decreases rapidly, mostly because of the latitudinal variation in f, i.e., β, but modified by advection due to the subinertial currents. Approximately 8 days after the storm, the mixed layer inertial currents begin to decay, reaching half their initial energy in about 12 days. The rate of decay is slightly faster than predicted by linear theory. The observed inertial currents decay to background levels in 23 days, much faster than predicted. Theoretically, the subinertial frequency vorticity should strongly modulate the evolution of the mixed layer inertial motions. This effect should be observable in these data; it is not.

Although the observed mixed layer inertial frequency motions have many of the characteristics predicted by linear internal wave theory, it cannot predict their evolution in detail.

1. Introduction

The famous equations of Ekman (1905) describe how a homogeneous ocean responds to the wind. A steady wind produces a steady response at an angle to the wind stress. An unsteady wind produces both a steady response and velocities that oscillate at the local inertial frequency. Both responses are commonly found within the nearly homogeneous mixed layer of the upper ocean. The steady component is described, for example, by Price et al. (1986), Davis et al. (1981), and Price et al. (1989). The inertial frequency component, which we will call inertial currents or inertial motions, is described by Webster (1968), Pollard and Millard (1970), Pollard (1980), Price (1981), and many others. Usually, these motions are nearly uniform across the mixed layer, reflecting rapid mixing within the mixed layer. This often produces a strong shear across the mixed layer base, where the mixing rate is smaller, and thus significantly affects the mixed layer dynamics. Strong storms commonly produce energetic inertial currents in the mixed layer.

A simple, but very useful, model assumes that the mixed layer velocity is vertically uniform and that the ocean is horizontally homogeneous. Under these assumptions Pollard and Millard (1970) write the momentum budget of the mixed layer as

$$\frac{dU}{dt} + ifU = T - rU \tag{1}$$

where the horizontal current components (u,v) are represented by the complex number $U = u + iv$ and the wind stress components (τ_x,τ_y) by $T = (\tau_x + i\tau_y)/\rho H$. The mixed layer

depth is H and its density ρ. With $r = 0$, this is Ekman's model with an infinite eddy diffusivity within the mixed layer and zero elsewhere. The steady Ekman layer has a velocity $U_E = T/(if\rho H)$. Such a model, however, cannot account for the observed decay of the inertial currents in the absence of continued forcing. Accordingly, Pollard and Millard (1970) added the empirical "decay parameter" r. The resulting model, (1), often makes good predictions of mixed layer inertial currents (Pollard 1980; Thomson and Huggett 1981; Paduan et al. 1989) provided that an appropriate mixed layer depth is used. The decay parameter is not constant, but typically has inverse values in the range of 4 to 20 days. A major goal of this paper is to understand the physics associated with this decay.

Many investigators, starting with Pollard (1970), have proposed that mixed layer inertial currents decay by propagating into the thermocline and deep ocean as near-inertial frequency internal waves. Considerable evidence supports this idea. Observations of near-inertial motions below the mixed layer usually are consistent with dominantly downward-propagating waves (Leaman 1976; D'Asaro and Perkins 1984; Müller et al. 1983) carrying a vertical energy flux comparable to the flux of energy from the wind to mixed layer inertial motions (D'Asaro and Perkins 1984; D'Asaro 1985; Käse 1979). Observations of near-inertial motions associated with both midlatitude storms (Kundu and Thomson 1985) and, in particular, hurricanes (Price 1983; Sanford et al. 1987) commonly show the expected increase in thermocline near-inertial motions and

many of the structural features expected for linear propagation.

Dynamics other than wave propagation has also been been proposed to explain the "decay factor" in (1). Bell (1978) suggests that high-frequency internal waves generated at the base of the mixed layer can transport its momentum into the thermocline. Kroll (1982) proposes a viscous instability of the mixed layer. Others (Smith 1973), despairing that linear dynamics could be made to account for real observations, have concluded that the wind itself is the major agent for both generating and dissipating inertial currents.

The background mesoscale eddy field can also change inertial frequency currents in ways not described by (1). Kunze (1985), for example, shows that mesoscale vorticity ζ acts to shift the Coriolis frequency for near-inertial frequency internal waves from f to $f_{\text{eff}} = f + \frac{1}{2}\zeta$. Subinertial frequency currents can also advect and strain inertial currents.

It has become common to refer to near-inertial frequency motions in the ocean as near-inertial frequency "waves," thus implicitly accepting that wave dynamics controls their evolution. The main goal of our paper is to test this hypothesis.

We analyze the evolution of inertial currents generated by a single isolated storm that passed over the OCEAN STORMS array on 4 October 1987. The oceanographic response to this storm was sampled using a diverse set of instrumentation. High-resolution sampling in depth and time was achieved using a six-element moored array concentrated in the upper 100 m of the ocean, but extending over the full ocean depth; high-resolution sampling in the horizontal and time was obtained using a 36-element

surface drifter array, and high-resolution in three dimensions was achieved using surveys of air-deployed expendable velocity profilers. These data resolve the horizontal and vertical structure of the inertial currents for nearly a month after the storm over a region several hundred kilometers square.

Due to the complexity of the data and analysis, our work is presented in three parts. Part I describes the subinertial flow and the generation and decay of the mixed layer inertial currents. Part II (D'Asaro et al. 1994) describes the propagation of these currents into the thermocline. Part III (D'Asaro 1994a) compares these observations in detail with a nonlinear numerical simulation of flow. Simple dynamical tests on the inertial motions are made in Parts I and II; a direct comparison with model simulations is made in Part III.

Many of the other papers in this volume contain complementary information. Crawford and Large (1994a,b) describe the wind field, the associated generation of the mixed layer inertial currents, and the resulting upper ocean mixing. Zervakis and Levine (1994a,b) and Qui et al. (1994) use a subset of the data presented here to test the dynamics of the inertial motions. Matear (1993) has described the low-frequency motion. Paduan and Niiler (1993) have described the mixed layer low-frequency motions and the mixed layer heat budget.

2. Theory

a. Linear wave theory

We consider the inviscid, linear response of a horizontally uniform, flat-bottomed ocean following Gill (1984) and D'Asaro (1989). A strong storm accelerates inertial currents in the mixed layer in a time that is short compared with the near-internal frequency wave propagation time. At time $t = 0$, the horizontal velocity is $U(x,y,t)Z(z)$. For times $t > 0$ the wind stress is zero.

Gill (1984), Kundu and Thomson (1985), and Eriksen (1988) show that the barotropic response to a fast moving storm is weak, so we considered only the baroclinic, near-inertial frequency response. The initial velocity profile is expanded in terms of the hydrostatic baroclinic modes of the stratification, $p_n(z)$:

$$Z(z) = \sum_{n=1}^{\infty} \sigma_n p_n(z) , \tag{2}$$

where $p_n(z)$ is the eigenfunction of the n^{th} mode. Defining a complex velocity U as in (1), the solution to the linear equations is also written as a sum of modes,

$$U(x,y,t) = \sum_{n=1}^{\infty} \tilde{U}_{In}(x,y,t) p_n(z) e^{-if_0 t} , \tag{3}$$

where $\tilde{U}_I$ is the amplitude of the inertial component of mode n and f_0 is the inertial frequency at a reference latitude. Smith (1973) and D'Asaro (1989) analyze the linear equations of motion under the assumption that U_{In} varies slowly compared with f^{-1} and find a simplified equation that governs its evolution:

$$\frac{\partial \tilde{U}_{In}}{\partial t} = i\frac{c_n^2}{2f_0}\nabla^2 \tilde{U}_{In} + i(f(y) - f_0)\tilde{U}_{In} . \tag{4}$$

Equation (4) filters high-frequency gravity waves from the equations of motion. On an f-plane, or locally in a WKB sense, (4) produces the familiar dispersion relationship for near-inertial motions.

$$\omega_n - f = \frac{c_n^2}{2f}\alpha^2 , \tag{5}$$

where ω is the frequency, c_n is the modal phase speed, and $\alpha^2 = k^2 + l^2$, where k and l are the horizontal wavenumber components.

The initial stages of wave propagation can intuitively be described by "inertial pumping" (Price 1983; Gill 1984; D'Asaro 1989). The divergence of the inertially oscillating mixed layer currents produces an oscillating vertical displacement of the mixed layer base. This results in oscillating pressure gradients in the thermocline and accelerates inertial currents at depth. The rate of energy transfer depends on the horizontal scale of the mixed layer inertial currents, as expressed by the ∇^2 term in (4). Small-scale inertial currents propagate more rapidly than large-scale inertial currents.

Mathematically, it is more convenient to describe the evolution of the mixed layer inertial currents using the normal mode expansion (3). Gill (1984) derives a simple expression for the rate of decay of mixed layer inertial currents. He considers the case in which the mixed layer inertial currents at $t = 0$ vary sinusoidally:

$$\tilde{U}_I(x,y,0) = \tilde{U}_0 e^{i(kx+ly)} \tag{6}$$

The modal amplitudes are

$$\tilde{U}_{ln}(x,y,0) = \sigma_n \tilde{U}_0 e^{i(kx+ly)} . \tag{7}$$

Each mode has a different frequency given by (5), so its phase relative to a pure inertial rotation is

$$\theta_n(t) = \frac{c_n^2}{2f}\alpha^2 t . \tag{8}$$

Since c_n decreases with n, the low modes have the highest frequency and rotate fastest. Gill (1984) defines times

$$t_n = \pi \frac{f_0}{\alpha^2 c_n^2} \tag{9}$$

for which $\theta_n = \frac{1}{2}\pi$. At time t_1, the first mode has rotated 90° and the amplitude of the mixed layer inertial current is reduced from U_0 to about $(1-\sigma_1)U_0$.

This can also be understood in terms of group velocity. The horizontal group speed of the n^{th} mode is

$$G_H = c_n^2 \frac{\alpha}{f} . \tag{10}$$

At time t_n the mode has propagated a distance

$$\Delta = \frac{\pi}{\alpha} , \tag{11}$$

or half a wavelength. Thus at time t_n, the mode has begun to propagate away from its initial location. The initial decrease in mixed layer inertial current amplitude at time t_1 is therefore not restored at later times.

These results can be simply summarized following Gill (1984); mode n separates in phase from the higher modes near time t_n and begins to propagate away from its generation region. Thus at time t_1 the effect of the lowest mode disappears from the mixed layer and the mixed layer velocity decreases to a fraction $1-\sigma_1$ of its initial value. Similarly, at time t_2 the amplitude decreases to $1-\sigma_1-\sigma_2$, and so on.

Mixed layer inertial currents are not generally sinusoidal as assumed above. Below, we will generalize these relationships to allow direct comparison of the above theory with our data.

b. Subinertial current effects

Equations (4) and (5) show the critical dependence of the linear propagation rate on the horizontal structure of the mixed layer inertial motions. Mesoscale subinertial currents can play a large part in determining this structure, as described, for example, by Kunze (1985). We therefore analyze this effect by scaling the equations governing the evolution of mixed layer inertial currents in a way appropriate for our data.

Consider a vertically uniform mixed layer of depth H with near-inertial frequency currents (u,v) of typical magnitude $\hat{u}$ and scale $\hat{l}$ superimposed on a mesoscale eddy field with velocities $(\overline{U},\overline{V})$ of typical magnitude $\hat{U}$ and scale $\hat{L}$. For our data, $\hat{L}$ is comparable to the Rossby radius of deformation (20–30 km). In contrast, the wind-generated inertial currents initially have a much larger horizontal scale, set by the wind, of many hundreds

of kilometers. Thus $\hat{l} >> \hat{L}$. The wind-generated inertial currents have amplitudes of 35–70 cm s^{-1}, much larger than the typical mesoscale currents of 5 cm s^{-1}, so $\hat{u} >> \hat{U}$, but $\hat{U}/\hat{L}$ is comparable to $\hat{u}/\hat{l}$. Under these conditions, the Boussinesq horizontal momentum equations for (u,v) are

$$\frac{Du}{Dt} + \mathbf{u}\cdot\nabla_H \bar{U} - fv = \rho_0^{-1}\frac{\partial P}{\partial x} + \frac{\tau_x}{\rho_0 H} \tag{12a}$$

$$\frac{Dv}{Dt} + \mathbf{u}\cdot\nabla_H \bar{V} + fu = \rho_0^{-1}\frac{\partial P}{\partial y} + \frac{\tau_y}{\rho_0 H} . \tag{12b}$$

Averaging over an inertial period, we can rewrite these as

$$\frac{\partial U}{\partial T} + \bar{\mathbf{V}}\cdot\nabla U + if_{\text{eff}}U = T + \hat{P} , \tag{13}$$

with complex notation for the mixed layer velocity U as in (1),

$$f_{\text{eff}}(x,y) = f(y) + \tfrac{1}{2}\zeta(x,y) , \tag{14}$$

and the subinertial vorticity is

$$\zeta = \frac{\partial \bar{V}}{\partial x} - \frac{\partial \bar{U}}{\partial y} . \tag{15}$$

All linear wave propagation effects act through $\hat{P} = (P_x + iP_y)/\rho_0$.

The subinertial velocity field shifts the effective inertial frequency to $f_{\text{eff}}(x,y)$ and advects the inertial currents, thus Doppler shifting their frequency, straining their spatial structure, and changing their wavenumber spectrum. We will attempt to find these effects in our data.

3. Data

a. CTD profiles

A grid of 34 CTD stations was made at the OCEAN STORMS site from 30 September to 7 October from the CRV *Parizeau*. Measurements were made with a Guildline 8705 CTD, calibrated by water samples (Tabata et al. 1988). Most stations were to a depth of nearly 1500 dbars. The CTD salinity was corrected using water samples and occasional full hydrocasts analyzed on board. Differences between the calibrated CTD data and the hydrocast data ranged from less than 0.005 psu to 0.02 psu (1 psu = 1‰. This suggests a typical error of 0.01 psu. If constant with depth, this is equivalent to about 0.006 surface dynamic meters referenced to 800 dbars, which is negligible.

b. Near-surface drifters

An array of Argos tracked TRISTAR drifting buoys (Paduan and Niiler 1993; Niiler et al. 1987) drogued at 15 m were deployed starting on day 275 of 1987. A total of 15 were operational by the beginning of the storm on day 277 (4 October). The array grew to 36 drifters by day 282 and contained 35 on day 295.

Niiler and Paduan (1994) describe a model in which these drifters slip downwind relative to the water at 15 m at 0.1% of the 10 m wind speed for moderate and low wind speeds. During the period of interest here, days 278–300 of 1987, the maximum 10 m wind speed was just below 10 m s^{-1} and the vector mean wind speed was about 3 m s^{-1}. The maximum predicted slippage is thus 0.01 m s^{-1} and the vector average is

0.003 m s^{-1}. Almost all of the CTD profiles showed a well mixed layer extending to about 40 m, so we expect little slippage due to shear.

Even for a perfect drifter, the velocities at 15 m should be correlated to the wind due to the presence of wind forced motions at 15 m. Niiler and Paduan (1994) correlate wind stress and drifter motion for 47 TRISTAR-II drifters including the ones used here. The drifter velocity coherent with the wind is 70° to the right of the wind with a magnitude $\tau/\rho f H_{eff}$ for wind stress τ, water density ρ, and an effective depth H_{eff} equal to about 35 m. Using a typical wind stress of 0.05 Pa during the period of interest here, a wind forced flow of about 0.012 m s^{-1} is predicted. The vector average stress of 0.03 Pa would produce an average flow of 0.008 m s^{-1}.

The raw buoy positions obtained from System Argos were demodulated into inertial and subinertial positions and velocities in two ways. The method described by D'Asaro (1992) uses smoothing splines with a smoothing parameter of $4/f$. This was used on only two drifters (Argos ID 7986, 7951). An objective analysis method, described in the appendix, was used on the remaining drifters. The two methods produce very similar results. The average difference in the demodulated inertial component of velocity is about 0.1 cm s^{-1} and the rms difference around this mean is about 2 cm s^{-1}, somewhat less than the estimated rms error in the first method (D'Asaro 1992). The rms difference between the subinertial velocity components computed by the two methods is about 0.5 cm s^{-1}, about 60% of the error in the first method as estimated by D'Asaro (1992).

Spectrally, the objective analysis scheme has a slightly narrower bandwidth and thus roughly 20% less energy for periods of 1.5 to 4 days. D'Asaro (1992) shows that energy in this band can be aliased by the irregular Argos sampling pattern, so the difference between the two schemes is concentrated in the region of most intrinsic uncertainty.

Figure 1 shows the interpolated trajectories for all the drifters. There is clearly a strong inertial component, shown by the clockwise rotating circles, and a smaller subinertial component.

c. Moorings

Velocities from three moorings (central, C; northern, N; and western, W) (Davis et al. 1994) are used here. Their locations are shown in Fig. 1. All contained acoustic Doppler current profilers (ADCP) looking upward from (110 m). An Argos transmitter on the surface float of each mooring was used to remove the mooring motion. Velocity was computed from these data, using the objective analysis scheme described above, and added to the ADCP velocity to form the oceanic velocity. Subinertial velocities were computed using a low-pass Butterworth filter with a 0.4 cpd cutoff. Inertial velocities were obtained by complex demodulating the velocity at a frequency of 1.5 cpd and low-pass filtering the result with the same Butterworth filter.

d. Wind

Wind was measured using a propeller anemometer mounted at 3 m height on the C mooring. Crawford and Large (1994a) describe other OCEAN STORMS wind measurements. Wind stress was computed as in Large and Pond (1981), but with no correction for stratification since it will have minimal effect at the high wind speeds encountered here. We have several reasons to regard these stress estimates with suspicion. First, the logging system was less than ideal: 15 minute average speed and instantaneous direction every 15 minutes. Second, the drag coefficient on short time scales can vary by a factor of 2 over several hours in storms similar to ours (Large and Pond, 1981). Third, comparison with other wind data, from Large et al. (1994), suggests that these wind speeds are low at high wind speed, relative to a 10 m reference, due to wave sheltering. They correct the winds for this effect and thus produce better predictions of mixed layer velocities. We will use these corrected data.

4. Subinertial velocity

a. Measured

The heavy arrows in Fig. 2a show all subinertial velocities from the drifters and moorings from days 280–300. For each record the data have been low-pass filtered using a cubic smoothing spline, with a 4 day smoothing parameter and subsampled every 4 days. The resulting 212 vectors form a consistent flow field, with nearby vectors almost always having similar magnitude and directions. We thus trade temporal for spatial reso-

lution and treat all the data together. These vectors are objectively mapped following Bretherton et al. (1976), assuming that the true velocity field is nondivergent and is characterized by the analytical correlation functions from McWilliams (1976a,b) and Shen and McWilliams (1978). Transverse and longitudinal correlation lengths of 150 km and 40 km, respectively, and an instrumental error of 5% provide a good fit to the data (see appendix). This analysis produces fields of horizontal velocity (Figs. 2a–2d), streamfunction normalized to equal dynamic height at 47.5°N (Fig. 2b), relative vorticity (Fig. 2c), and absolute vorticity $\zeta_A = \zeta + f$ (Fig. 2d). We plot only data for which the mapping error is less than 60%. Most of the domain has a mapping error between 20% and 40%.

Figure 2 shows a subinertial flow that is northward and eastward with embedded eddies. The spatial mean flow is 0.027 m s^{-1} to the northeast, and the rms eddy velocity about this mean is 0.053 m s^{-1}. The vorticity field shows the eddies to be dominantly anticyclonic with an rms vorticity of $0.023f$ and a maximum anticyclonic vorticity of $-0.07f$ at the bottom left of the domain. The strain field (not shown) has smaller correlation spatial scale, about 20 km, but an rms value comparable to vorticity. A large scale straining $\bar{v}_y \approx 0.005f$ is apparent in the rapid acceleration of buoys out of the domain to the north and to the south.

The eddies have a typical scale of about L = 40 km and thus a Rossby number $Ro = U/fL$ of about 0.01. We expect the flow to be geostrophic and nearly nondivergent

as assumed. The vorticity equation appropriate for low Rossby number flow

$$\frac{D(\zeta+f)}{Dt} = -(\zeta+f)\nabla\cdot u \tag{16}$$

implies that $\nabla\cdot u$ is a factor of Ro smaller than the vorticity. However, the streamline and absolute vorticity fields (Figs. 2b and 2d) are well correlated. The residual in absolute vorticity from this correlation is $0.015f$, only slightly above estimated mapping error of $0.013f$. Therefore, ζ_A is constant along streamlines to within the measurement error, and (16) implies $\nabla\cdot u = 0$. The divergence is even smaller than scaling would indicate. The vorticity equation is therefore consistent with our assumption that the subinertial, near-surface flow is steady over 25 days.

b. Geostrophic velocity

CTD data provide a second estimate of the subinertial surface flow. Figure 3 shows contours of surface dynamic height relative to 800 dbars objectively mapped (Bretherton et al. 1976) using a Gaussian correlation function with a 100 km scale (see appendix). The pattern is similar, but somewhat smoother than the dynamic height computed from the velocity data in Fig. 2b. The anticyclonic eddy near the moored array (47.5°N, 139°W) is not evident in the CTD data, probably because it fits between the CTD stations and is thus poorly sampled. The CTD-derived and buoy-derived surface dynamic heights are correlated with $r = 0.9$, a slope of 1.06, and a residual error (1.2 dynamic cm) comparable to the CTD calibration error. For deeper reference levels to 1500 dbars the

correlation is equally good but the CTD-derived dynamic height is too large; for shallower levels to 500 dbars it is too small. The flow in the upper 1500 m is therefore nearly geostrophic with a level of no motion near 8 MPa. Matear (1993) obtains similar results using a full inverse of this data.

The subsurface geostrophic velocities, computed from these dynamic height data, are in nearly the same direction as the surface geostrophic velocity at the same horizontal location; they are reduced in magnitude, however, by a factor that decreases nearly linearly to zero at the reference level. This correlation persists, with opposite sign, to the end of our data at 1500 dbars. The residuals from this correlation are always below 0.02 m s^{-1}. However, the surface geostrophic kinetic energy is only 34% of that measured directly by the drifters. Furthermore, the subinertial velocities measured on the PCM and OSU moorings (Davis et al. 1994) do not show a strong correlation between near-surface and subsurface velocities. This suggests that only the larger-scale subinertial velocity measured by the CTD data is correlated in depth and that the subinertial velocity on scales smaller than 50 km has a more complex vertical structure.

5. The storm

Figure 4 shows the wind stress and the currents predicted from it using (1) with $r = 0$. We choose H = 55 m based on the observed vertical profile of horizontal current measured after the storm (Part II). We define the backrotated inertial current vector as

$$\tilde{U} = \tilde{u} + i\tilde{v} = (u + iv)e^{if_0(t - t_0)} \tag{17}$$

with f_0 equal to the inertial frequency at 47.5°N and t_0 defined as the start of day 278. If u and v were a pure inertial oscillation at this latitude, then $\tilde{u}$ and $\tilde{v}$ would be constant. The inertial speed is $|\tilde{U}|$ and the phase of $\tilde{U}$ corresponds to the direction of the inertial currents at t_0.

The storm on day 277 is the only large wind event in the region during October 1987. The predicted mixed layer inertial currents are about 0.6 m s^{-1}. The winds are weak for the next 25 days, with (1) predicting about 0.1 m s^{-1} change in the inertial current due to the wind, mostly in the sense to rotate $\tilde{U}$ counterclockwise. To first order, we can ignore the wind forcing through about day 298. The wind forcing increases, thereafter, with a large storm occurring on day 309.

A surface isobar chart at 277.5 (Fig. 5) shows the structure of the storm. This was constructed using all available surface wind and pressure measurements and satellite photographs (N. Bond, personal communication, 1990). A cold front rotating around a low to the north of our area moves eastward over the site preceded by a warm front. The main wind shift occurs at the cold front; this is preceded by a smaller wind shift at the warm front. The relative timing of these shifts makes this storm a particularly effective generator of mixed layer inertial currents (Crawford and Large 1994b). From analyses based on satellite imagery and surface reports, the triple point at the junction of the warm and cold fronts translates at 18.5 m s^{-1} toward 63°T. The cold front itself translates

almost due eastward at about 16 m s^{-1}. It is difficult to estimate the errors in these numbers but 2–3 m s^{-1} and 15–20° are reasonable.

6. Inertial currents

a. Maps

Energetic inertial oscillations are obvious in the buoy tracks (Fig. 1). We use drifter 7944 at approximately 48.5°N, 140.4°W as an example. Before the storm (northwest end of track), the buoy drifts southeastward at 4–6 cm s^{-1} with superimposed inertial oscillations of comparable magnitude. Four inertial periods from the start of the track, the inertial oscillations increase dramatically as the storm passes over the buoy. The inertial circle is about 14 km in diameter, implying an inertial velocity of about 0.7 m s^{-1}. The currents remain this large for about 10 days, and then slowly decrease, reaching prestorm levels about 20 days after the storm. A similar pattern occurs at each of the drifters, although those deployed after the storm do not show the prestorm conditions.

For each drifter and mooring, we compute the backrotated inertial current vector (17) as described in section 2. The panels of Fig. 6 show these vectors for days 276–300 at 5 day intervals. The speed and direction contours show the results of objectively mapping these vectors using a Gaussian correlation function with a 90 km scale and 10% measurement error. The correlation scales of the data change dramatically with time, but we have not accounted for this in our mapping.

Before the storm (Fig. 6a) the mixed layer backrotated inertial vectors have a nearly uniform amplitude (0.1 m s^{-1}) and direction. Two days after the storm (Fig. 6b), they are much more energetic (0.35–0.7 m s^{-1}) and still nearly uniform across the array. Clearly the storm has accelerated inertial currents within the mixed layer with approximately the magnitude predicted in Fig. 4. These have a horizontal scale of hundreds of kilometers, comparable to the scale of the storm (Fig. 5), and smaller scale variations.

Between days 280 and 285 (Figs. 6b and 6c), the amplitude of the backrotated mixed layer inertial vectors does not change significantly, but their direction develops a pattern of clockwise rotation toward the north. This pattern intensifies through day 295 (Figs. 6d and 6e) as the amplitude decays. The rate of decay is slowest in the northwest quadrant of the array and fastest in the southeast. By day 300 (Fig. 6f) the mixed layer inertial currents have decayed to nearly their prestorm level. The major goal of this paper is to understand these patterns.

b. Dominant spatial scales

The spatial structure of the inertial currents is easily explained following D'Asaro (1989). The wind stress pattern associated with the storm has a spatial scale large compared with that of the array and moves across the array in a small fraction of an inertial period. Accordingly, the inertial currents generated by the storm have a scale large compared with the array's. If we assume that the inertial currents rotate at the local inertial frequency, but that f varies as $f_0 + \beta y$, then

$$\tilde{U} = e^{i\beta y(t - t_0)} . \tag{18}$$

The north-south wavenumber l decreases as $-\beta t$, while the east-west wavenumber k remains constant. A 180° phase change across a 300 km array will occur in 8 days, in rough agreement with the observations.

More quantitatively, we find the dominant wavenumber of the backrotated mixed layer inertial currents by fitting a single plane wave to the data

$$\tilde{U}(x,y) = \tilde{U}_{\text{fit}} e^{i(kx + ly)} + U_R(x,y) \tag{19}$$

using the algorithm described in the appendix. Here $\tilde{U}_{\text{fit}}$ is the complex wave amplitude, k and l are the wavenumbers, and U_R is a residual. The phase of $\tilde{U}_{\text{fit}}$ is set by referencing x and y to a point near the center of the array (47.5°N, 139.5°W).

Figure 7 shows the parameters of (19) for days 276–300. The number of data points increases from 14 on day 276 to about 40 on day 285. The energy in the fit $E_{\text{fit}} = \frac{1}{2}|U_{\text{fit}}|^2$ (shading) is more than 90% of the total energy E_{tot} through day 290. (There is some imprecision here since E_{tot} is the average of the energies of the irregularly spaced buoys). After day 295, the fit energy is less than half of the total, so (19) does not describe the field well. The uncertainties in the parameter values are indicated by the symbols, which show the results of fitting 40 realizations of a Monte Carlo simulation of the data as described in the appendix. The 2nd and 39th ranked realizations are approximate 95% confidence limits. By about day 297, these become sufficiently large to make the fits nearly meaningless.

Both the total energy and the energy in the fit increase dramatically on day 277 due to the storm. For the next 23 days the energy decreases, slowly at first, then more rapidly; by day 300, $|\tilde{U}_{\text{fit}}|$ is about 0.05 m s^{-1}. The direction of $\tilde{U}_{\text{fit}}$ increases slightly at first, corresponding to a slightly subinertial frequency, and then decreases, corresponding to a frequency of about 1% above f. The horizontal wavenumbers are initially small, corresponding to a wavelength of about 1700 km. They then evolve nearly as predicted by (18); k remains constant within the confidence limits and l decreases as $-\beta t$ (Fig. 7, dashed line). Between days 290 and 200, l deviates slightly from this dependence.

c. Spatial variability

The decay rate of the mixed layer inertial currents is faster in some places than in others (Fig. 6). We therefore define four geographical subregions (NE, NW, STH, CL) in Fig. 1, each containing a subgroup of drifters and moorings. For each region, we fit (19) and display the fit parameters in Figs. 8–11. Statistically significant variations between these regions are apparent. The inertial currents are most energetic in NW and least in STH. They decay faster in CL and NE than in NW. Similarly, l is less negative in NW and more negative in CL; it decreases fastest in STH and slowest in NE.

7. Dynamical tests

a. Storm forcing

The storm on day 277 generates inertial currents in the mixed layer. The slab model (1) using the winds at mooring C predicts an amplitude of about 0.6 m s^{-1} (Fig. 5), comparable to the 0.50–0.58 observed in the CL cluster (Fig. 10). If we model the wind as due to a storm of fixed shape which translates over the ocean with a velocity **G**, then (1) implies that the resulting mixed layer inertial currents will have a phase speed $c = f/\alpha$ equal to $|\mathbf{G}|$ and a horizontal wavenumber with the same direction as **G**. Extrapolating the wavenumbers in Fig. 7 to the time of the storm, day 277.5, we estimate $c = 29 \pm 5$ m s^{-1} on a heading of $73 \pm 10°$T. This is about 50% faster than the meteorological estimate of the storm advection speed, 18.5 m s^{-1}, but in approximately the same direction. We conclude that the assumption of a fixed shape, translating storm is not very accurate here, unlike in D'Asaro (1994b) or Kundu and Thomson (1985). The winds of this storm rotate at almost exactly the inertial frequency and are therefore very efficient generators of mixed layer inertial currents (Crawford and Large 1994b). The amplitude and phase of these currents may therefore be quite sensitive to the details of the wind field, perhaps explaining the observed difference between c and $|\mathbf{G}|$.

b. The β effect

The spatial scale of the mixed layer inertial currents decreases by an order of magnitude in the 20 days following the storm. Figure 7 shows that this is almost entirely due to a decrease in the north-south wavenumber l at a rate $-\beta t$. This is in excellent agreement with (18).

c. Does $f = f_{eff}$*?*

Formulation. During the storm and for about 10 days thereafter, the mixed layer inertial currents have a horizontal scale much larger than the Rossby radius, so equation (13) is valid. Furthermore, the rate of linear wave propagation is small (see below). Under these conditions, the $\hat{P}$ term can be ignored in (13) and it reduces to

$$\tilde{U}_I(t) = \tilde{U}_I(t_0) + \int_{t_0}^{t} if_{\text{eff}}\tilde{U}_I dt + \int_{t_0}^{t} e^{\text{if}_{\text{eff}}t} T dt \,, \tag{20}$$

where the integration is along a Lagrangian trajectory of the mixed layer. Equation (20) differs from (1) in that the mesoscale vorticity changes the effective inertial frequency to f_{eff}. We now test whether we can see this effect in the data.

Generation of inertial currents and f_{eff}. We first examine the generation of mixed layer inertial currents by the storm. The dependence of $\tilde{U}_I$ on f_{eff} was quantified by evaluating (20) for different values of f_{eff} using the same wind stress from Fig. 4. We assume $U = 0$ at day 275. We find that a vorticity of $-0.08f$ increases $|\tilde{U}_I|$ on day 280 by 0.1 m s^{-1} and rotates its direction 15° clockwise. The same calculation using winds measured at other sites within the array gives similar results.

Figure 12a overlays contours of the measured $|\tilde{U}_I|$ averaged over days 280–284, as in Fig. 6, and relative vorticity ζ (shaded) from Fig. 2. There is a general increase in $|\tilde{U}_I|$ to the northwest, with smaller scale fluctuations. The fluctuations seem to be correlated with the vorticity. Figure 12b isolates the fluctuations by removing the larger scale

trend with a quadratic smoothing spline (Wahba 1975); the smoothing parameter is 44 km. The main feature is a central minimum in ζ of magnitude $-0.02f$ corresponding to a 0.13 m s^{-1} increase in $|\tilde{U}_I|$ and an 11° counterclockwise rotation of its direction. These changes are 3 to 4 times larger than predicted by (20), and the rotation is in the wrong sense. They cannot be caused by the direct effect of f_{eff}.

The wind stress and mixed layer depth, or some integrated equivalent, are the most obvious factors influencing the inertial currents generated by the storm. The data indicate that the combination of these can easily produce the variations in $\tilde{U}_I$ seen in Fig. 12 and that any correlation of these with vorticity is indirect. Crawford and Large (1994a,b) show that the difference in measured wind at two drifting buoys 50 km apart near 48.5°N, 139°W produces a difference of about 0.2 m s^{-1} in $\tilde{U}_I$, in agreement with the observations. Similarly, mixed layer depths measured after the storm at the nine thermistor chains deployed in this region vary from 29 m to 41 m, a variation capable of producing about 0.2 m s^{-1} change in $\tilde{U}_I$. These data are limited, but suggest a correlation between mixed layer depth and ζ in the right sense to produce the observed correlation between $\tilde{U}$ and ζ.

Evolution of inertial currents and f_{eff}. The variations in f_{eff} should modulate the phase of the mixed layer inertial currents. We test for this by integrating (20) along each drifter trajectory with $\tilde{U}_I(t_0)$ set from the parameters of the fit of (19) at day 280. These simulated data are then fit with (19) and the fit parameters shown in Fig. 13, along with

the fit parameters for the data. Three variants on (20) were used: (i) assuming $\zeta = 0$; (ii) using the ζ from Fig. 2c; and (iii) averaging ζ_A along each trajectory to form ζ_A and using $\zeta = <\zeta_A> - f$. Note that E_{tot} is constant by construction since (20) only changes the direction of $\tilde{U}_I$. In all simulations, we assume $T = 0$ since the winds are light during this interval.

The best agreement between the data and (20) is found by assuming $\zeta = 0$. Including ζ in (20) produces small-scale structure in $\tilde{U}_I$, destroying the large-scale coherence and resulting in a rapid decrease in E_{fit}. This is illustrated in Fig. 14. On day 280 (Fig. 14a), the $\tilde{U}_I$ are initialized to a constant amplitude and a linearly varying direction. With $\zeta = 0$, the vectors on day 288 (Fig. 14b) are very similar to those observed (Fig. 6c), with perhaps somewhat more small-scale structure. Including ζ, however, either directly (Fig. 14c) or via $<\zeta_A>$ (Fig. 14d), produces much more small-scale structure than is observed. Either the ζ does not affect f_{eff}, or some other force acts to eliminate the small-scale structure produced by it.

We cannot dynamically justify setting $\zeta = 0$ in (20). Doing this, however, leads to a remarkably good prediction of the fit wavenumbers, both using all the drifters [Figs. 7 (heavy dashed line) and 13] and in each of the subgroups (heavy dashed lines in Figs. 8–11). In particular, it predicts both the average deviation of l from the $-\beta t$ line (Figs. 7 and 13) and its variation between subregions. This indicates that horizontal advection, and the resultant straining of the mixed layer inertial currents, plays a measur-

able, if small, role in determining their structure.

d. Linear wave theory

Gill (1984) predicts the approximate residence time of mixed layer inertial currents based on their horizontal scale, i.e., (9). In our data, the horizontal scale of the inertial currents varies rapidly in time. Following D'Asaro (1989) we modify (8) so that the phase of the n^{th} mode at time t is

$$\Theta_n(t) = \int_0^t \frac{c_n^2}{2f} \alpha(t)^2 dt \, . \tag{21}$$

Gill (1984) then predicts that the amplitude of the mixed layer inertial currents will be reduced by a factor σ_n at time t_n such that $\Theta_n(t_n) = \frac{1}{2}\pi$. Table 1 lists c_n and the cumulative σ_n computed from a representative CTD profile and a $Z(z)$ taken from moored velocity observations (see Parts II and III). The values of c_1 and c_2 are quite stable; using different CTD profiles results in changes of less than 10%. The σ_n vary due to both stratification and $Z(z)$; reasonable bounds on σ_1 are 0.12–0.15.

Figure 15 compares the observations and linear predictions of the quantity $\tau_{1/2}$, defined as the time for E_{fit} to fall to half its value on day 280 (day 282 for subgroup CL). Theoretically, Table 1 shows that $(1-\sigma_1-\frac{1}{2}\sigma_2)^2$ is close to 0.5, so the predicted $\tau_{1/2}$ corresponds to the time when mode 1 has separated and mode 2 is about half way separated. We expect this to occur at approximately $\frac{1}{2}(t_1 + t_2)$, so we use $c_{1/2}^2 = \frac{1}{2}(c_1^2 + c_2^2) = (1.78 \text{ m s}^{-1})^2$ in (21). Observationally, we extract $\tau_{1/2}$ from Figs. 7–11.

We now compare the observed and predicted values of $\tau_{½}$ in Fig. 15 The 95% confidence limits are from the Monte Carlo simulated data. The observed and predicted $\tau_{½}$ are correlated, but the predicted values are about 2 days larger than the observed values; linear theory underpredicts the decay rate. Using $c_{½} = 2.5$ m s^{-1} gives a better fit (circles); this value is high, but perhaps plausible.

Linear wave theory clearly fails at longer times. E_{tot} decays to 2.5% of its initial value by day 300, 23 days after the storm; E_{fit} decays to about 0.7% of its initial value. Using (21), we find that only modes 1–3 should have separated by this time. Linear theory therefore predicts a reduction of E_{fit} to $(1-\sigma_1-\sigma_2-\sigma_3-½\sigma_4)$ = 10% of its initial value. This estimate is confirmed in a full simulation of the data in Part III. It is a large underestimate of the actual decay. In linear theory, the high modes propagate very much slower than the low modes, since c_n^2 is roughly proportional to n^{-2}. The observations show the high mode energy disappearing at approximately the same rate as the lower mode energy. Linear internal wave theory alone cannot explain this.

8. Summary

The near-surface velocity field in a 300 km × 300 km region of the northeast Pacific was measured using an array of 36 nearly Lagrangian drifters drogued at 15 m, CTD profiles, and 3 ADCP moorings. We describe these measurements for a 23 day period following a strong storm. The storm generates near-inertial frequency currents of small horizontal wavenumber in the mixed layer. The variation of f with latitude increases the

north-south wavenumber at a rate $-\beta t$ as predicted for inertial motions on a β-plane. Linear internal wave theory predicts that near-inertial motions with the initial horizontal wavenumber will propagate very slowly. Their propagation rate is predicted to increase along with the wavenumber magnitude, eventually spreading the mixed layer inertial energy horizontally and vertically over a wide region. Qualitatively, the observations match these predictions. Quantitatively, however, the mixed layer inertial currents decay more rapidly than predicted by linear theory, particularly after most of the initial energy has decayed.

a. Subinertial currents

The array was intentionally located in a region of weak flow, so that wind forced effects would be easy to measure.

- The subinertial flow was dominated by low-mode, nondivergent geostrophic motions with a level of no motion near 800 m.

- The spatial mean currents were northeastward at 0.025 m s^{-1}. The eddy currents were 0.05 m s^{-1} rms, of dominantly anticyclonic vorticity (0.023 f rms) magnitude, and a wavelength of roughly 100 km.

- Water parcels move through the nearly stationary eddy field much faster than it evolves, so absolute vorticity is conserved along streamlines to the measurement accuracy.

b. Inertial frequency currents

• The storm produced energetic (0.35–0.7 m s^{-1}) inertial motions in the mixed layer. Their magnitude can be predicted from the measured winds as interpreted by Large et al. (1994).

• The horizontal structure of the mixed layer inertial currents can be accurately described by a single, time dependent horizontal wavenumber.

• The initial horizontal wavelength of the mixed layer inertial motions was large, about 1700 km. This is about 50% larger than would be predicted by assuming that a storm of fixed shape advected over the region at the observed rate.

• Smaller-scale variations in the amplitude and phase of the mixed layer inertial motions are correlated with the measured subinertial vorticity. These variations are too large, however, to be directly explained by the variation in the effective Coriolis frequency induced by subinertial vorticity. Variability in the atmospheric forcing and in the mixed layer depth probably account for these variations in inertial currents and probably lead, indirectly, to a correlation with vorticity.

• The east-west wavenumber of the mixed layer inertial currents remains constant after the storm, while the north-south wavenumber decreases at about $-\beta t$ as expected for inertial currents on a β-plane.

• The theoretically expected variation in the frequency of the mixed layer inertial currents with subinertial vorticity was not observed. The best prediction of their

horizontal structure is made using a model which includes only advection of the inertial currents by the subinertial currents.

• The mixed layer inertial energy decayed to half its initial value in 8–14 days, depending on location within the array. Regions with a larger horizontal wavenumber decay more rapidly as predicted by linear internal wave theory. On average, however, linear theory underpredicts this decay time by about 2 days.

• The mixed layer inertial energy decays to background levels in 20–25 days depending on location. This is much faster than predicted by linear internal wave theory.

9. Discussion

D'Asaro (1989) describes a scenario in which large-scale storms generate large-scale inertial motions in the mixed layer. The combined action of β and mesoscale eddies then decreases the scale of these motions until the rate of linear internal wave propagation is large enough to remove them from the mixed layer. Although this appears to be correct in broad outline, particularly, in the strong effect of β, it cannot completely explain our observations. This theme is repeated in Parts II and III, where other important differences between the observations and theoretical expectations based on linear theory are described. It appears that D'Asaro (1989) omits at least one important mechanism affecting the behavior of mixed layer inertial currents.

Practically, this analysis, combined with D'Asaro (1994b), demonstrates the important role of horizontal scale in controlling the residence time of mixed layer near-inertial motions. Gill (1984) suggests replacing $-rU$ in (1) by $-c_1^2/(2f)\nabla^2 U$ as a way of including this physics in simple models of the mixed layer. Our results indicate that this parameterization would result in improved predictions of mixed layer inertial currents, particularly since it would properly predict the rapid decay of the last 10% of the inertial energy. However, since we do not know why this final decay occurs, it is not clear when such a parameterization would fail.

Acknowledgments. EAD thanks Brad Bell for help with programming. Eric Kunze made many helpful comments on an early draft of this article. This work was supported by the Office of Naval Research, contracts N00014-84-C-0111 and N00014-87-K-0004 and grant N00014-90-J-1104.

APPENDIX

a. Drifter interpolation by objective analysis

We interpolate the irregularly spaced time series of drifter position assuming that these positions are realizations of an isotropic, stationary random process with known statistics using the objective analysis techniques outlined by McIntosh (1990) and Davis et al. (1992). The assumption of a stationary signal will later be relaxed to allow for slowly changing statistics to accommodate nonstationarity of the variance of the low-frequency and higher-frequency components of the data set.

The positions of the drifters at time i are estimated using N observations at times t_n according to

$$\bar{\mathbf{x}}(t) = \sum_{n=1}^{N} \left[\alpha_n(t)\mathbf{r}_n + \beta_n(t)\hat{z}\times r_n \right] , \qquad \text{(A1)}$$

where $\bar{\mathbf{x}}(t)$ is the estimate of the float position at time t, $\mathbf{r}_n$ is the observed position at time t_n, and $\hat{z}$ is the vertical unit vector. In this formula α takes into account how longitude observations are used in estimating the longitude component of the position and how latitude observations are used in estimating the latitude component. Similarly, β takes into account how the latitude observations influence the estimated longitude estimate and how the longitude observations influence the latitude estimate. This means that rotary tendencies like inertial or tidal motions can be modeled accurately. These weights are calculated by minimizing the mean square position error, $\varepsilon = <|\bar{\mathbf{x}}(t) - \mathbf{x}(t)|^2>$, subject to

$$\sum_{n=1}^{N} \alpha_n = 1 \tag{A2}$$

$$\sum_{n=1}^{N} \beta_n = 0 . \tag{A3}$$

These constraints are necessary to assure that the observed mean and estimated mean are similar. The positions could be referenced to the sample mean, but this would make the time series nonstationary.

The analysis also requires knowledge about the covariance function and the distribution function of the error. The error will be modeled as Gaussian, uncorrelated with the data, with zero mean and a position variance of 500 m^2. Since the observed spectra of position have a large inertial peak and a red low-frequency spectrum, we use correlation functions that mimic these features. The correlation function that generates α is

$$\langle x(t_1)x(t_2)\rangle = \hat{U}^2 \tau_L^2 \, e^{\frac{-(t_1-t_2)^2}{2\tau_L^2}} + \hat{u}^2 \frac{\tau_I^2}{f_0^2 \tau_I^2 + 1} \cos(f_0(t_2-t_1)) \, e^{-\frac{(t_1-t_2)^2}{2\tau_I^2}} , \tag{A4}$$

and the one that generates β is

$$\langle x(t_1)y(t_2)\rangle = \hat{u}^2 \frac{\tau_I^2}{f_0^2 \tau_I^2 + 1} \sin(-f_0(t_2 - t_1)) \, e^{-\frac{(t_1-t_2)^2}{2\tau_I^2}} . \tag{A5}$$

$\hat{U}^2$ is the variance of the low-frequency component of the velocity; $\hat{u}^2$ is the variance of the inertial component of the velocity. These variances are computed using a moving average of 40 points for the inertial component and 80 points for the low-frequency component. We use τ_L = 3 days and $\tau_I = 4/f_0$. As described in the text, these values give inertial and subinertial currents very close to those estimated by D'Asaro (1992) for this

same data set.

b. Mapping the subinertial velocity

We map the subinertial velocity field as described by Bretherton et al. (1976) using the analytical correlation function from McWilliams (1976a,b). Figure A1 shows estimates of the longitudinal (Fig. A1a) and transverse (Fig. A1b) correlation functions for the subinertial drifter velocities in Fig. 2. Using all possible buoy pairs produces a longitudinal correlation function (small dots) with a minimum in coherence at 5 km. This seems anomalous. Many of the data pairs with short spatial lags are really autocorrelation pairs for buoys with small speed; these are the data most likely to be decorrelated by wind-forced currents. Removing buoys with speeds less than 0.04 m s^{-1} reduces the anomalously low correlations at 5 km (pluses) but has little effect at larger lags. A purely spatial correlation function was constructed by computing the lagged covariances for each day and averaging the 21 covariances at each lag to form a correlation function (large dots in Fig. A1). Far fewer pairs are used, so the correlation function is much noiser and 20 km bins are required. The two data sampling schemes produce significantly different transverse correlation functions. A fit of the McWilliams (1976a,b) analytical correlation functions (solid lines in figure) with a longitudinal correlation scale of 150 km and a transverse scale of 40 km yields a good fit to the longitudinal data, but it overestimates the negative lobe of the transverse correlation function. This discrepancy cannot be corrected by varying the coefficients; it indicates that the objectively analyzed

fields may have some systematic errors. Objective analysis also requires an estimate of the small-scale "noise" in the field due to instrumental error and small-scale oceanographic motions. Instrumental, windage, and demodulation errors for the drifters are estimated at 0.01 m s^{-1} in each component, or about 5% of the variance. The fields produced using these parameters differ from those produced using two-dimensional quadratic smoothing splines (Wahba, 1975) by less than the estimated error.

Objective analysis of the dynamic height data (Fig. 3) used a correlation function of form $e^{-(r/\Delta)^2}$ for separation r. Using Δ = 100 km gives a rough fit to the correlation function estimated from the data. Again, smoothing splines produce a very similar field.

c. Fitting (19)

For each value of the parameters k and l, U_{fit} is determined by linear least squares. A dense search in k,l space is used to find a starting point for a nonlinear, least squares minimization using an algorithm similar to that of Marquardt (1963).

d. Monte Carlo simulation

We model the field of inertial currents by (19) using the fit values of U_{fit}, k, and l and consider U_R to be a continuous random function characterized by its correlation function. Figure A2 shows the covariance function of the measured U_R (dashed) computed for all fits between days 276 and 300. Realizations of U_R were generated by smoothing an array of random Gaussian vectors with a two-dimensional quadratic

smoothing spline (Craven and Wahba, 1979), fitting this field with (19), and computing the residual from this fit. The variance and amount of smoothing were chosen so that the correlation function of the data is the same as that of these realizations within their confidence limits (solid line, Fig. A2). Note that U_R is spatially inhomogeneous since (19) fits data better near the center of the array than near its edge. The simulated U_R simulate this inhomogeneity well except for the northwest corner of the domain where the simulated variance is less than that of the data. Adjusting the simulated fields to improve this does not make a significant difference in the confidence limits computed from the simulations, and we did not include such an adjustment.

REFERENCES

Bell, T.H., 1978: Radiation damping of inertial oscillations in the upper ocean. *J. Fluid Mech.*, **88**, 289–308.

Bretherton, F.P., R.E. Davis, and C.B. Fandry, 1976: A technique for objective analysis and design of oceanographic experiments applied to MODE-73. *Deep-Sea Res.*, **23**, 559–582.

Craven, P., and G. Wahba, 1979: Smoothing noisy data with spline functions: Estimating the correct degree of smoothing by the method of generalized cross validation. *Numer. Math.*, **3**, 377–403.

Crawford, G.B., and W.G. Large, 1994a: Observations and simulations of upper ocean response to wind events during the OCEAN STORMS experiment. (this volume)

———, and ———, 1994b: A numerical investigation of resonant inertial response of the ocean to wind forcing. (this volume)

D'Asaro, E.A., 1985: The energy flux from the wind to near-inertial motions in the surface mixed layer. *J. Phys. Oceanogr.*, **15**, 1043–1059.

———, 1989: The decay of wind-forced mixed layer inertial oscillations due to the β effect. *J. Geophys. Res.*, **94**, 2045–2056.

———, 1992: Estimation of velocity from Argos-tracked surface drifters during OCEAN STORMS. *J. Atmos. Oceanic Technol.*, **9**, 680–686.

———, 1994a: Upper ocean inertial currents forced by a strong storm: Part III.

Modeling. (this volume)

———, 1994b: Observations and dynamics of small-scale, storm-forced inertial frequency currents. (this volume)

———, and H. T. Perkins, 1984: A near-inertial internal wave spectrum for the Sargasso Sea in late summer. *J. Phys. Oceanogr.*, **14**, 489–505.

———, R. E. Davis, C. C. Eriksen, and M. D. Levine, 1994: Upper ocean inertial currents forced by a strong storm: Part II. Propagation into the thermocline. (this volume)

Davis, R. E., R. A. de Szoeke, and P. P. Niiler, 1981: Variability in the upper ocean during MILE. Part II: Modeling the mixed layer response. *Deep-Sea Res.*, **28**, 1453–1475.

———, D. C. Webb, L. A. Regier, and J. Dufour, 1992: The autonomous Lagrangian circulation explorer (ALACE). *J. Atmos. Oceanic Technol.*, **9**, 264–285.

———, C. C. Eriksen, M. D. Levine, W. G. Large, and E. A D'Asaro, 1994: (this volume)

Ekman, V. W., 1905: On the influence of the earth's rotation on ocean currents. *Ark. Mat. Astron. Fys.*, **2**(11), 1–53.

Eriksen, C. C., 1988: On wind forcing and observed oceanic wave number spectra. *J. Geophys. Res.*, **93**, 4985–4992.

Gill, A. E., 1984: On the behavior of internal waves in the wakes of storms. *J. Phys.*

Oceanogr., **14**, 1129–1151.

Käse, R. H., 1979: Calculations of the energy transfer by the wind to near-inertial internal waves. *Deep-Sea Res.*, **26**, 227–232.

Kroll, J., 1982: An unstable uniform slab model of the mixed layer as a source of downward propagating near-inertial motion. Part I: Steady mean flow. *J. Mar. Res.*, **40**, 1013-1033.

Kundu, P. K, and R. E. Thomson, 1985: Inertial oscillations due to a moving front. *J. Phys. Oceanogr.*, **15**, 1076–1084.

Kunze, E., 1985: Near-inertial wave propagation in geostrophic shear. *J. Phys. Oceanogr.*, **15**, 544–565.

Large, W. G., and S. Pond, 1981: Open ocean momentum flux measurements in moderate to strong winds. *J. Phys. Oceanogr.*, **11**, 324–336.

———, J. Morzel, and G. B. Crawford, 1994: A note on possible errors in inferring 10 m wind speed from low-level anemometer measurements. (this volume)

Leaman, K. D., 1976: Observations on the vertical polarization and energy flux of near-inertial waves. *J. Phys. Oceanogr.*, **6**, 894–908.

Marquardt, D. W., 1963: An algorithm for least-squares estimation of nonlinear parameters. *J. Soc. Indus. Appl. Math.*, **11**, 431–440.

Matear, R. J., 1993: Circulation within the Ocean Storms area located in the northeast Pacific Ocean determined by inverse methods. *J. Phys. Oceanogr.*, **23**, 648–658.

McIntosh, P. C., 1990: Oceanographic data interpolation: Objective analysis and splines. *J. Geophys. Res.*, **95**, 13,529–13,541.

McWilliams, J. C., 1976a: Maps from the Mid-Ocean Dynamics Experiment: Part I. Geostrophic streamfunction. *J. Phys. Oceanogr.*, **6**, 810–827.

———, 1976b: Maps from the Mid-Ocean Dynamics Experiment: Part II. Potential vorticity and its conservation. *J. Phys. Oceanogr.*, **6**, 828–846.

Müller, P., D. J. Olbers, and J. Willebrand, 1983: The IWEX spectrum. *J. Geophys. Res.*, **83**, 479–500.

Niiler, and J. D. Paduan, 1994: Wind driven motions in the northeast Pacific as measured by Lagrangian drifters. (this volume)

———, R. E. Davis, and H. J. White, 1987: Water-following characteristics of a mixed layer drifter. *Deep-Sea Res.*, **34**, 1867–1881.

Paduan, J. D., and P. P. Niiler, 1993: Structure of velocity and temperature in the northeast Pacific as measured with Lagrangian drifters in fall 1987. *J. Phys. Oceanogr.*, **23**, 585–600.

———, R. A. de Szoeke, and R. A. Weller, 1989: Inertial oscillations in the upper ocean during the Mixed Layer Dynamics Experiment (MILDEX). *J. Geophys. Res.*, **94**, 4835–4842.

Pollard, R. T., 1970: On the generation by winds of inertial waves in the ocean. *Deep-Sea Res.*, **17**, 795–812.

———, 1980: Properties of near-surface inertial oscillations. *J. Phys. Oceanogr.*, **10**, 385–398.

———, and R.C. Millard, Jr., 1970: Comparison between observed and simulated wind-generated inertial oscillations. *Deep-Sea Res.*, **17**, 813–821.

Price, J.F., 1981: Upper ocean response to a hurricane. *J. Phys. Oceanogr.*, **11**, 153–175.

———, 1983: Internal wave wake of a moving storm, I, Scales, energy budget and observations. *J. Phys. Oceanogr*, **13**, 949–965.

———, R.A. Weller, and R. Pinkel, 1986: Diurnal cycling: Observations and models of the upper ocean response to diurnal heating, cooling and wind mixing. *J. Geophys. Res.*, **91**, 8411–8427.

———, ———, and R.R. Schudlich, 1989: Wind driven ocean currents and Ekman transport. *Science*, **238**, 1534–1538.

Qui, H., R.A. de Szoeke, C.A. Paulson, and C.C. Eriksen, 1994: The structure of near-inertial waves during OCEAN STORMS. (this volume)

Sanford, T.B., P.G. Black, J.R. Haustein, J.W. Feeney, G.Z. Forristall, and J.F. Price, 1987: Ocean response to a hurricane: Part I. Observations. *J. Phys. Oceanogr.*, **17**, 2065–2083.

Shen, C., and J. McWilliams, 1978: Optimal arrays for estimating potential derivatives and non-linear terms in a potential vorticity budget. *Special Report #85*, Depart-

ment of Oceanography, University of Washington, Seattle, WA 98105.

Smith, R., 1973: Evolution of inertial frequency oscillations. *J. Fluid Mech.*, **60**, 383–389.

Tabata, S., L. A. F. Spearing, R. H. Bigham, B. G. Minkley, J. Love, D. Yelland, J. Linguanti, and P. M. Kimber, 1988: STP/hydrographic observations along line P, Station P, Line R and associated lines, and in the "OCEAN STORMS" area. Canadian Data Report of Hydrography and Ocean Sciences, No. 70, 132 pp. [Available from Institute of Ocean Sciences and Department of Fisheries and Oceans, Sidney, B.C.]

Thomson, R. E., and W. S. Huggett, 1981: Wind-driven inertial oscillations of large spatial coherence. *Atmos.–Oceans*, **19**, 281–306.

Wahba, G., 1975: Smoothing noisy data with spline functions. *Num. Mathematik*, **24**, 383–393.

Webster, F., 1968: Observation of inertial-period motions in the deep sea. *Rev. Geophys.*, **6**, 473–490.

Zervakis, V., and M. D. Levine, 1994a: (this volume)

———, and ———, 1994b: (this volume)

FIGURE CAPTIONS

FIG. 1. Mixed-layer drifter trajectories for days 275–300 of 1987 interpolated and filtered as described in the text. Many drifters were not deployed until day 280. Moorings are indicated by the three large dots. Light lines define the geographic subregions used in the analysis.

FIG. 2. Analysis of subinertial velocities from mixed layer drifters for days 280–300. (a) Subinertial velocity smoothed and sampled every 4 days (heavy arrows). An objectively analyzed field of vectors (light arrows) is computed from these. Only data with less than 60% error are shown. Contours of 80%, 60%, and 40% error are plotted. (b) Surface dynamic height contours; contour interval is 1 dynamic centimeter, and mapped velocity arrows from (a). (c) Relative vorticity; contour interval is 1% of f, and mapped velocity arrows from (a). (d) Absolute vorticity; contour interval is 2% of f, and mapped velocity arrows from (a).

FIG. 3. Dynamic height relative to 800 dbars from CTD data. Station positions are indicated by the circles. Contour interval is 1 dynamic centimeter.

FIG. 4. Wind stress and inertial current generation. (a) Wind stress (Crawford and Large 1994a) at mooring C. (b) East and north velocity components predicted from (1) with $H = 55$ m. (c) Corresponding speed and direction.

FIG. 5. Surface chart for 12Z, day 277. All wind and pressure observations from 10Z to 14Z are used. Observations are advected by the mean speed of the storm to their

estimated position at 12Z. Heavy lines give frontal positions; dashed lines give wind speed contours; arrows are wind speed measurements.

FIG. 6. Evolution of mixed layer inertial currents. Each panel shows mixed layer inertial current from drifters and moorings (arrows) and speed and direction contours from an objective mapping of these data. Only regions with an error less than 80% are shown. Speed contour interval is 0.02 m s^{-1}. Direction contour interval is 22.5°. Speed contours are shaded starting at 20 m s^{-1} and darkening at 40 m s^{-1}.

FIG. 7. Parameters of plane-wave fit to mixed layer inertial currents for all data. (a) Fit energy E_{fit} (shaded), total energy E_{tot} (line), and phase of U_{fit} (heavy line). (b) Wavenumbers k (light solid line); l (heavy solid line). (c) Number of data points in fit. Diagonal dashed line has a slope of $-\beta$. Other dashed lines show results of evaluating the model (20) with $\zeta = 0$ for each parameter. Symbols show parameters for 20 Monte Carlo simulations of the fit residuals and serve as confidence limits.

FIG. 8. Parameters of plane-wave fit to mixed layer inertial currents for subgroup NW.

FIG. 9. Parameters of plane-wave fit to mixed layer inertial currents for subgroup NE.

FIG. 10. Parameters of plane-wave fit to mixed layer inertial currents for subgroup CL.

FIG. 11. Parameters of plane-wave fit to mixed layer inertial currents for subgroup STH.

FIG. 12. (a) Contours of relative vorticity as in Fig. 2c (shaded; contour interval = 2% of f) and of average inertial speed $|\tilde{U}_I|$ for days 280–284 (interval = 0.02 m s^{-1}). Only data with less than 40% error are shown. Heavy contour is 30% error line for inertial velocity. (b) Relative vorticity as in (a), with vectors of spatially high-passed $|\tilde{U}_I|$.

FIG. 13. Parameters of plane-wave fit to data (heavy line) and to the Lagrangian model (20). Cases are advection only ($\zeta = 0$), measured ζ, and $\zeta = <\zeta_A> - f$. Display is as in Figs. 7–11.

FIG. 14. Mixed layer inertial currents produced by the model (20). Field (a) is initialization on day 280.5. (b)–(d) are field on day 288.5: (b) Advection only, $\zeta = 0$, in Fig. 13; (c) Advection and measured ζ, case ζ in Fig. 13; (d) Advection and ζ from $<\zeta_A>$, case $<\zeta_A>$ in Fig. 13.

FIG. 15. Comparison of observed and predicted values of $\tau_{1/2}$ the time for the mixed layer inertial currents to decay to half their initial value. Confidence limits are approximately 95% from 20 Monte Carlo simulations. Circles are prediction with unrealistically high value of $c_{1/2} \approx 2.5$ m s^{-1}.

FIG. A1. Estimated correlation functions for subinertial velocity data in Fig. 2. (a) longitudinal, (b) transverse. Symbols indicate type of averaging: small dots = all data grouped in 5 km bins; plus = data with speed greater than 0.04 m s^{-1} in 5 km bins; large

dots = data from each day averaged in 20 km bins and these covariances averaged to form correlations; lines = correlation functions used in analysis.

FIG. A2. Estimated covariance functions for U_R in (19) from data (dashed line) and from average of 20 Monte Carlo simulations of data (solid line). Error bars are approximate 95% confidence limits from these simulations.

TABLE 1. Modal properties.

n	$\sum_{k=1}^{n} \sigma_k$	c_n m s^{-1}
1	0.14	2.18
2	0.44	1.27
3	0.64	0.92
4	0.71	0.66
5	0.78	0.52
6	0.89	0.44
7	0.96	0.39
8	0.97	0.34
9	0.98	0.29
10	0.98	0.26
20	0.98	0.13
30	0.98	0.09
40	0.98	0.06
50	0.98	0.05

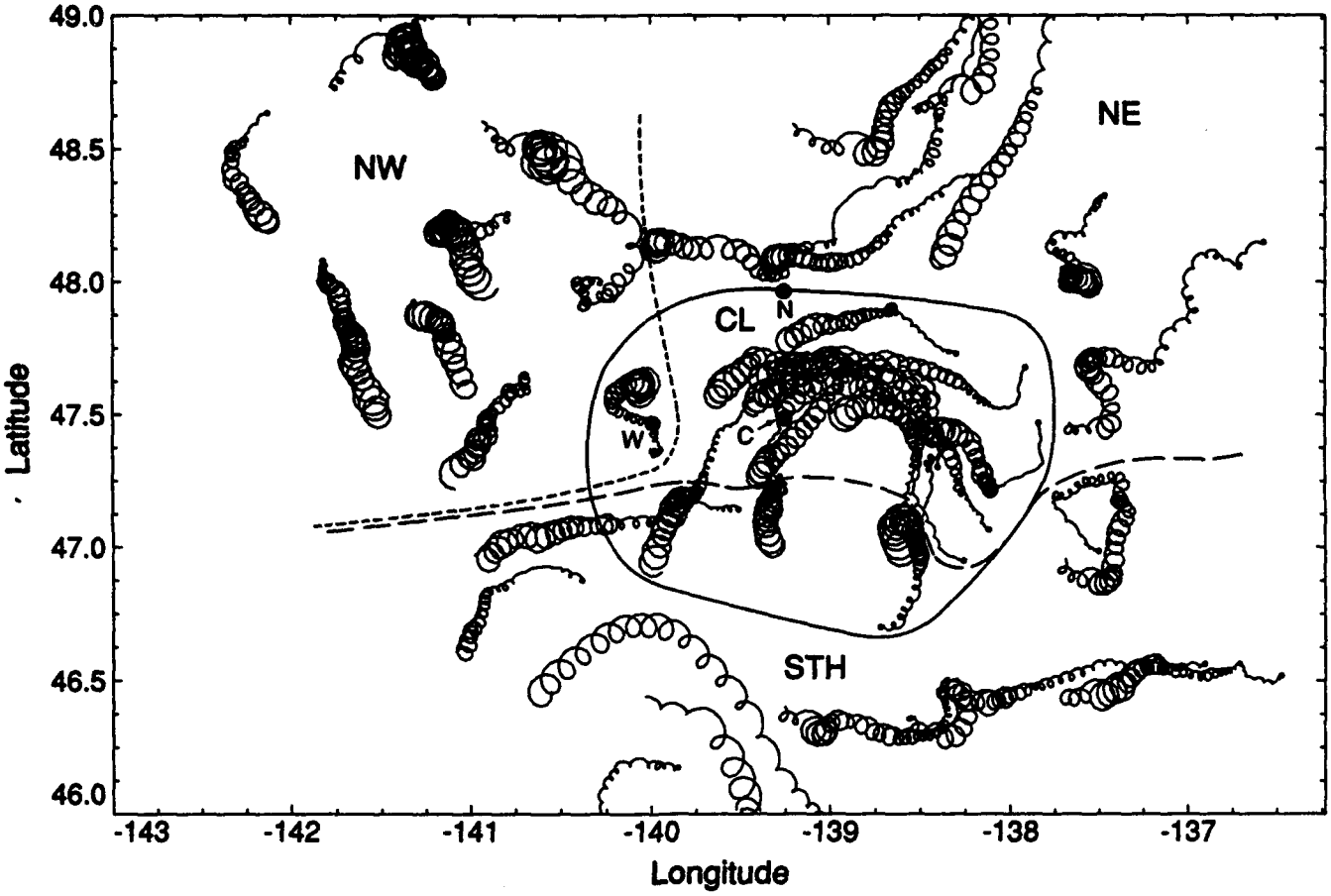

D'Asaro et al., Part I, Fig. 1

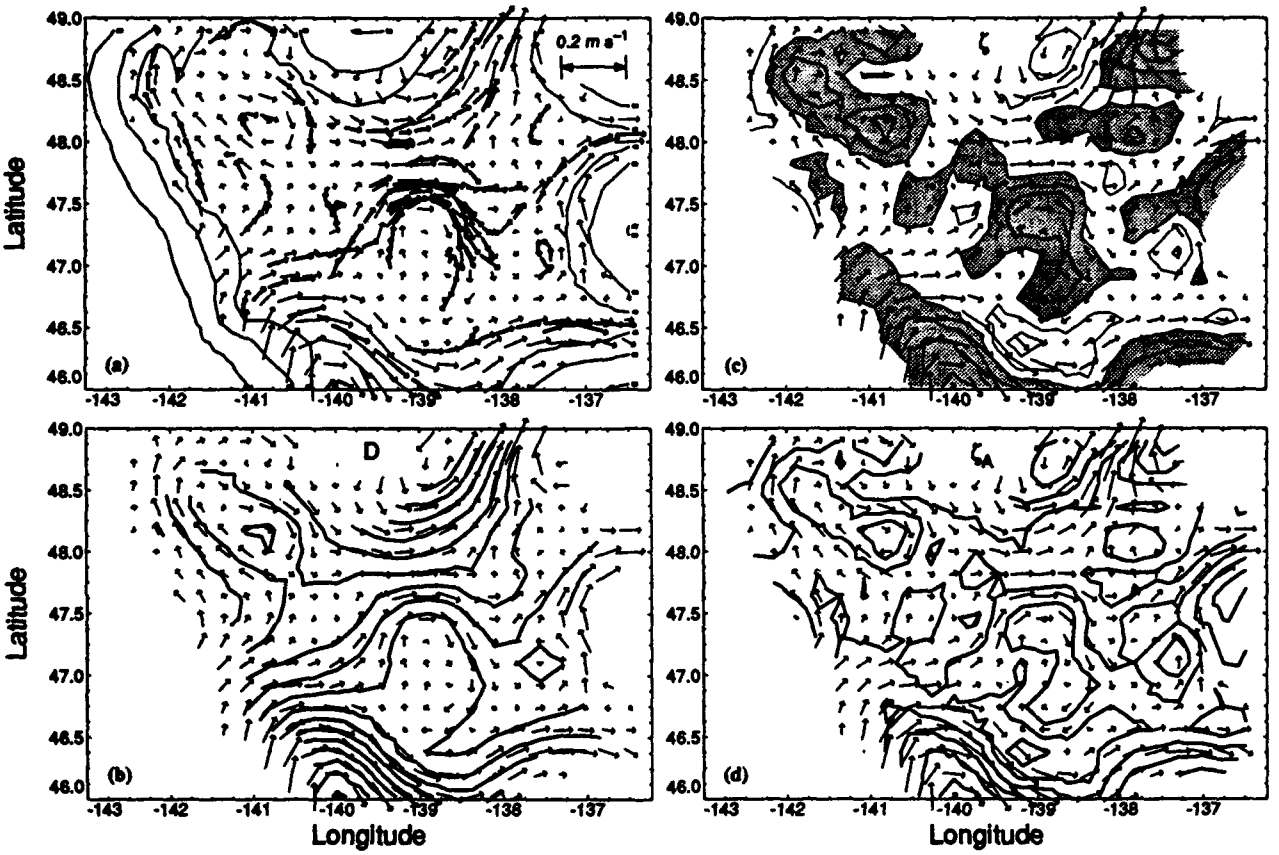

D'Asaro et al., Part I, Fig. 2

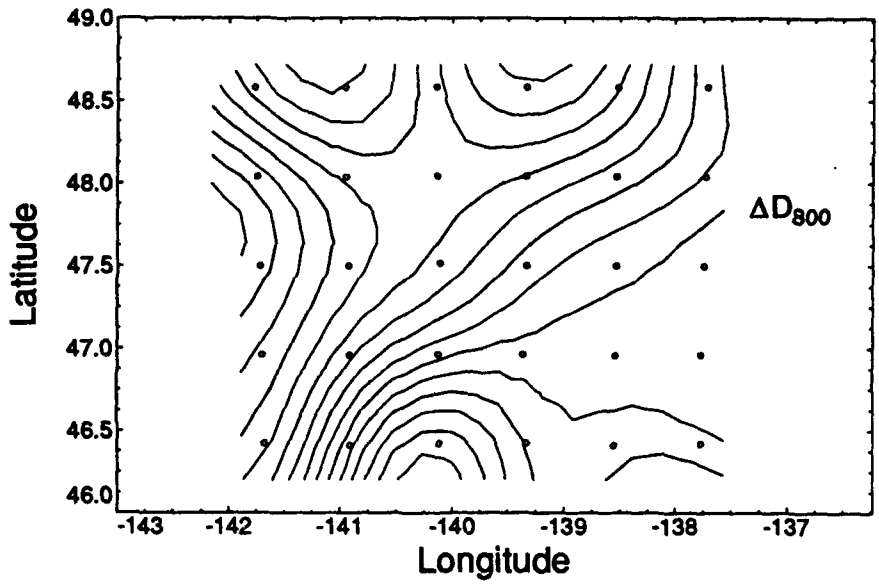

D'Asaro et al., Part I, Fig. 3

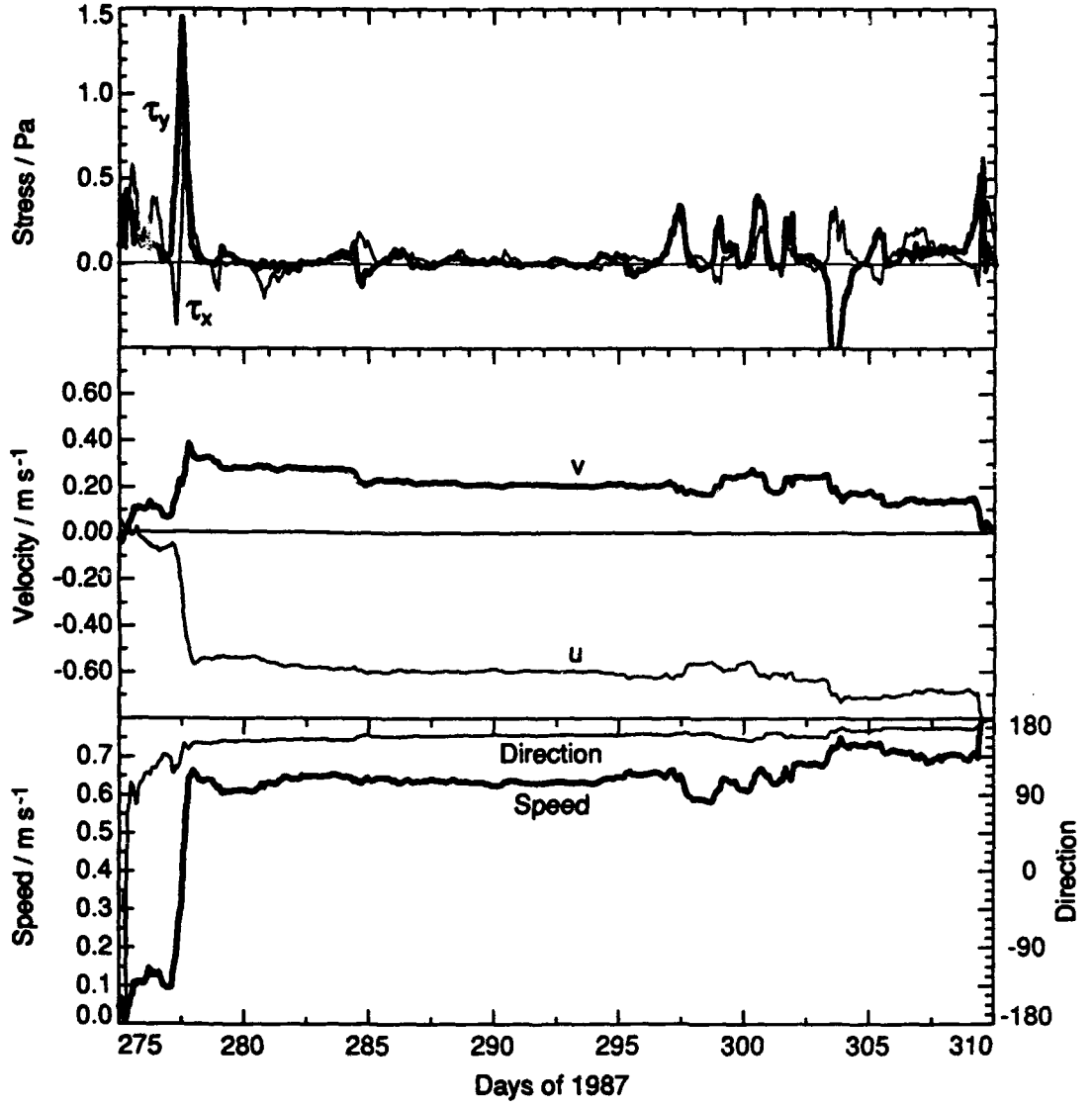

D'Asaro et al., Part I, Fig. 4

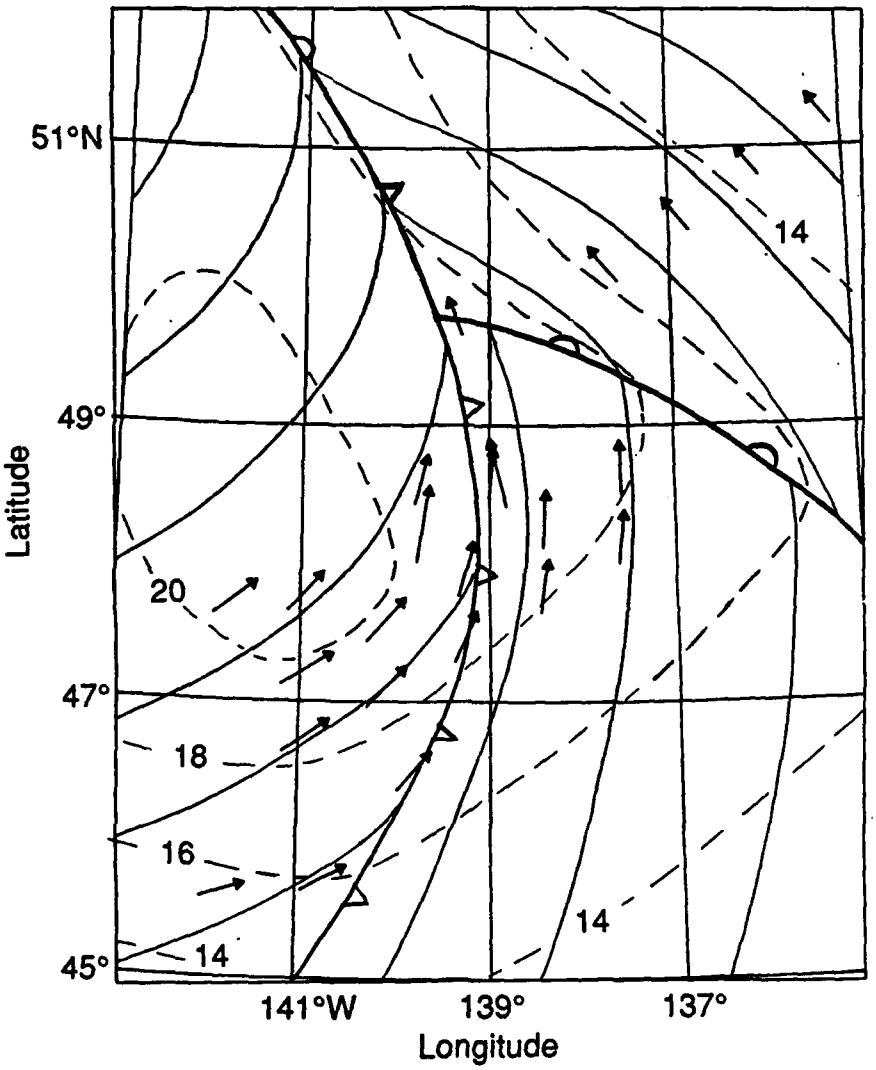

D'Asaro et al., Part I, Fig. 5

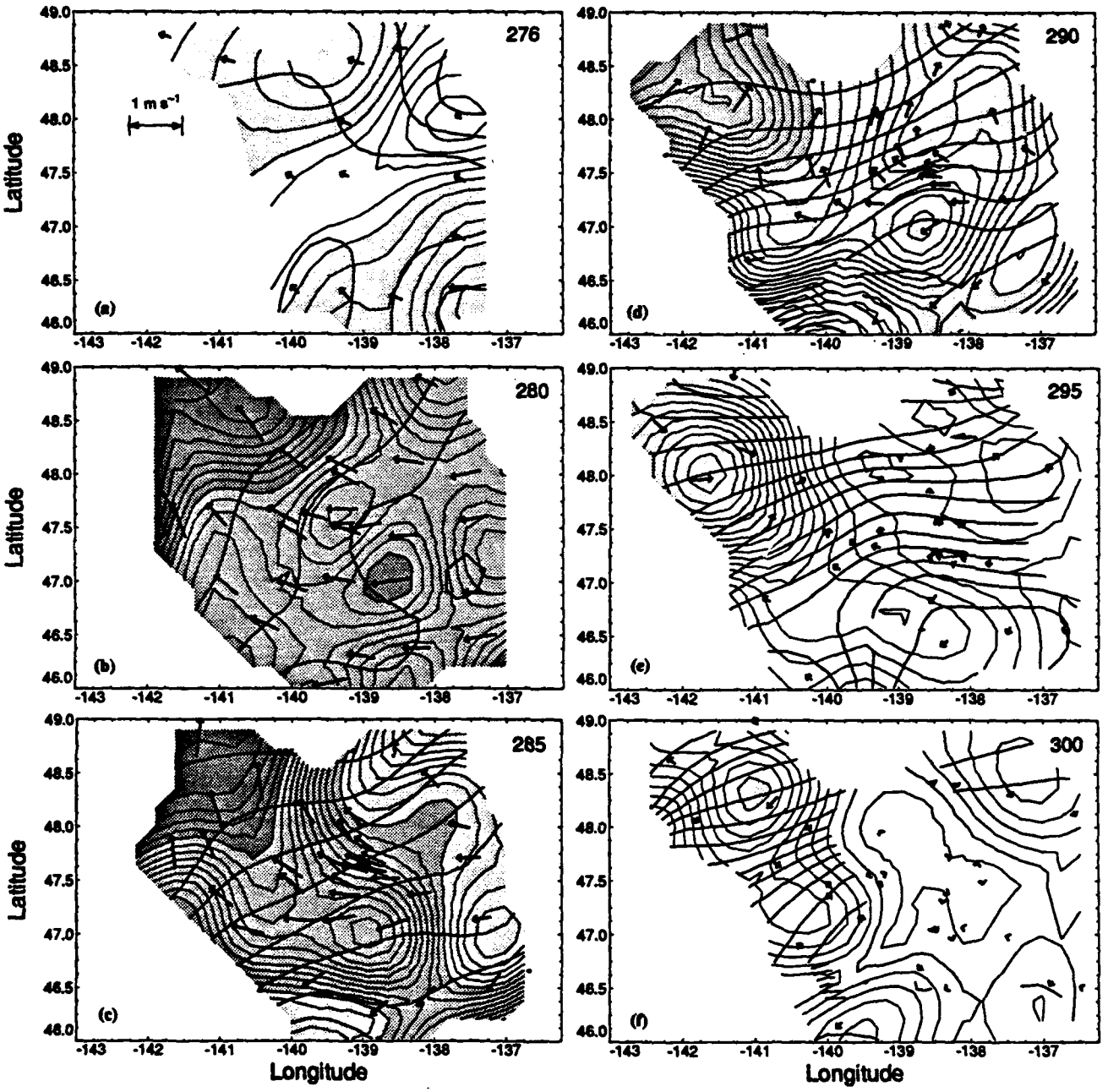

D'Asaro et al., Part I, Fig. 6

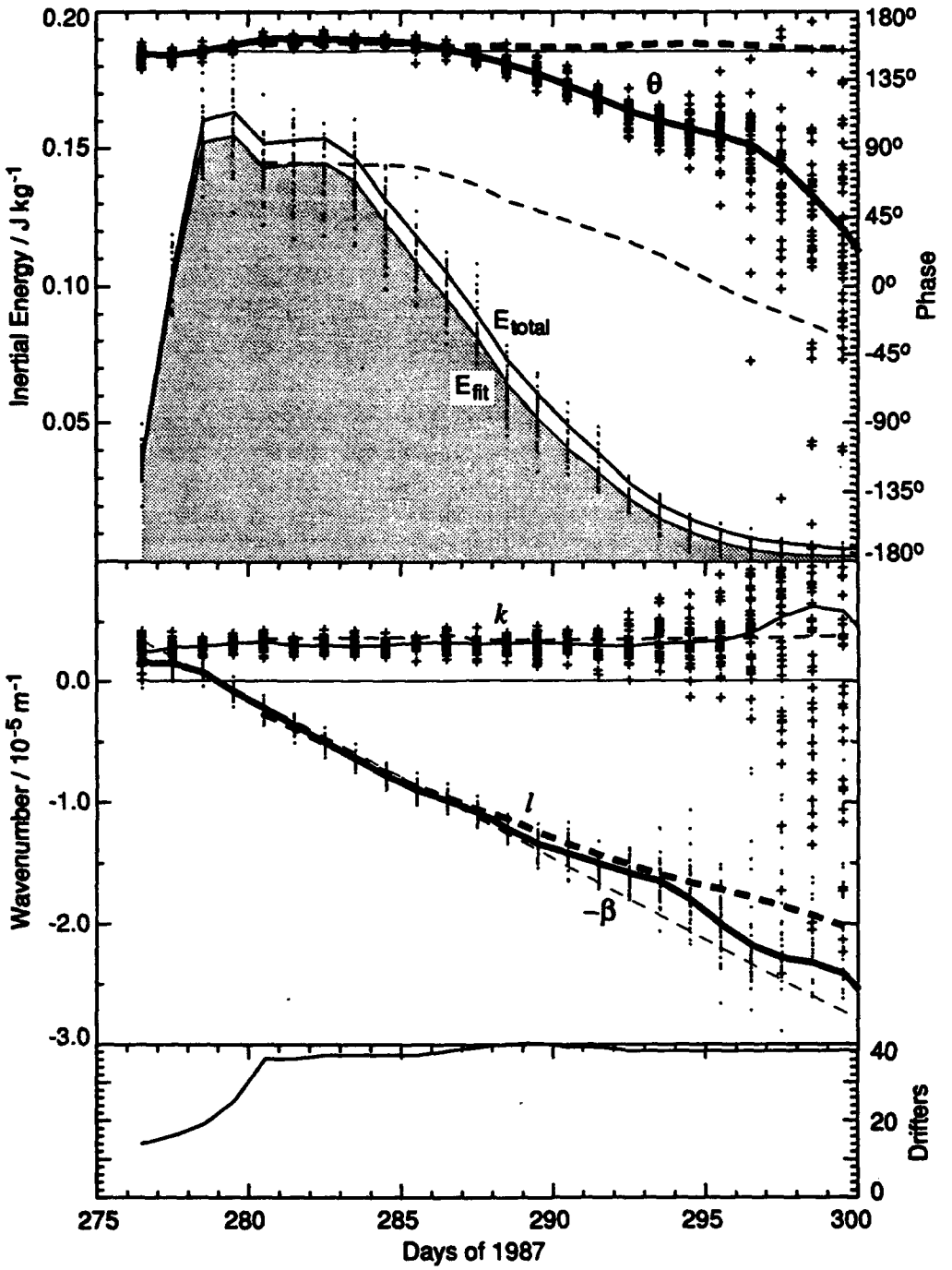

D'Asaro et al., Part I, Fig. 7

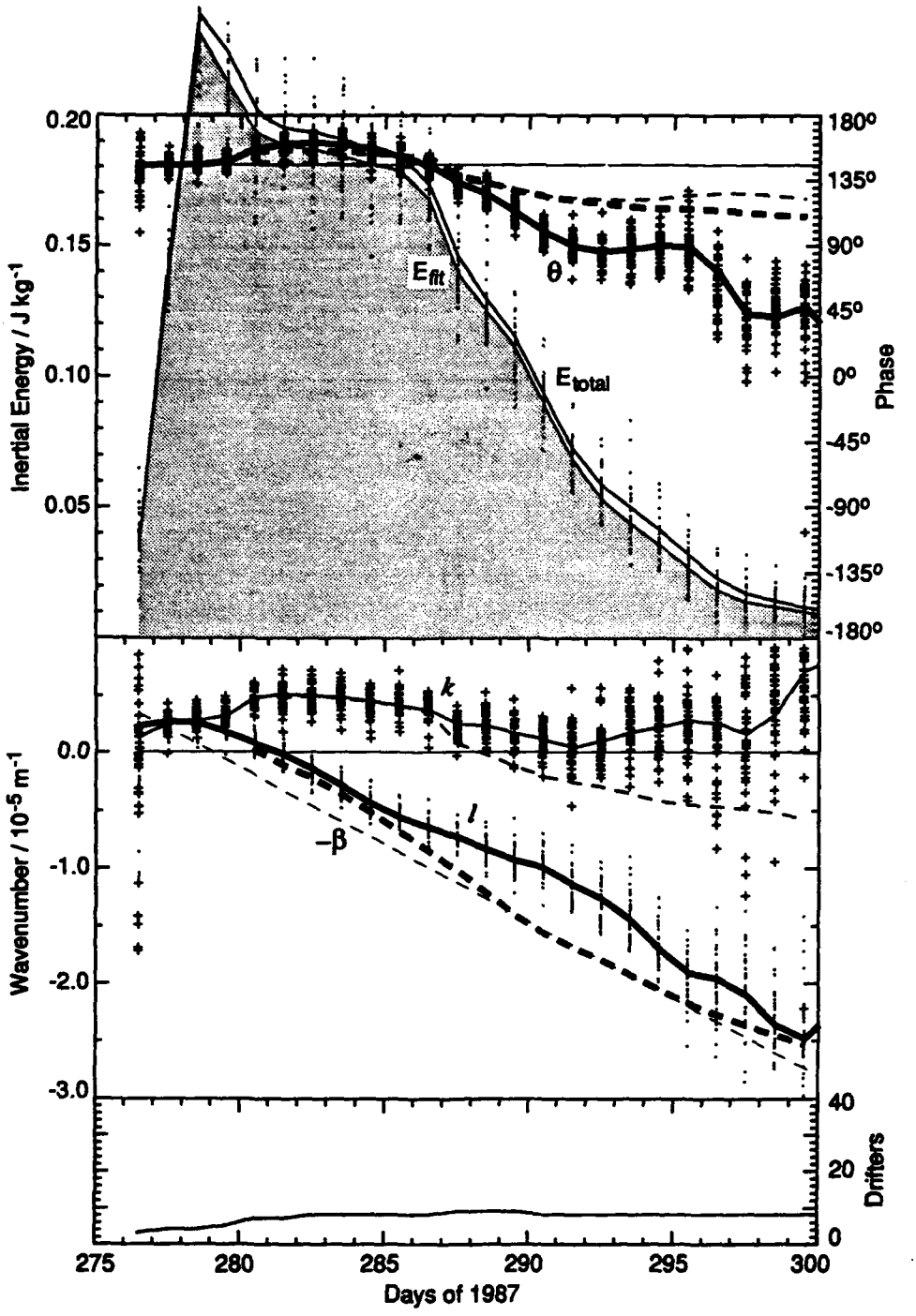

D'Asaro et al., Part I, Fig. 8

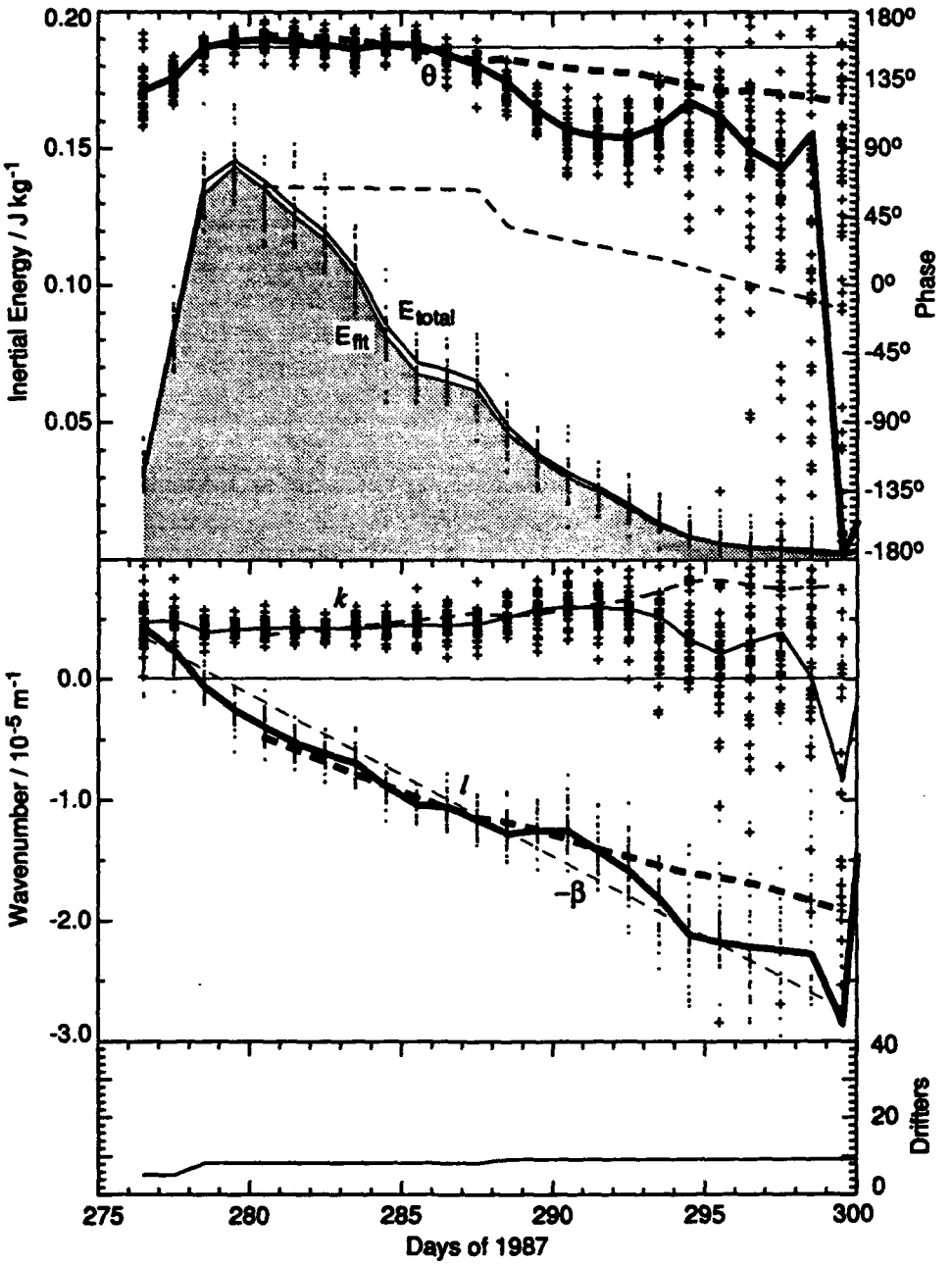

D'Asaro et al., Part I, Fig. 9

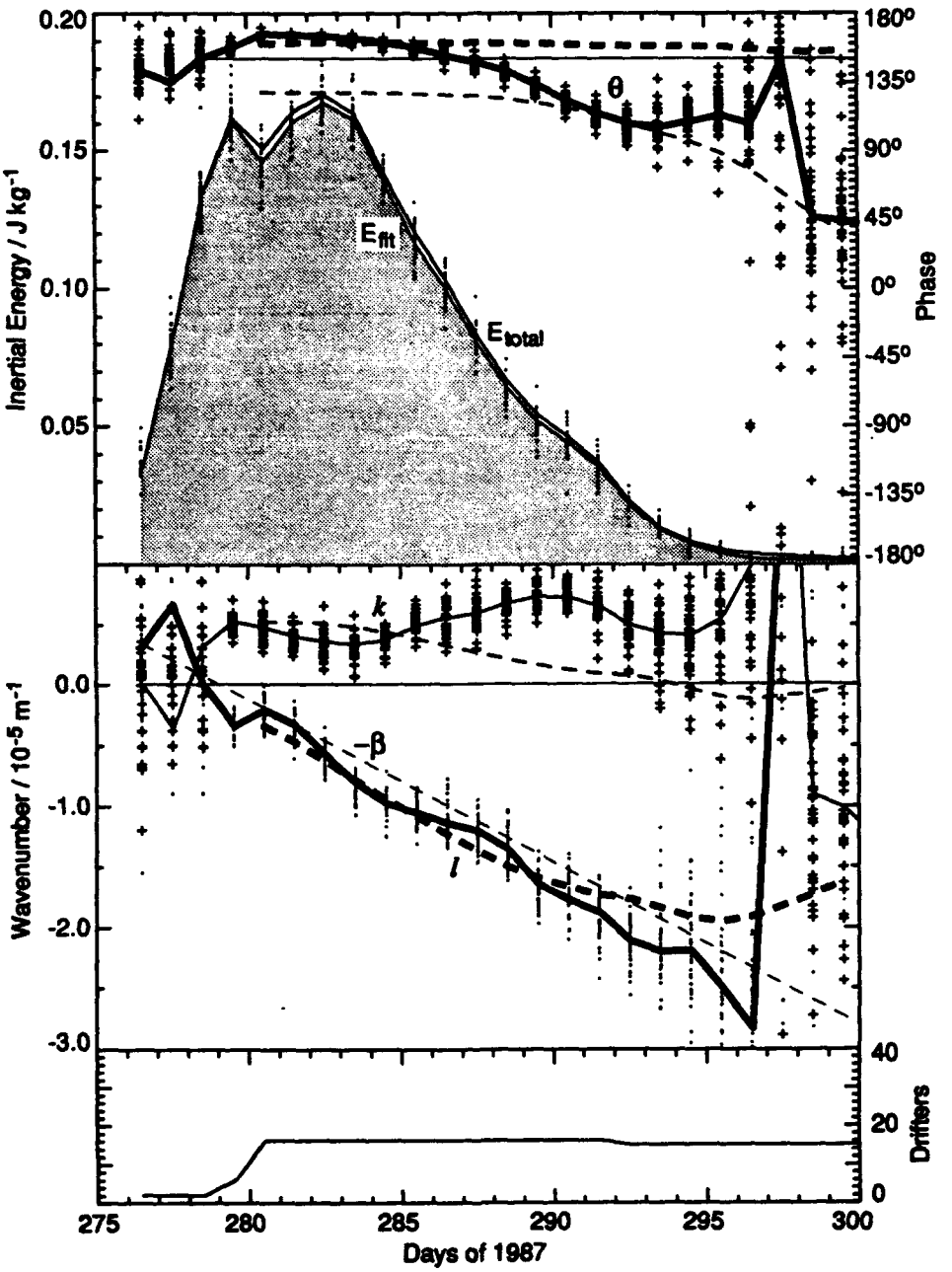

D'Asaro et al., Part I, Fig. 10

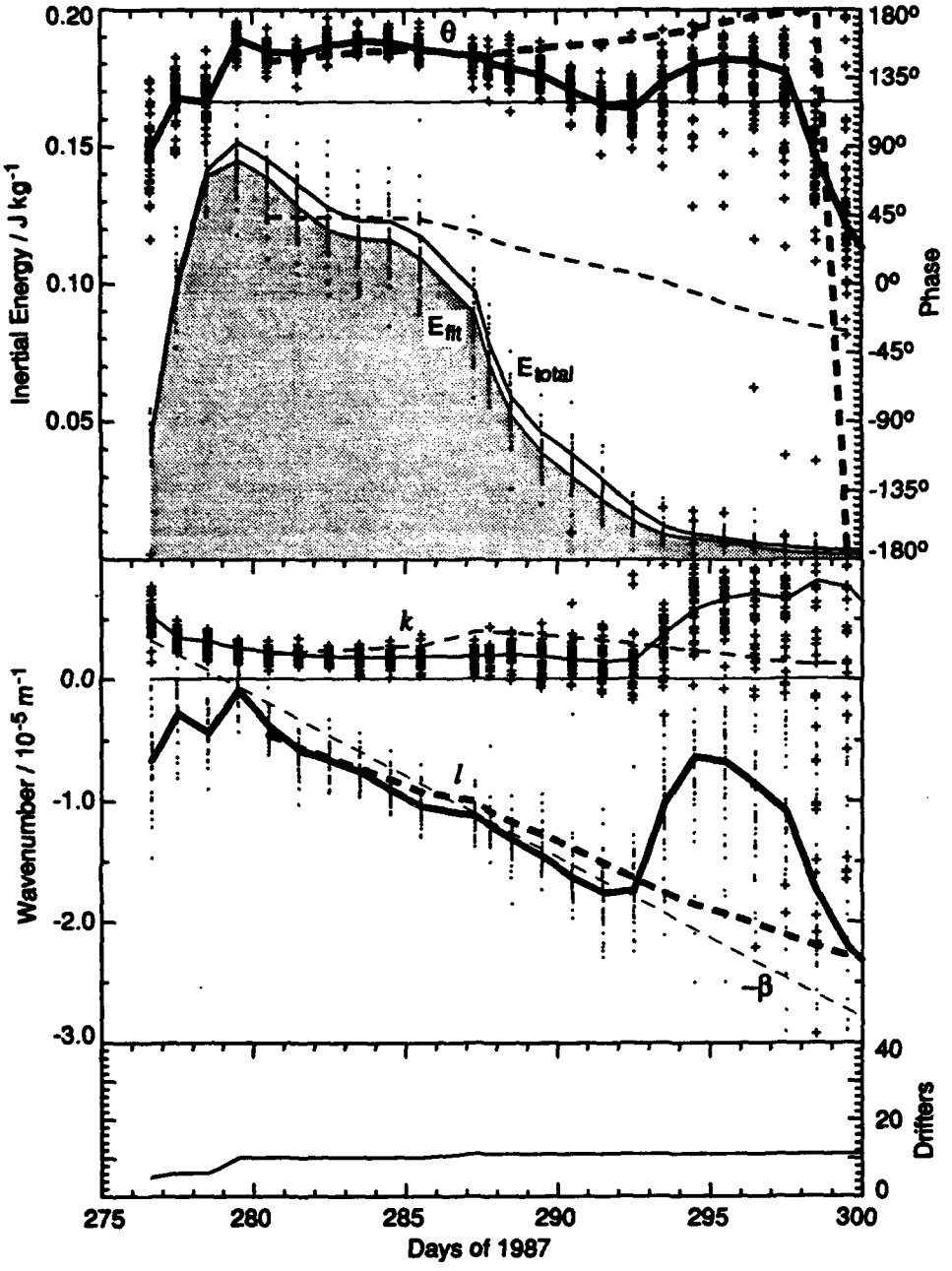

D'Asaro et al., Part I, Fig. 11

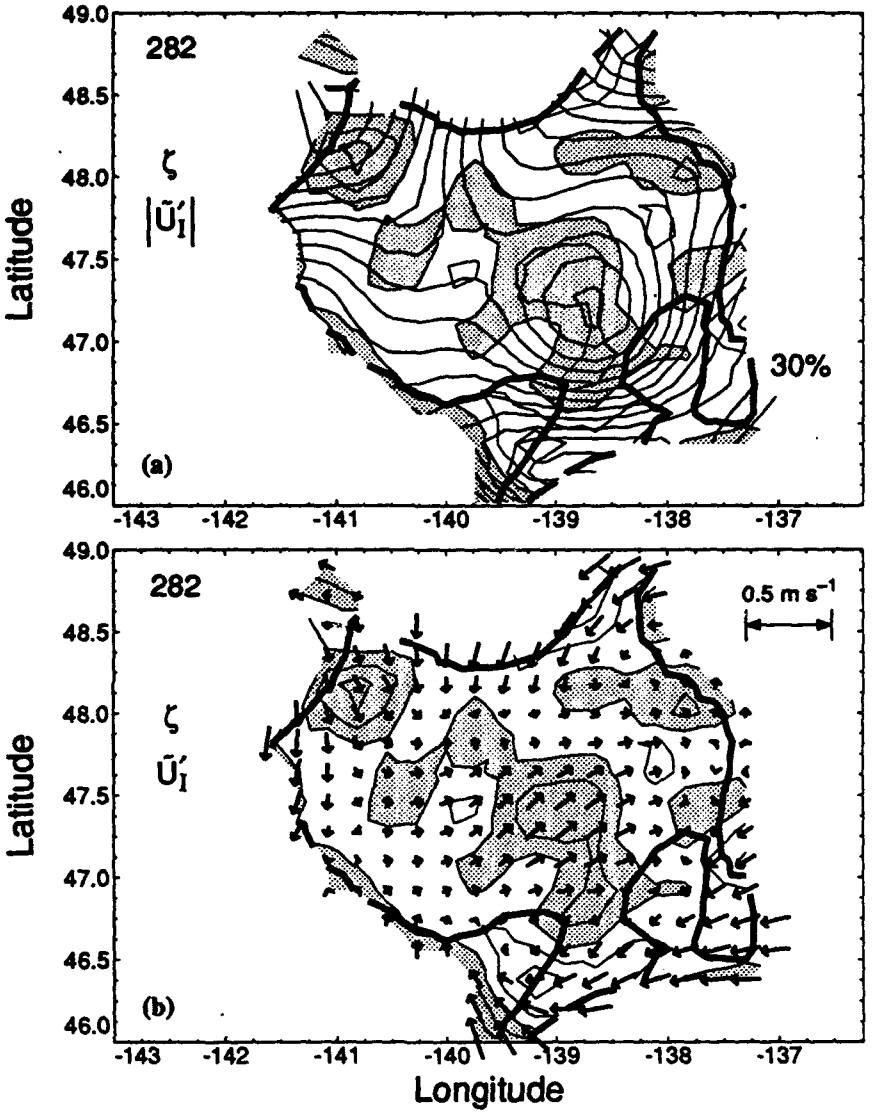

D'Asaro et al., Part I, Fig. 12

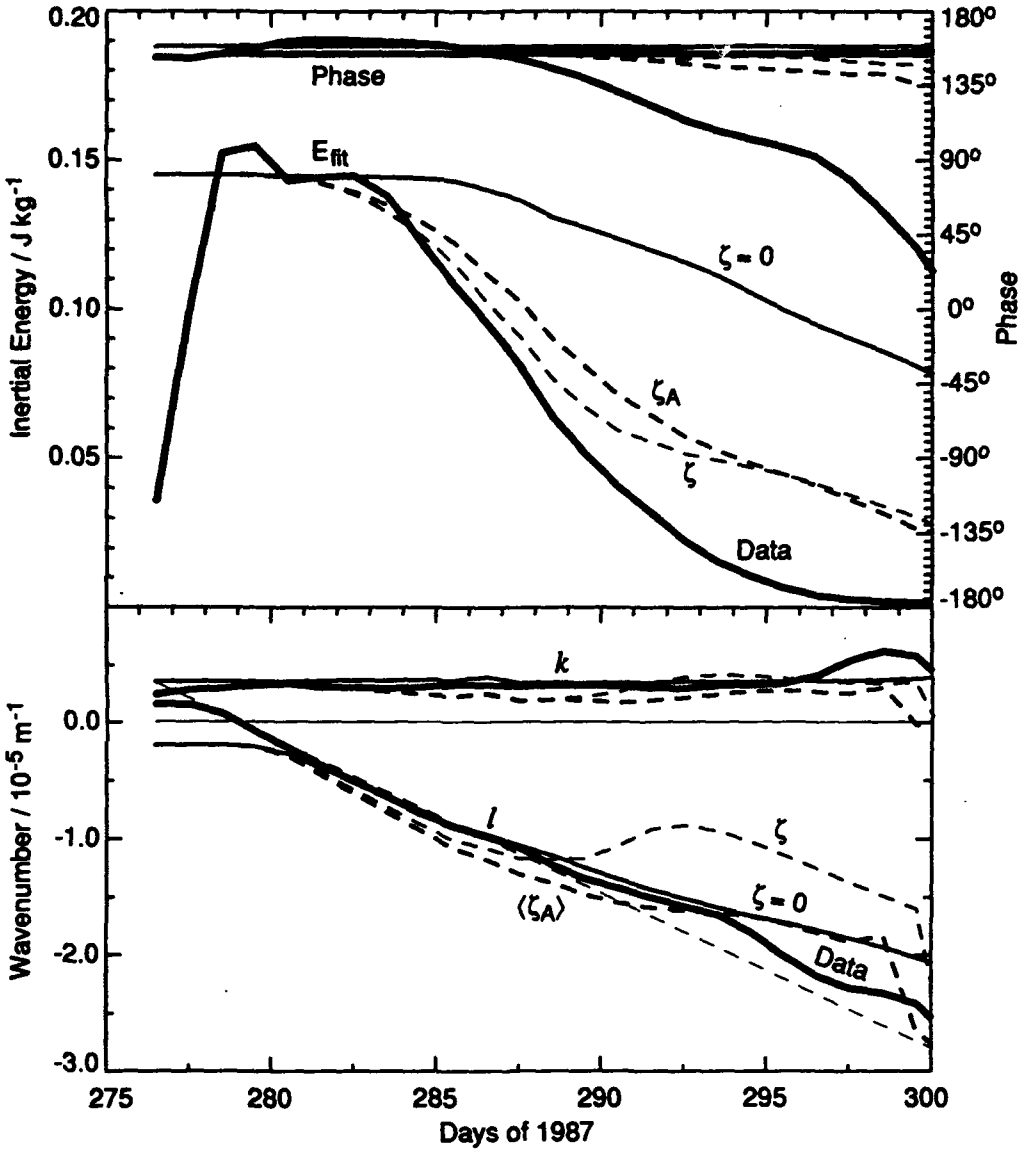

D'Asaro et al., Part I, Fig. 13

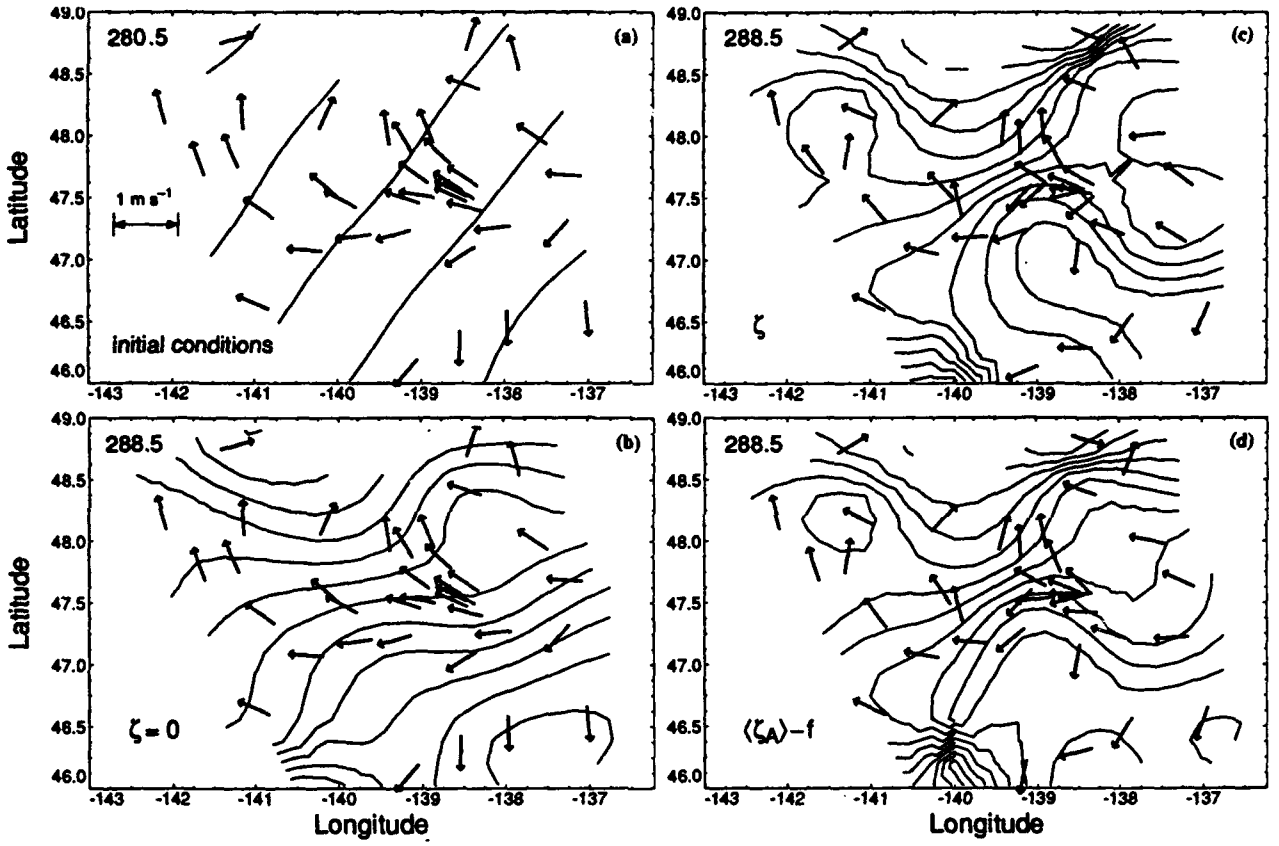

D'Asaro et al., Part I, Fig. 14

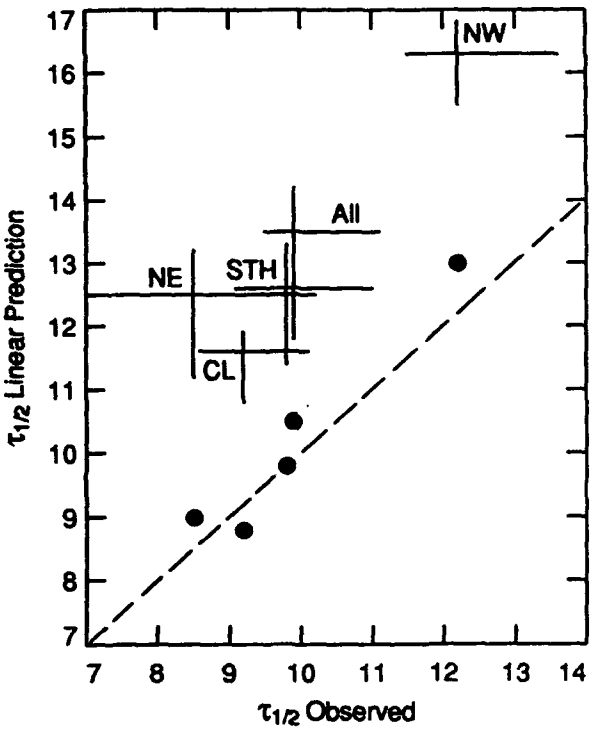

D'Asaro et al., Part I, Fig. 15

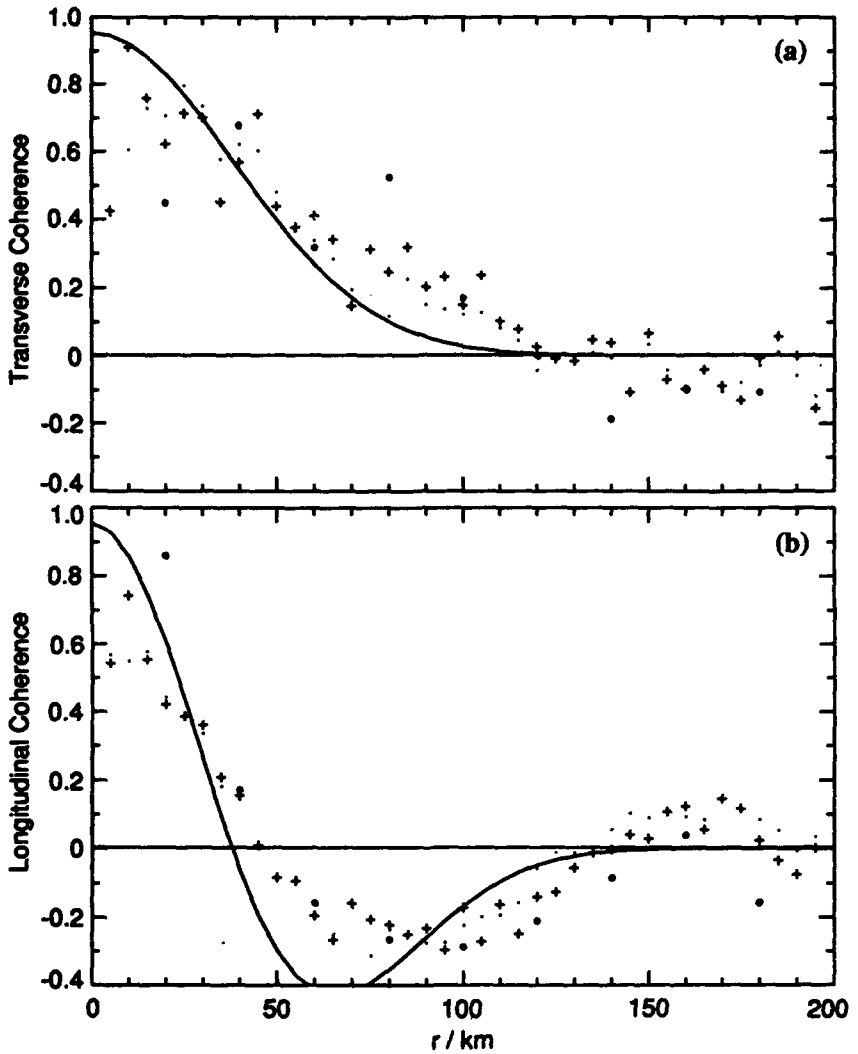

D'Asaro et al., Part I, Fig. A1

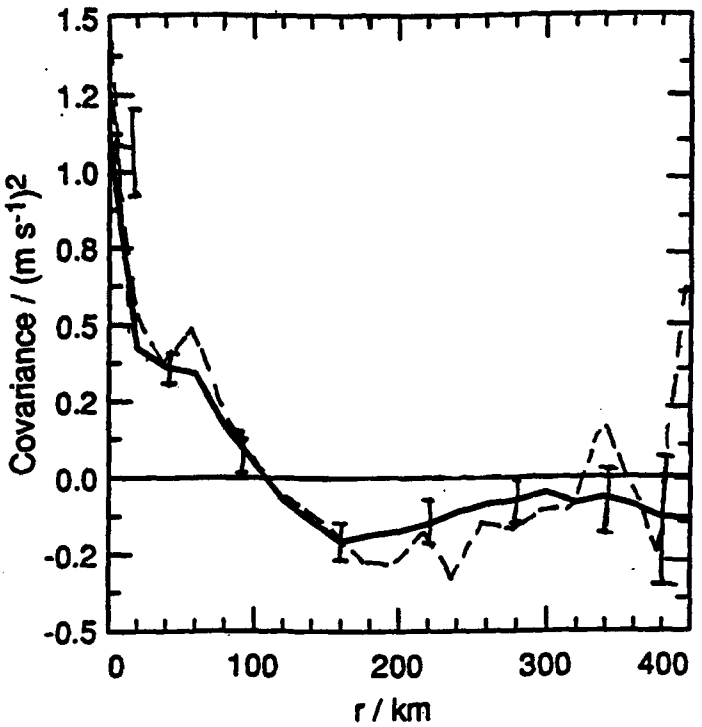

D'Asaro et al., Part I, Fig. A2

Upper Ocean Inertial Currents Forced by a Strong Storm*
II: Propagation into the Thermocline

*Eric A. D'Asaro,** Russ E. Davis,† Charles C. Eriksen,‡ Murray D. Levine,§*

20 December 1993

---

*Contribution Number _____ from the University of Washington School of Oceanography

**Applied Physics Laboratory, College of Ocean and Fishery Sciences, Seattle, Washington 98105

†Scripps Institution of Oceanography, La Jolla, California

‡University of Washington, Seattle, Washington

§Oregon State University, Corvallis, Oregon

ABSTRACT

In Part I, we described the generation of inertial frequency currents in the mixed layer by a strong storm and the decay of these currents over the next month. Here, we expand this description to include inertial currents throughout the full ocean depth using moored and profiling current measurements. Inertial motions propagate downward from the mixed layer into the upper thermocline. By 20 days after the storm, the mixed layer inertial currents are weak and a maximum in inertial energy has been created at about 100 m. The inertial frequency shear, initially concentrated at the mixed layer base, decreases by about a factor of 5 during this period. This pattern occurs over the entire 300 km × 300 km experimental region with only minor variations between locations. A depth-dependent horizontal wavenumber, varying in time due to the β effect, fits the horizontal structure of both the mixed layer and the thermocline inertial currents. The inertial currents rotate clockwise with depth in the thermocline, indicating downward and southward energy propagation. The estimated vertical component of group velocity correctly predicts the observed rate at which the thermocline maximum descends, within large uncertainties. The southward component of group velocity is sufficient to propagate all the energy in the first mode and much of the energy in the second and third modes out of the experimental region in 20 days, roughly consistent with the observed decrease in total water column inertial energy. The modulation of the inertial currents by mesoscale vorticity is much less than predicted. We conclude that the mixed layer iner-

tial currents decay by a combination of southward propagation of the low internal modes and vertical propagation of the higher internal modes. A more detailed comparison of data and theory is presented in Part III.

1. Introduction

Part I (D'Asaro et al. 1994) described mixed layer inertial currents generated by a strong storm in October 1987 during the OCEAN STORMS experiment. Part I showed that the rate of decay of the mixed layer inertial currents was qualitatively consistent with the propagation of inertial energy out of the mixed layer as linear internal waves. In detail, however, linear wave theory was inconsistent with the observations. Here, we look below the mixed layer and describe the evolution of the inertial frequency energy and shear in response to the same storm.

The generation of mixed layer inertial motions by the wind and their subsequent decay have been observed and modeled for nearly a quarter century (Webster 1968; Pollard and Millard 1970; Pollard 1970). The generation mechanism appears to be simple: the momentum imparted to the ocean by the wind stress is distributed nearly uniformly across the mixed layer by turbulence within the mixed layer. The mechanism for decay of these mixed layer inertial motions is less clear, partially because there have been few detailed observations. Linear wave theory (reviewed in Part I) suggests that the horizontal structure of the inertial motions is key to understanding their behavior. Here, we present observations of the three-dimensional structure and evolution of inertial motions using a moored array of six elements, plus a single rapid survey of 31 velocity profiles. These provide an unusually detailed description of upper ocean inertial currents and shear. The inertial currents clearly propagate downward into the thermocline and south-

ward out of the experimental area, at rates that are roughly consistent with group velocities estimated from their spatial scales. This indicates that they evolve, at least in part, as predicted by linear internal wave theory. However, a more detailed analysis, presented in Part III (D'Asaro 1994a), finds that linear wave theory cannot describe these observations correctly in detail.

2. Instruments and data processing

a. Moored array

The moored array is shown in Fig. 1. Davis et al. (1994) describe the instrumentation in detail and present the entire data record.

Four moored Acoustic Doppler Current Meters (ADCP) measured profiles of horizontal velocity once per hour (Davis et al. 1994). Three of these, labeled C, N, and W in Fig. 1, looked upward from about 110 m depth. These produced reliable velocity estimates every 3.88 m to about 25 m. An Argos transmitter measured the position of the surface float of the ADCP moorings. A fourth ADCP, labeled E in Fig. 1, looked downward from 2 m below a surface float and obtained velocity estimates from 7 m to 112 m every 3.88 m. The Argos transmitter failed on this mooring.

A profiling current meter (PCM in Fig. 1) sampled velocity, temperature, and salinity every 10 m over approximately 40–200 m at 4 hour intervals (Eriksen et al. 1982). A subsurface mooring (OSU in Fig. 1) was instrumented with Vector Measuring Current

Meters (VMCM) at 20 m intervals from 60–160 m and at 195 m, and with Aanderaa RCM-5 current meters at 500 m, 1000 m, 2000 m, 3000 m, and 4000 m. These measured currents and temperature at 15 minute (VMCM) and 1 hour (Aanderaa) intervals.

The inertial component of velocity was extracted from each moored record by backrotating the velocity vector to 00Z on day 278 at the inertial frequency corresponding to 47.5°N and averaging these vectors over three inertial periods with a half cosine window. We thus present all inertial velocities with the oscillatory inertial motions removed, so that a velocity vector rotating at the inertial frequency corresponding to 47.5°N is represented as a constant vector. For clarity we will use the term "backrotated inertial vector."

b. Mooring motion removal

The motion of the surface floats of moorings C, N, and W was computed from the Argos fixes, using the objective analysis scheme described in Part I and Davis et al. (1994), and added to the measured ADCP velocities to form an estimate of the true water velocity. The error in the estimated mooring motion is XX cm s^{-1}. The error in its estimated inertial component is XXX, consistent ? with the measured inertial component of mooring motion during times of very small inertial current, about 1.2 cm s^{-1}. The backrotated inertial vector of mooring motion on moorings C, N, and W during the period investigated here is predicted by the linear model

$$S_M = 0.12 S_U , \qquad \theta_M = \frac{\theta_U}{141} - 40^\circ , \tag{1}$$

with an rms error of 0.018 m s^{-1}. S_M and θ_M are the speed and direction of the backrotated inertial vector of mooring motion, and S_U and θ_M are the speed and direction of the backrotated inertial vector measured by the ADCP at 30 m. Since the physical configuration of mooring E is very similar to that of the other moorings, we use (1) to remove the motion from mooring E.

Although no measurements of mooring motion were made at either the OSU or PCM moorings, the magnitude of the motion can be bounded by simple models using the pressure measured near the top of each mooring. A mooring may move horizontally like a pendulum in response to inertial currents. Given the 0.3 m rms inertial frequency pressure fluctuations of the OSU mooring, and assuming, pessimistically, a perfectly stiff, 4000-m-long, mooring pivoting at the ocean floor, we estimate an rms inertial mooring speed of less than 0.5 cm s^{-1}. A mooring may also rotate in a circle, like a precessing top, in response to the clockwise rotation of inertial currents. The maximum sustained vertical descent of the OSU mooring is less than a meter. Again, assuming a 4000-m-long rigid mooring implies an inertial frequency velocity of less than 1 cm s^{-1}. In fact, the buoyancy of the OSU mooring was concentrated below 200 m, while the inertial currents are mostly above this. If we assume, optimistically, that the mooring pivots at 200 m and remains motionless below, the motion of the top of the mooring is about 5 times less than estimated above.

Similarly, the PCM mooring descends a maximum of 10 m, corresponding to a maximum inertial motion of about 3 cm s^{-1}. It also has buoyancy concentrated near 200 m, so the actual motion should be less than this.

Figure 2 shows the backrotated inertial vector at ADCP mooring C before (top) and after (bottom) removal of the mooring motion. The mixed layer base is at about 40 m. Notice the increase in mixed layer energy due to the storm on day 278. Velocities below the mixed layer on days 278–280 in the uncorrected data are due to mooring motion. This pattern does not occur at either the PCM or OSU moorings, indicating that their mooring motion is indeed small and can be safely neglected.

c. AXCP survey

A single survey of Sippican air-expendable current profilers (AXCP) was made on 25 October 1987 (day 298) around the moored array (Fig. 1) using a NOAA WP-3D aircraft as described by D'Asaro et al. (1990). An AXCP measures temperature and the horizontal velocity relative to its conductivity-weighted depth average (Sanford et al. 1982). These were processed as described by Sanford et al. (1982) but with the incremental changes discussed by D'Asaro et al. (1990) and Kennelly et al. (1989). The resulting relative velocity was averaged in 10 m, half overlapping bins between 15 m and 1600 m and has an accuracy better than 0.01 m s^{-1}.

Time since deployment determines the depth of an XCP datum. We estimate the error in depth by matching temperature and velocity features in simultaneous XCPs. D'Asaro and Morehead (1991) found depth differences of about 2 m for a pair of XCPs dropped through adjacent holes in the Arctic pack ice. Since the NOAA WP-3D had only a single drop chute, AXCP pairs deployed during OCEAN STORMS exited a few seconds (a few hundred meters) apart. Two pairs were dropped; each showed depth differences of less than 2 m in the upper 200 m and less than 4 m in the 600–1000 m depth range.

Above about 50 m, surface wave velocities often dominate the signals measured by XCPs. Although this signal can be partially removed by fitting a surface wave profile to the data (Sanford et al. 1987; D'Asaro 1994b), this technique is ineffective here, as the mixed layer is too shallow. We choose instead to ignore AXCP data above 50 m.

Frequency spectra. We will need frequency spectra of velocity to interpret the AXCP profiles. Spectra of horizontal velocity from the OSU mooring for days 278–304 (Fig. 3) reveal a strong inertial peak at all depths, a slight shoulder corresponding to the semidiurnal tide, a broad peak near $2f$, and the usual internal wave band. The near-inertial frequencies are clearly the most energetic component. Figure 4 shows the energy in the subinertial (<1.33 cpd), inertial (1.33–1.66 cpd), and superinertial (>1.66 cpd) frequency bands as a function of depth for days 277–304 from the OSU mooring. The mixed layer subinertial and inertial kinetic energy is estimated from the drifter data

(Part I), and the mixed layer superinertial energy from the 59 m VMCM. The inertial band contains more than 80% of the energy at all depths in the upper 150 m, but drops to about 50% of the energy below 1000 m.

Inertial velocity component. We interpret the referenced AXCP velocities as inertial currents plus an error due to noninertial components and AXCP errors.

We reference the relative AXCP velocity profiles to the 1400–1600 m average velocity, thus making them absolute with a depth-independent error equal to the rms currents at this depth, about 0.045 m s^{-1} (Fig. 4). Alternative schemes—such as using the velocities directly from the AXCP, equivalent to using the electromagnetically determined barotropic flow as a reference, or using different reference levels—make little difference in the results.

The high frequency internal waves have horizontal coherence scales that are short compared with the AXCP spacing (D'Asaro and Perkins 1984) and therefore contribute a random error of about 0.07 m s^{-1} at 100 m.

We partially remove the low frequency contribution to each AXCP profile by interpolating the near-surface velocity field from the drifters (Fig. 2a of Part I) to the position of each AXCP. Matear (1993) and Part I find that the geostrophically determined subsurface velocity is highly correlated with the surface flow, so we construct a profile of velocity at each AXCP using the correlation function described in Part I. To form our estimate of the backrotated inertial vector, we subtract this velocity profile from each AXCP

profile and then back-rotate the residual to 00Z day 278 at the inertial frequency corresponding to 47.5°N. The residual low frequency error is less than the rms variability of the low frequency velocity, 0.06 m s^{-1}.

We bound the error in AXCP inertial velocity from above as that due to all of the preceding factors, 0.1 m s^{-1}, since we have partially compensated for the low frequency flow and because the error in referencing is correlated with the other errors. We bound it from below as larger than the high frequency error alone, 0.07 m s^{-1}. We check these bounds by applying the same procedure to the instantaneous moored velocity profiles from the PCM and OSU moorings at the time of the AXCP survey. In the 60–200 m depth range, the resulting profiles differ from the true demodulated inertial vector profiles by 0.04 and 0.07 m s^{-1} rms, for the OSU and PCM moorings, respectively, with maximum errors of 0.09 and 0.14 m s^{-1}.

3. Moored data

a. Temperature and density

Mixed layer depth. CTD profiles on days 277–280 (Tabata et al. 1988; Matear 1993) measured mixed layer depths from 33 m to 43 m from 5 profiles within 30 km of the OSU mooring and mixed layer depths from 33 m to 49 m from 15 profiles within 120 km of the moorings. The AXCP survey on day 298 measured mixed layer depths ranging from 35 m to 40 m; in some profiles the mixed layer is poorly defined. This vari-

ability is comparable to the 8 m, peak to peak, tidal and inertial frequency displacements in the upper thermocline measured in the PCM data. Moored temperature data at mooring C (Davis et al. 1994) show an average mixed layer about 35 m deep during this period. The average mixed layer depth is thus a few meters above the top of the PCM mooring (40 m).

Evolution. The evolution of the density and temperature in the upper 200 m at the PCM and OSU moorings is shown in Figs. 5c,d and 6d. The isotherms and isopycnals spread and deepen in the upper 80 m during the storm on day 277 and for several days thereafter. A more detailed analysis of the associated mixing is given by Crawford and Large (1994a,b). Before and after the storm, the isopycnals are remarkably free of subinertial variations, consistent with the low levels of mesoscale activity described in Part I. Some activity is evident in the PCM data near day 275 and in the OSU data near day 300. These may be related to the near-surface fronts that appear both in the drifter data (Paduan and Niiler 1993) and in closely spaced yo-yo profiles of density (William Crawford, personal communication).

b. Inertial velocity: Data

The backrotated inertial vector from the moorings is shown in Figs. 5–10. The inertial currents are very similar at all moorings. In each, inertial currents are generated in the mixed layer by the storm and spread downward into the thermocline over the next 30 days. The evolution of these currents is the focus of this paper.

We form an average picture of the inertial evolution at the four ADCP moorings by fitting the backrotated inertial vectors at each depth and time by a plane wave. With complex notation, the backrotated inertial vectors are $U = u_I + iv_I$. These are fit with the model

$$U(x,y) = \tilde{U}e^{i(kx+ly)} + U_R(x,y)\,, \tag{2}$$

using the algorithm described in the appendix of Part I. Here $\tilde{U}$ is the complex wave amplitude, k is the east-west wavenumber, l is the north-south wavenumber, and U_R is a residual. The phase of $\tilde{U}$ is set by referencing x and y to the position of the PCM mooring. The resulting backrotated inertial vectors are shown in Fig. 11, and the wavenumbers in Fig. 12. Over most of the domain, (2) accounts for over 90% of the data variance, which is not surprising since (2) has four free parameters and we are fitting five data points. More striking is the remarkable similarity between the average picture in Fig. 11 and that from the PCM (Fig. 5a,b).

F 11, 12

c. Inertial velocity: Description

We describe the evolution of the inertial currents in a series of stages:

Generation. The storm on day 277 generates inertial currents in the upper ocean as described in Part I and Crawford and Large (1994a,b). Note that these currents penetrate to about 60 m, well below the mixed layer, at all moorings. The thermocline warms during the storm to the same depth (Figs. 5d, 6d). Crawford and Large (1994a,b)

attribute these changes to turbulent mixing that penetrates below the mixed layer.

Spreading. For the first week after the storm (days 278–285) the inertial currents spread slowly downward into the thermocline with only a slight clockwise veering of the backrotated inertial vectors with depth, i.e., a slightly negative phase shift in $\tilde{U}$. On average, the inertial currents penetrate to about 75 m by day 284, although the amount of penetration varies between moorings. The density and temperature profiles change only slightly during this time. A vertical viscosity of around 10^{-4} m^2 s^{-1}, without an associated diffusivity, qualitatively describes the evolution.

Formation of the beam. On about day 284, the mixed layer inertial currents begin to move downward into the upper thermocline, so by day 300 the strongest inertial currents are at 100 m and little energy remains in the mixed layer. During this period, the frequency of the inertial currents rises from about f to roughly $1.01f$, and the 100 m inertial currents lead those in the mixed layer by roughly 60°. This pattern resembles a beam, or packet, of near-inertial waves propagating downward from the mixed layer. We name this thermocline maximum in near-inertial energy "the Beam."

The horizontal wavenumbers derived from fitting (2) to the moored data are shown in Fig. 12. We only plot data for which $|\tilde{U}| > 0.1$ m s^{-1}, since only these appear stable. For comparison, the solid lines show the approximate horizontal wavenumbers computed for subgroup CL in the mixed layer in Part I. The east-west wavenumber k is nearly constant, in both the mixed layer and below, while the north-south wavenumber l increases

as $-\beta t$, where $\beta = f_y$. The value of l is somewhat below the dashed line, as was found for the CL group. As the inertial energy propagates downward from the mixed layer it retains its horizontal structure, as expected for linear wave propagation.

Persistence of the Beam. From day 295–305, the Beam persists with some weakening and a slight deepening. The wind forcing increases after day 298. Stronger storms pass over the OCEAN STORMS area after day 305, new inertial motions are generated, and the evolution of the inertial motions due to the storm can no longer be followed.

d. Deep inertial currents

The deep data from the OSU mooring (Fig. 6c) suggest an inertial frequency response that extends to the ocean bottom. A downward extension of the Beam, with enhanced inertial currents and clockwise veering with depth, extends to about 1000 m. Below this, the inertial currents reach a minimum near 2500 m and then increase toward the bottom (4200 m). The inertial direction changes by about 180° across the speed minimum. Overall, the pattern in the bottom 3000 m on days 290–305 is suggestive of a low mode with a node near 2500 m.

e. Inertial shear

The inertial shear, computed from the vertical first difference of the backrotated inertial vectors in Fig. 11, is shown in Fig. 13. The storm generates a strong inertial shear between the mixed layer base and about 70 m. The shear weakens over the next week

(the "spreading phase") so that by day 285 the maximum shear is about half its initial value. As the Beam forms, the shear weakens further and deepens. By day 290 there is little shear left at the mixed layer base, and the remaining shear is associated with the Beam. After day 300 the shear near the mixed layer base increases again, probably because of renewed wind forcing.

4. AXCP survey data

The moored data span a region approximately 50 km by 100 km. On day 298 a larger region, 125 km by 150 km surrounding the moored array, was surveyed using AXCPs (Fig. 1). We now describe the three-dimensional structure of the inertial velocity at that time.

a. Maps

The backrotated inertial vectors at 100 m (Fig. 14, heavy arrows) have a nearly constant amplitude of about 0.25 m s^{-1}. Their direction at 100 m (heavy arrows, contours), at 75 m (light arrow, smallest arrowhead), and at 140 m (light arrow, largest arrowhead) rotates counterclockwise to the SSW, implying an increasing phase or equivalently a horizontal wavenumber pointing in this direction. Generally the direction rotates clockwise with increasing depth (i.e., with larger arrowheads), consistent with an upward pointing wavenumber. F14

b. Sections

Sections of backrotated inertial vectors along each of the three legs of the AXCP survey (Fig. 1) are shown in Figs. 15–17. The sections are computed from moored, AXCP, and drifter backrotated inertial vectors; each drifter vector (from Part I) is reproduced at 15 m, 20 m, and 25 m. These data were horizontally interpolated to the section using two-dimensional smoothing splines (Craven and Wahba 1979) with essentially no smoothing. The location of the data along the section is indicated by triangles whose size indicates the perpendicular distance (0–20 km) from the section to the data. Only the PCM, OSU, and C moorings are close enough to a section to merit a triangle.

The Beam is present everywhere in these data; every velocity profile has a maximum in inertial energy between 100 m and 150 m. Section A (Fig. 15) is oriented approximately perpendicular to the direction contours in Fig. 14, so it clearly shows the clockwise rotation of the inertial direction to the north. The other two sections are nearly parallel to the direction contours and therefore show the progression less clearly. In all three sections, the clockwise rotation of the backrotated inertial vector with depth is apparent.

For the most part, the inertial currents in the mixed layer are weak. In the few regions where they are strong enough that their direction is well determined (about 0.05 m s^{-1}), the backrotated mixed layer inertial vectors are about 90° clockwise of those in the Beam.

Inertial currents generated by the storm extend well below the Beam (Fig. 6c). Their spatial structure is seen in the AXCP survey (Figs. 15–17) and in Fig. 18, which plots the currents within the Beam (100 m, smallest arrowhead) and below it (250 m, heavy; 600 m, largest arrowhead). The currents below the Beam show little variation in direction, in contrast to the clear direction progression in the Beam. This results in a change in direction across the Beam which, in Fig. 15, varies from about 180° near 70 km to only 45° near 150 km.

c. Wavenumbers

We fit a plane wave (2) to the survey data, as described in the appendix of Part I, and compute the average amplitude, direction, and wavenumbers of the backrotated inertial vector at the time of the survey (Fig. 19). Confidence limits in these parameters were determined using a Monte Carlo simulation as described in the appendix. The small symbols give the parameter values from 50 such realizations; 95% confidence limits are located between the second and third and 47^{th} and 48^{th} ranked values. The difference between the energy in the fit (shaded region, top panel) and the total energy (line, top panel) is about 0.007 J kg^{-1} near 100 m, which is about 3 times the estimated demodulation error of 0.0025 J kg^{-1} (0.07 m s^{-1}). Equivalently, the fit explains about 75% of the inertial energy, when corrected for the noise energy.

The maximum in inertial energy near 110 m is the Beam. Its direction is about 130° clockwise of the inertial vectors initially generated by the storm, and turns approximately

135° clockwise between 80 m and 140 m. The peak speed is about 0.22 m s^{-1}, and the half-energy width is about 80 m. Above the Beam, the direction rotates clockwise upward about 70° into the mixed layer, although this number is less reliable than it appears, owing to the very weak mixed layer inertial currents (see Part I). Below, the direction rotates clockwise, but the variation is barely significant.

The k and l wavenumbers at the center of the Beam are nearly statistically indistinguishable from those in the mixed layer at this time. They are also close to those computed just from the ADCP data at this time (Fig. 12, error bars). Again, it seems clear that the Beam acquires its horizontal wavenumber from the mixed layer.

Below the Beam both k and l fall to nearly zero by 200 m. There are few moored data here, and the AXCP data are less accurate, so the significance of this is unclear.

d. Spatial variability

The spatial structure is not totally described by the fit parameters in Fig. 19. In Figs. 15–17 the maximum speed in the Beam varies (0.1–0.3 m s^{-1}) as does its depth (95–140 m). These variations are spatially coherent, as seen by the speed contours in Fig. 14, unlike the error, which is dominated by incoherent internal wave noise. Furthermore, the maximum inertial speeds in the Beam on day 298 measured at the six moorings vary from about 15 cm s^{-1} to 32 cm s^{-1}, greatly exceeding the measurement error.

5. Dynamical tests

a. Residence time

The inertial currents remain in the mixed layer for 10–20 days after the storm. As discussed in Part I, this time is nearly consistent with the predictions of D'Asaro (1989) for storm forced inertial currents on a β plane. The decay of shear on the same time scale as velocity is not predicted by this theory.

b. Ray propagation

Qualitatively, the propagation of energy from the mixed layer into the thermocline looks like the linear propagation of a wave packet. Qui et al. (1994) explore this in great detail using only data from the OSU and PCM moorings. Here we use wavenumber data as well. We can compare the frequency and wavenumbers of the packet with those predicted by the internal wave dispersion relation, and we can compare the motion of the packet with that predicted by the group velocity. The WKB scaled dispersion relationship for linear near-inertial waves is (Gill 1984)

$$\omega - f = \frac{N^2}{m^2}\,\frac{\alpha^2}{2f}\,, \tag{3}$$

where ω is the wave frequency, $\alpha^2 = k^2 + l^2$; k, l, and m are the east, north, and vertical wavenumber components, and N is the local buoyancy frequency. The vertical group speed is

$$G_Z = -2\frac{\omega - f}{m} . \tag{4}$$

We use $N = 0.012\ s^{-1}$ (Part III, Fig. 11). We compute wavenumbers for each of the 40 Monte Carlo realizations; m is computed from a least squares fit to the phase slope between 90 m and 130 m and between 70 m and 150 m to yield 160 total realizations. The median [95 percentile limits] value of m is 0.029 $[0.017, 0.037]\ m^{-1}$, of α is 2.2 $[2.1, 2.4] \times 10^{-5}\ m^{-1}$, and of $(\omega - f)/f$ is 0.004 [0.002, 0.007]. The resulting vertical displacement at the group speed in 10 days is 24 [10, 119] m. The large variability in the group speed is due to the inverse cubic dependence of G_Z on m.

We compare this with the observations of the Beam on days 290–305. In Figs. 5b and 6b, the frequency of the Beam is approximately $1.005f$. The depth of maximum velocity descends about 40 m in this time at the PCM mooring (Fig. 5), and 20 m or less at the OSU mooring (Fig. 6a). This agrees with the group velocity predictions above, but the large errors provide only very weak verification of linear theory.

The above calculation does not address the issue of how the Beam is formed from the initially uniform mixed layer currents. The more detailed modeling in Part III and in Zervakis and Levine (1994) demonstrates that linear theory does not replicate the observed separation of the Beam from the mixed layer.

c. Spatial variability

We can also estimate whether the spatial variability of the Beam could be due to a

mesoscale eddy field. One effect of mesoscale currents is to shift the frequency of free inertial currents from f to $f_{\text{eff}} = f + \frac{1}{2}\zeta$, where ζ is the vorticity of the background flow (Kunze 1985; Smith 1973; Part I). Variations in f_{eff}, acting over a time T, will produce variations in initially uniform inertial currents described by

$$u + iv = \tilde{U}(x,y,z)\, e^{-if_{\text{eff}}(x,y,z)T} . \tag{5}$$

The linear increase of l seen in Fig. 12 is a special case of (5) in which only β contributes to f_{eff}.

Figure 20 (light contours) plots f_{eff} using ζ in the mixed layer from Part I. Although F20
the general north-south trend induced by β is evident, the gradients in f_{eff} are much larger than β. Superimposed (dark contours) are the measured contours of inertial direction from Fig. 14, plotted so that if (5) were correct the light and heavy contours would coincide. Clearly, they do not. The observed variations in direction are roughly 4 times less than predicted by (5). The mesoscale variations in inertial direction are much less than would be expected from the measured variations in vorticity.

6. Energy balance

In Figs. 3 and 7 of Part I, we estimate the average mixed layer inertial energy density generated by the storm using the array of surface drifters. For the entire array we find 0.14 ± 0.01 J kg^{-1}; for the CL region near the AXCP drops and the moorings, we find 0.16 ± 0.01 J kg^{-1}. The moorings (Figs. 5–12) show that these currents are nearly uniform across the mixed layer and extend somewhat below it; the total inertial energy

put into the ocean by the storm, $8.4 \pm 0.6 \times 10^3$ J m^{-2}, is obtained by assuming that the near-surface velocities extend uniformly to 55 m.

On day 298, the survey (Fig. 19) finds a total inertial energy, uncorrected for noise, of $5.2 \pm 0.3 \times 10^3$ J m^{-2} in the upper 1000 m; the error is the standard deviation of the total energy computed from the Monte Carlo realizations. From the OSU mooring (Fig. 6c), the total energy above background levels and below 1000 m is $1 \pm 0.5 \times 10^3$ J m^{-2}. The total inertial energy over all depths is thus $6.2 \pm 0.6 \times 10^3$ J m^{-2}.

The coherent energy on day 298, i.e., that fit by (2), is $3.2 \pm 0.3 \times 10^3$ J m^{-2} in the upper 1000 m. Assuming the same proportion of fit to total below 1000 m, the water column coherent energy is $3.8 \pm 0.3 \times 10^3$ J m^{-3}. A bit less than half of this, 1.5×10^3 J m^{-2}, is in the upper 150 m.

Using these numbers, the total water column's inertial frequency energy on day 298, 21 days after the storm, is 74 ±7% of the initial energy. Only 45 ± 5% of the initial energy is described by (2) on day 298. Only 18% is both described by (2) and in the upper 150 m on day 298. That is, only 18% is in the Beam.

Near-inertial internal waves are very close to their critical latitude and thus cannot propagate much farther northward (Munk and Phillips 1968). They therefore tend to propagate southward from their generation region. The horizontal group velocity of the n^{th} vertical baroclinic mode of near-inertial frequency gravity waves is

$$G_H = c_n^2 \frac{\mathbf{k}}{f} \tag{6}$$

where c_n is the phase speed of the mode. The horizontal wavenumber **k** obtained from (2) (Figs. 12 and 19) points to the SSE at all depths with an average magnitude of about 10^{-5} m^{-1}. Using the c_n in Table 2 of Part III, this implies a horizontal group speed for the first four baroclinic modes of, respectively, 0.5, 0.16, 0.08, and 0.04 m s^{-1} or, equivalently, 860, 280, 140, and 74 km horizontal propagation in 21 days.

The storm on day 277 generated large inertial currents because its motion and structure conspired to rotate the wind stress clockwise at almost exactly the inertial frequency. (Crawford and Large 1994a,b). The storm center passed about 500 km north of OCEAN STORMS. Much weaker inertial currents were probably generated north of the storm center, as the wind turned counterclockwise with time there. We estimate, therefore, that strong inertial currents were generated in a region that extended at most 500 km north of the OCEAN STORMS array. Mode 1 can clearly propagate out of this generation region in 21 days, while modes 2 and 3 can only partially do so. Using a realistic initial velocity profile, Table 2 of Part III shows mode 1 carrying 15% of the total inertial energy, modes 1 and 2 carrying 49%, and modes 1–3 carrying 70%. The observed 45–75% decrease in water column inertial energy in 20 days is consistent with mode 1 and part of modes 2 and 3, propagating southeastward out of their generation region.

Figure 13 shows a large decrease in upper ocean shear over these same 20 days. These low modes contribute little to the shear profile; the higher modes, which do

contribute, propagate little in 20 days. The decrease in shear, therefore, is not explained by these simple linear ideas.

7. Summary

Observations of the three-dimensional structure and evolution of inertial currents generated by a strong storm show that

- Inertial currents are clearly generated by the storm and propagate into the thermocline over a period of 20 days.
- The inertial currents generated by the storm extend 20–30 m below the mixed layer immediately after the storm. Turbulent mixing is responsible for this (Crawford and Large 1994a,b).
- Propagation starts as a spreading of the inertial currents approximately 10–30 m into the upper thermocline over the first 10 days, followed by a more rapid propagation of energy out of the mixed layer and into the upper thermocline. The net result is a maximum in inertial energy at a depth of about 100 m ("the Beam"), which persists for the next 10 days.
- The transfer of energy out of the mixed layer is accompanied by a clockwise turning of the inertial currents with depth and a slightly superinertial frequency.
- Twenty days after the storm, the Beam is present at all stations within the 150 km × 150 km array and exhibits a phase propagation to the southwest with a wavelength of

about 300 km.

- Significant smaller scale deviations from this large-scale structure occur.

- Below the Beam, significant storm-forced inertial currents exist to at least 1500 m depth and possibly below. These motions have a horizontal wavenumber that is barely distinguishable from zero and clearly smaller than that in the Beam.

- The total water column inertial energy decreases to about 74% of its initial value in the 20 days after the storm. The fraction of energy described by a plane wave decreases to 45% of its initial value.

- The shear at the base of the mixed layer decreases by a factor of about 5 during this period.

Several simple tests of linear dynamics can be made on these data:

- The vertical propagation and frequency of the Beam are consistent with WKB ray theory, although the error bars are large.

- The decrease in total water column inertial energy is consistent with southward propagation of the lowest few baroclinic modes out of the generation region.

- The mesoscale (50 km) variations in inertial phase are at least a factor of 4 less than would be expected from the vorticity of the mesoscale eddy field in which the inertial currents evolve.

- The large decrease in shear is inconsistent with linear theory.

Acknowledgments. EAD thanks Jim Overland, Nick Bond, and Mel Shapiro for invaluable help in using the NOAA P-3; the forecasters of the National Weather Service of the United States, and of Environment Canada for our weather briefings; Stig Rossby and the NOAA P-3 crew for excellent flying under adverse conditions. Mark Morehead and Mike Horgan did an excellent job preparing the AXCPs for flights. Tom Sanford provided the original motivation for this experiment as well as invaluable scientific and technical advice. This work was supported by the Office of Naval Research, contracts N00014-84-C-0111 and N00014-87-K-0004 and grant N00014-90-J-1104.

APPENDIX

Simulation of Fitting Errors

The parameters of the wavenumber fit (2) are determined by a nonlinear fit to the data as described in Part I. Their errors are determined by a Monte Carlo simulation. The fitting procedure is simulated by generating realizations of U_R with a correlation function similar to that found for the real U_R. Figure A1 shows the correlation function averaged over data from 55 to 175 m (circles). This is simulated by generating a field of complex Gaussian random numbers with expected variance at each depth determined by $|U_R|^2$ computed from the fit of (2). These are then smoothed with splines (Craven and Wahba 1979) with a smoothing parameter of 1000 m to generate synthetic realizations of U_R. The correlation function of these realizations is close to that of the data both in the 55–175 m depth range (Fig. A1) and below (not shown). These U_R are used to generate synthetic data which are then fit to form Monte Carlo realizations of the data. As in Part I, the variance of U_R appears to be spatially variable, but not so much that it could not be a realization of this model.

REFERENCES

Craven, P., and G. Wahba, 1979: Smoothing noisy data with spline functions: Estimating the correct degree of smoothing by the method of generalized cross validation. *Numer. Math.*, **3**, 377–403.

Crawford, G. B., and W. G. Large, 1994: (this volume).

D'Asaro, E. A., 1989: The decay of wind-forced mixed layer inertial oscillations due to the β effect. *J. Geophys. Res.*, **94**, 2045–2056.

———, 1994a: Upper ocean inertial currents forced by a strong storm, III: Modeling. (this volume)

———, 1994b: Observations and dynamics of small-scale, storm-forced inertial frequency currents. (this volume)

———, and M. D. Morehead, 1991: Internal waves and velocity fine structure in the Arctic Ocean. *J. Geophys. Res.*, **96**, 12,725–12,738.

———, and H. Perkins, 1984: A near-inertial internal wave spectrum for the Sargasso Sea in late summer. *J. Phys. Oceanogr.*, **14**, 489–505.

———, T. B. Sanford, R. G. Drever, M. D. Morehead, and G. L. Welsh, 1990: Air

expendable current profiling during the OCEAN STORMS experiment, Technical Report, APL-UW TR 8916, Applied Physics Laboratory, University of Washington, Seattle.

———, P. Van Meurs, R. E. Davis, and P. P. Niiler, 1994: Upper ocean inertial currents forced by a strong storm, I: Mixed layer. (this volume)

Davis, R. E., R. de Szoeke, D. R. Halpern, and P. P. Niiler, 1981: Variability in the upper ocean during MILE, Part I, The heat and momentum balances. *Deep-Sea Res.*, **28**(12A), 1427–1451.

———, C. C. Eriksen, M. D. Levine, W. G. Large, and E. A. D'Asaro, 1994: *(instrumentation; this volume)*

Eriksen, C. C., J. M. Dahlen, J. T. Shillingford, Jr., 1982: An upper ocean moored current and density profiler applied to winter conditions near Bermuda. *J. Geophys. Res.*, **87**, 7879–7902.

Gill, A. E., 1984: On the behavior of internal waves in the wakes of storms. *J. Phys. Oceanogr.*, **14**, 1129–1151.

Kennelly, M. A, J. H. Dunlap, T. B. Sanford, E. L. Kunze, M. D. Prater, and R. G. Drever, 1989: The Gulf of Cadiz Expedition: R/V *Oceanus* Cruise 202. Report APL-UW

TR 8914, Applied Physics Laboratory, University of Washington, Seattle.

Kunze, E., 1985: Near-inertial wave propagation in geostrophic shear. *J. Phys. Oceanogr.*, **15**, 544–565.

Matear, R.J., 1993: Circulation within the Ocean Storms area located in the northeast Pacific Ocean determined by inverse methods. *J. Phys. Oceanogr.*, **23**, 648–658.

Munk, W., and N. Phillips, 1968: Coherence and band structure of inertial motions in the sea. *Rev. Geophys.*, **6**, 447–472.

Paduan, J.D., and P.P. Niiler, 1993: Structure of velocity and temperature in the northeast Pacific as measured with Lagrangian drifters in fall 1987. *J. Phys. Oceanogr.*, **23**, 585–600.

Pollard, R.T., 1970: On the generation by winds of inertial waves in the ocean. *Deep-Sea Res.*, **17**, 795–812.

———, and R.C. Millard, Jr., 1970: Comparison between observed and simulated wind-generated inertial oscillations. *Deep-Sea Res.*, **17**, 813–821.

Price, J.F., 1981: Upper ocean response to a hurricane. *J. Phys. Oceanogr.*, **11**, 153–175.

———, R. A. Weller, and R. Pinkel, 1986: Diurnal cycling: Observations and models of the upper ocean response to diurnal heating, cooling, and wind mixing. *J. Geophys. Res.*, **91**, 8411–8427.

Qui, H., R. A. de Szoeke, C. A. Paulson, and C. C. Eriksen, 1994: The structure of near-inertial waves during OCEAN STORMS. (this volume)

Sanford, T. B., R. G. Drever, J. H. Dunlap, and E. A. D'Asaro, 1982: Design, operation and performance of an expendable temperature and velocity profiler (XTVP). Report APL-UW 8110, Applied Physics Laboratory, University of Washington, Seattle, 164 pp.

———, P. G. Black, J. R. Haustein, J. W. Feeney, G. Z. Forristall, J. F. Price, 1987: Ocean response to a hurricane, Part I: Observations. *J. Phys. Oceanogr.*, **17**, 2065–2083.

Smith, R., 1973: Evolution of inertial frequency oscillations. *J. Fluid Mech.*, **60**, 383–389.

Tabata, S., L. A. F. Spearing, R. H. Bigham, B. G. Minkley, J. Love, D. Yelland, J. Linguanti, and P. M. Kimber, 1988: STP/hydrographic observations along Line P, Station P, Line R and associated lines, and in the "OCEAN STORMS" area. Canadian Data Report of Hydrography and Ocean Sciences, No. 70, 132 pp.

[Available from Institute of Ocean Sciences and Department of Fisheries and Oceans, Sidney, B.C.]

Webster, F., 1968: Observations of inertial-period motions in the deep sea. *Rev. Geophys.*, **6**, 473–490.

Zervakis, V., and M. D. Levine, 1994: (this volume).

Figure Captions

FIG. 1. Location of OCEAN STORMS moored array (triangles) including ADCP moorings (C, N, E, W, S), PCM mooring, and OSU mooring. The 25 October AXCP drops (filled circles) are in three sections labeled A, B, and C.

FIG. 2. Inertial currents at ADCP mooring C before (top) and after (bottom) removal of mooring motion. The errors due to mooring motion show up primarily below the mixed layer near day 278.

FIG. 3. Horizontal kinetic energy spectra from current meters on OSU mooring at 59 m, 79 m, 99 m, 119 m, 139 m, 159 m, 500 m, 1000 m, 2000 m, 3000 m, and 4000 m for days 278–304. The spectra are computed from 6-day-long, half-overlapped pieces windowed with a half-cosine.

FIG. 4. Partition of horizontal kinetic energy by subinertial, inertial, and superinertial frequency bands in the upper (top panel) and deep ocean (bottom panel). Below 59 m, spectra from currents meters on the OSU mooring for days 277–304 are used. The inertial band is 1.33–1.66 cpd. In the mixed layer, data from surface drifters are used. Their decomposition into inertial and subinertial energy is described in Part I. The mixed layer superinertial energy is taken from the 59 m deep current meter on the OSU mooring.

FIG. 5. Data from PCM mooring. (a) Backrotated inertial vectors with contours of inertial speed. Speeds greater than 0.15 m s^{-1} are shaded; contour interval = 0.05 m s^{-1}.

(b) Backrotated inertial vectors, shading from (a), with contours of backrotated inertial direction; contour interval = 22.5°. (c) Density contours; interval = 0.05 kg m^{-3}. (d) Temperature contours; interval = 0.25°.

FIG. 6. OSU moored data. (a) Backrotated inertial vectors with contours of inertial speed, 0–200 m. Speeds greater than 0.15 m s^{-1} are shaded; contour interval = 0.05 m s^{-1}. (b) Backrotated inertial vectors, shading from (a), with contours of backrotated inertial direction; contour interval = 22.5°. (c) Backrotated inertial vectors with speed contours, 200–4200 m. Speeds greater than 0.04 m s^{-1} are shaded; contour interval = 0.025 m s^{-1}. (d) Temperature contours; interval = 0.25°.

FIG. 7. Backrotated inertial vectors with speed contours from ADCP C. Speeds greater than 0.15 m s^{-1} are shaded; contour interval = 0.05 m s^{-1}.

FIG. 8. As in Fig. 7 but for ADCP N.

FIG. 9. As in Fig. 7 but for ADCP W.

FIG. 10. As in Fig. 7 but for ADCP E.

FIG. 11. Backrotated inertial vectors from fit of (2) to five ADCP moorings. (a) Vectors and speed contours. Speeds greater than 0.15 m s^{-1} are shaded; contour interval = 0.05 m s^{-1}. (b) Vectors, shading from (a), and direction contours; contour interval = 22.5°.

FIG. 12. Wavenumbers from fit of (2) to five ADCP moorings (a) k (light) and l (heavy) in mixed layer (25–50 m). (b) Same but below mixed layer (70–100 m). Dashed line has slope of $-\beta$ and a level that fits the l wavenumber for all surface drifters in Part I. Heavy error bars are k and l in the appropriate depth range of Fig. 20.

FIG. 13. Backrotated inertial shear vectors computed from vectors in Fig. 11. Shear vectors and contours of shear magnitude are plotted. Shear magnitudes greater than 2×10^{-2} s^{-1} are shaded. Contour interval = 5×10^{-3} s^{-1}.

FIG. 14. Backrotated inertial vectors from AXCP and moored data on 25 October, day 298, at 80 m (light, small arrowhead), 100 m (heavy, medium arrowhead), and 40 m (light, large arrowhead). Contours of direction at 100 m; contour interval = 22.5°. Shaded contours of speed at 100 m; contour interval = 0.1 m s^{-1}; shading starts at 0.1 m s^{-1}.

FIG. 15. Backrotated inertial vectors on day 298 interpolated to section A (see Fig. 1) in upper 300 m. Triangles show the projected location of all data within 20 km of the section. Moorings are labeled. The size of the triangle indicates the perpendicular distance. (a) Vectors with speed contours. Speeds greater than 0.15 m s^{-1} are shaded; contour interval = 0.05 m s^{-1}. (b) Vectors, shading from (a), and direction contours; contour interval = 22.5°.

FIG. 16. Backrotated inertial vectors on day 298 interpolated to section B (see Fig. 1).

FIG. 17. Backrotated inertial vectors on day 298 interpolated to section C (see Fig. 1).

FIG. 18. Backrotated inertial vectors from AXCP and moored data on 25 October, day 298, at 100 m (light, small arrowhead), 250 m (heavy, medium arrowhead), and 700 m (light, large arrowhead).

FIG. 19. Fit of (2) to backrotated inertial vectors on day 298. Fit parameters include the fit energy (top panel, shaded); the total energy (top panel, line); the fit phase (top panel, heavy line); east-west wavenumber (k, middle panel light); north-south wavenumber (l, middle panel heavy); and number of data points in fit (bottom panel). The dots and pluses are same parameters fit to 50 realizations of a Monte Carlo simulation of the data errors.

FIG. 20. Contours of f_{eff} (light) from vorticity field computed in Part I and inertial direction (heavy) from Fig. 14. Contour interval of f_{eff} (0.2% f_0) is chosen so that if (5) were correct the heavy and dark contours would coincide.

FIG. A1. Lagged longitudinal (heavy line, o) and transverse (light line, +) for fit residual averaged from 55 m to 175 m. Symbols are for data; lines and 95% confidence limits are from Monte Carlo realization.

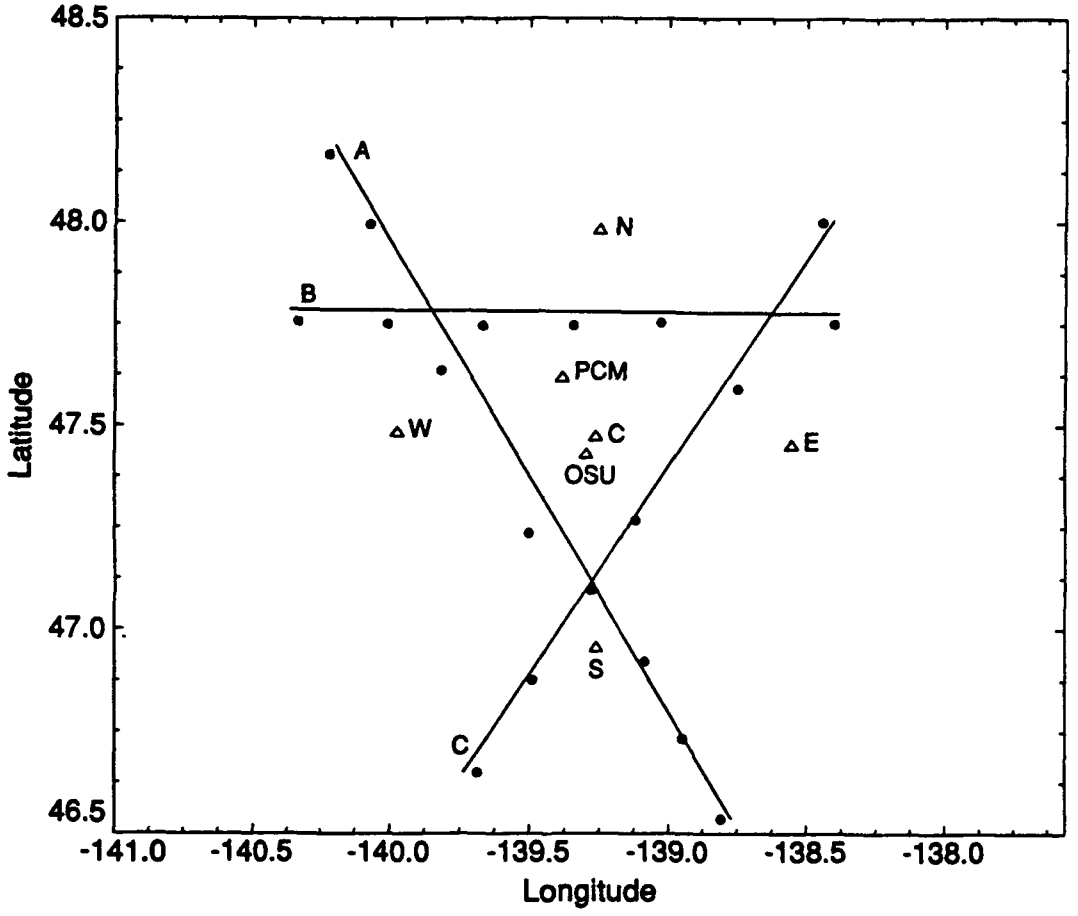

D'Asaro et al., Part II, Fig. 1

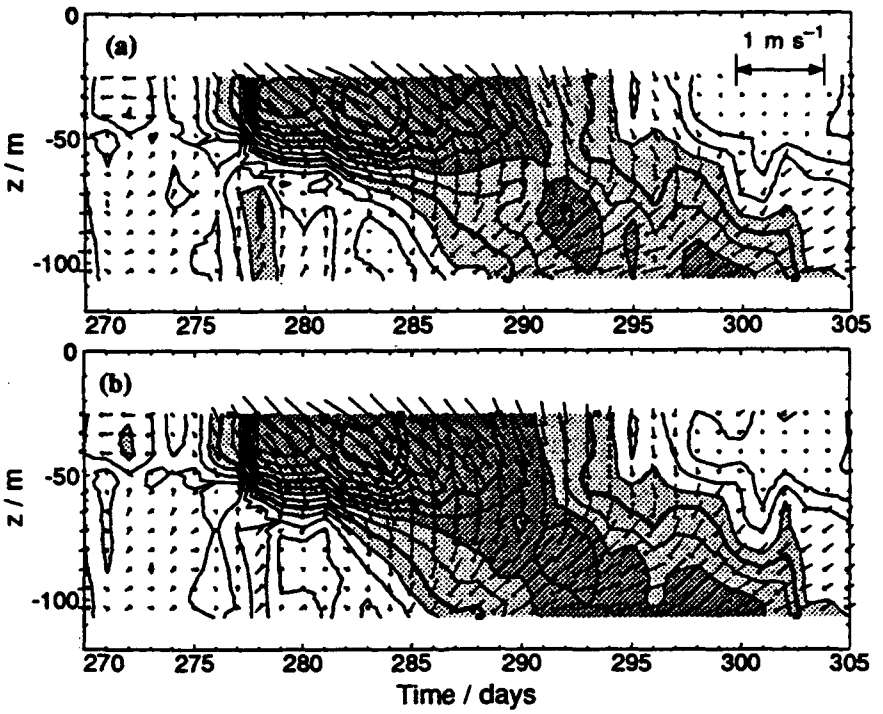

D'Asaro et al., Part II, Fig. 2

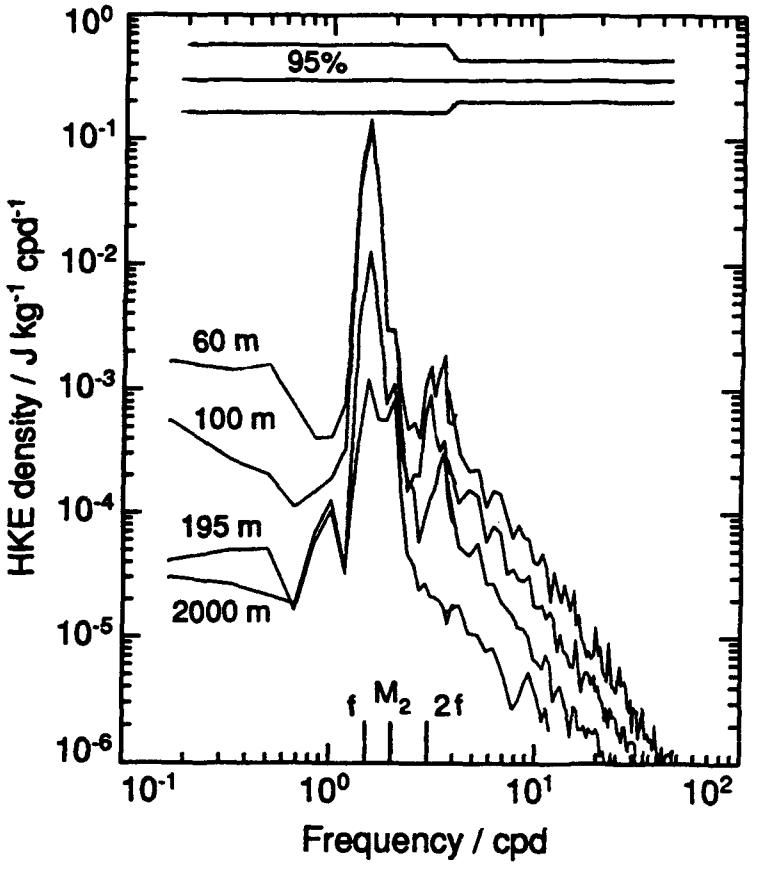

D'Asaro et al., Part II, Fig. 3

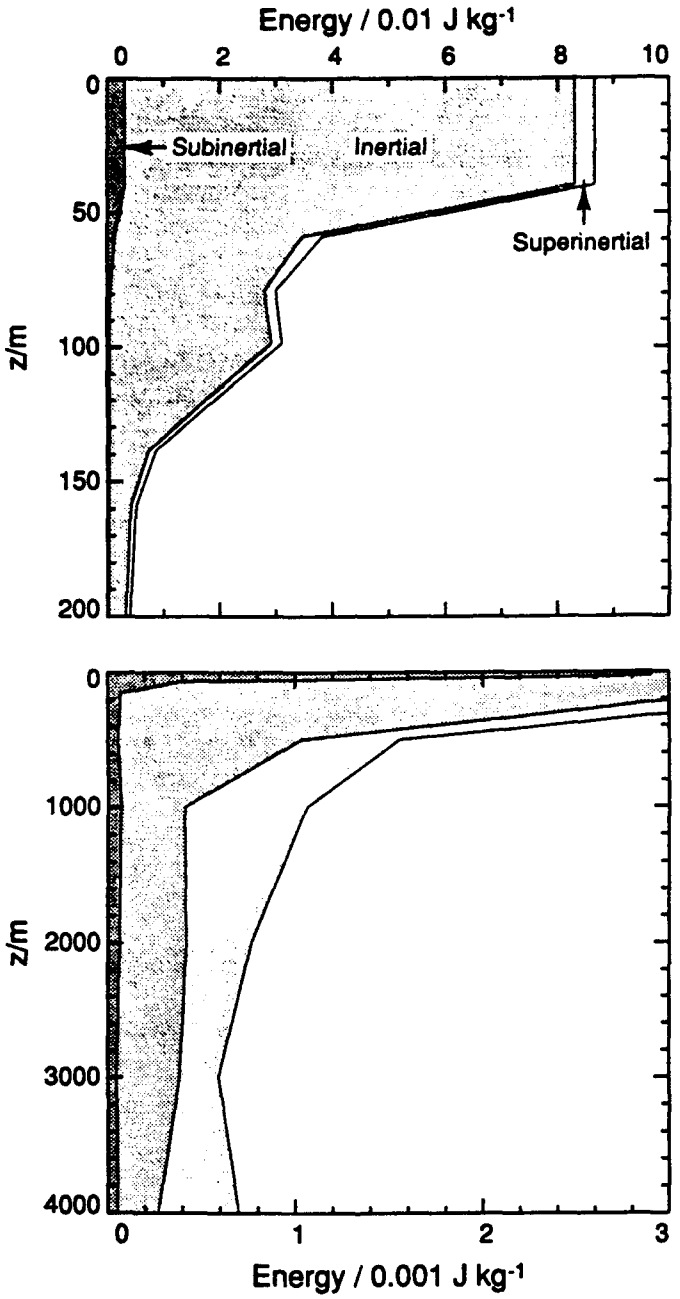

D'Asaro et al., Part II, Fig. 4

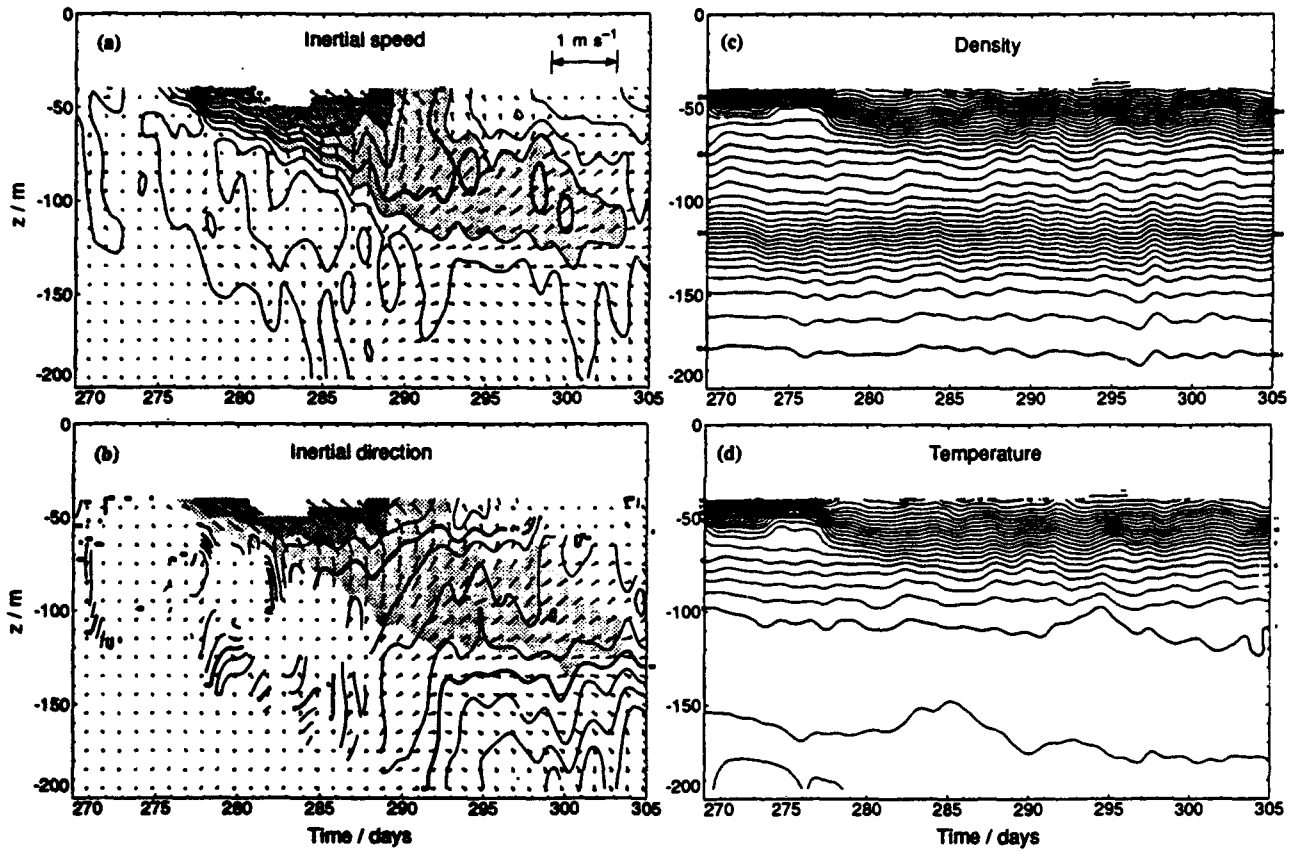

D'Asaro et al., Part II, Fig. 5

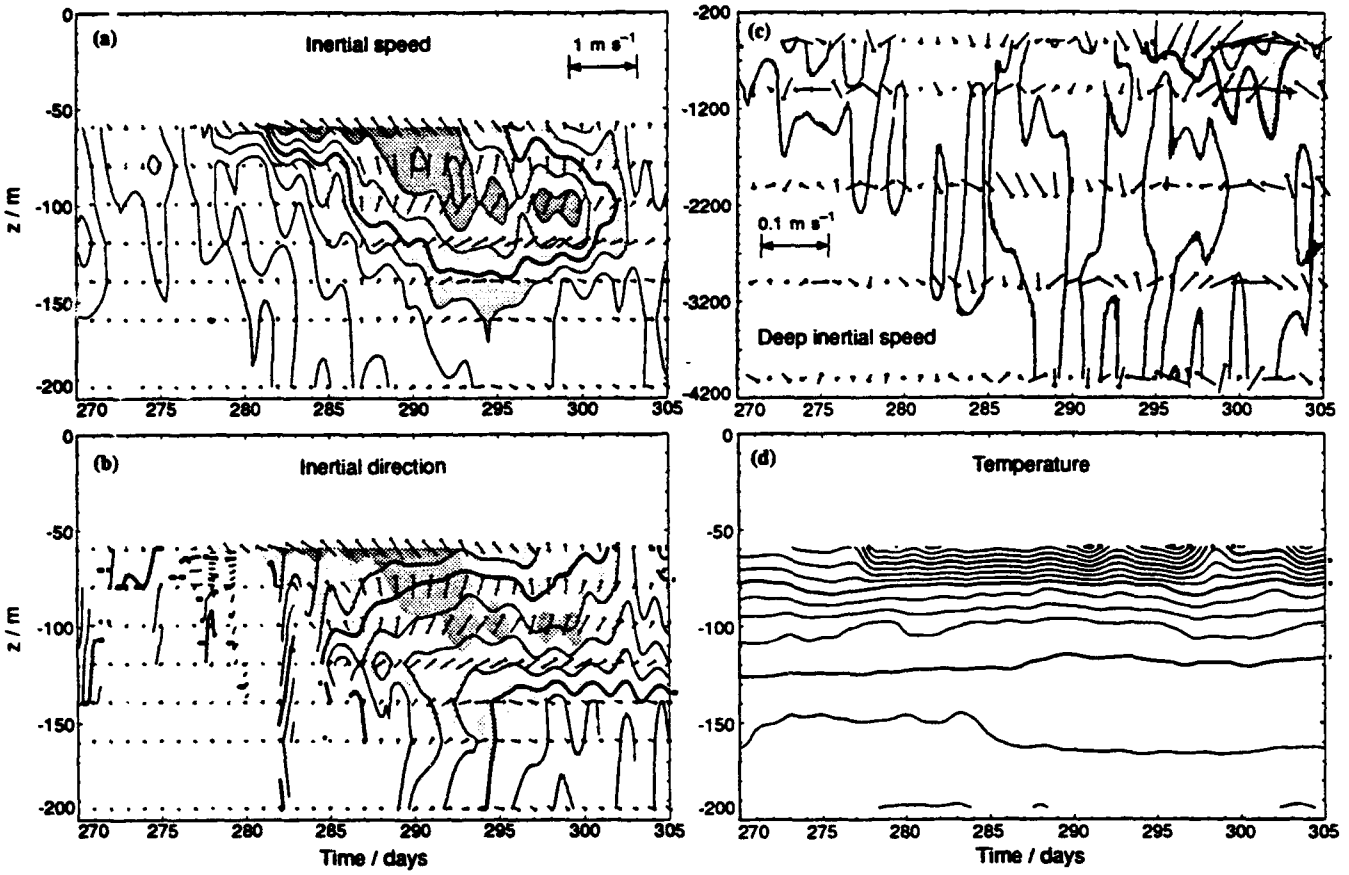

D'Asaro et al., Part II, Fig. 6

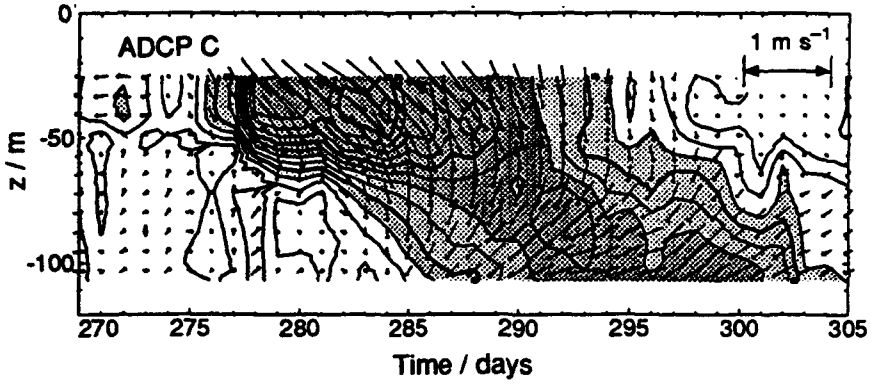

D'Asaro et al., Part II, Fig. 7

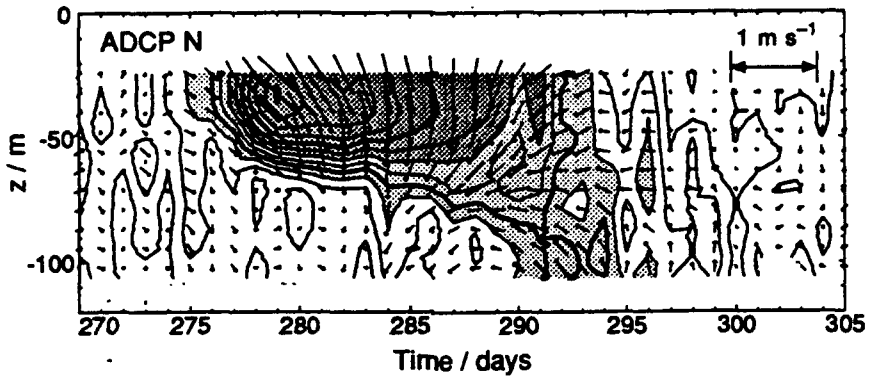

D'Asaro et al., Part II, Fig. 8

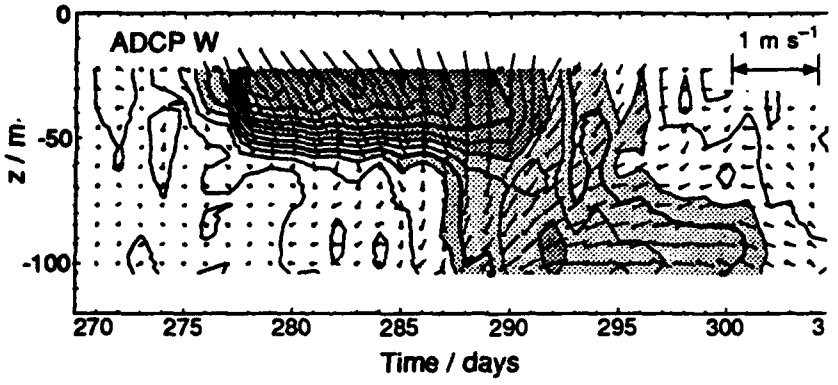

D'Asaro et al., Part II, Fig. 9

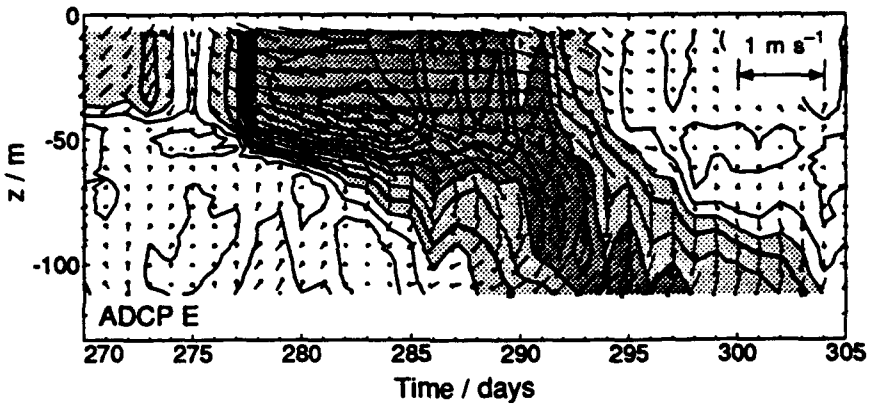

D'Asaro et al., Part II, Fig. 10

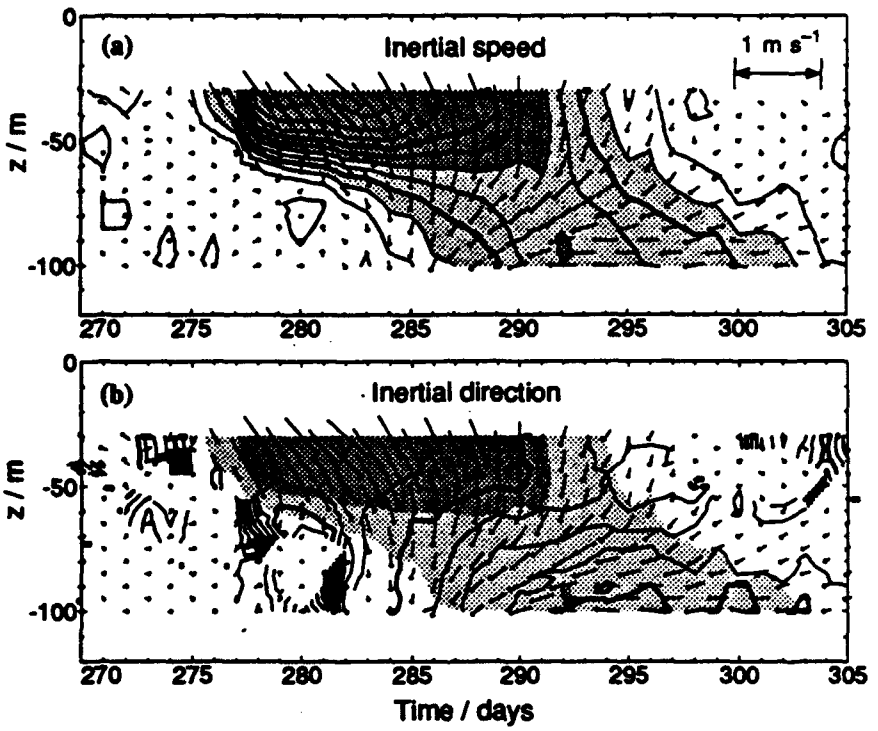

D'Asaro et al., Part II, Fig. 11

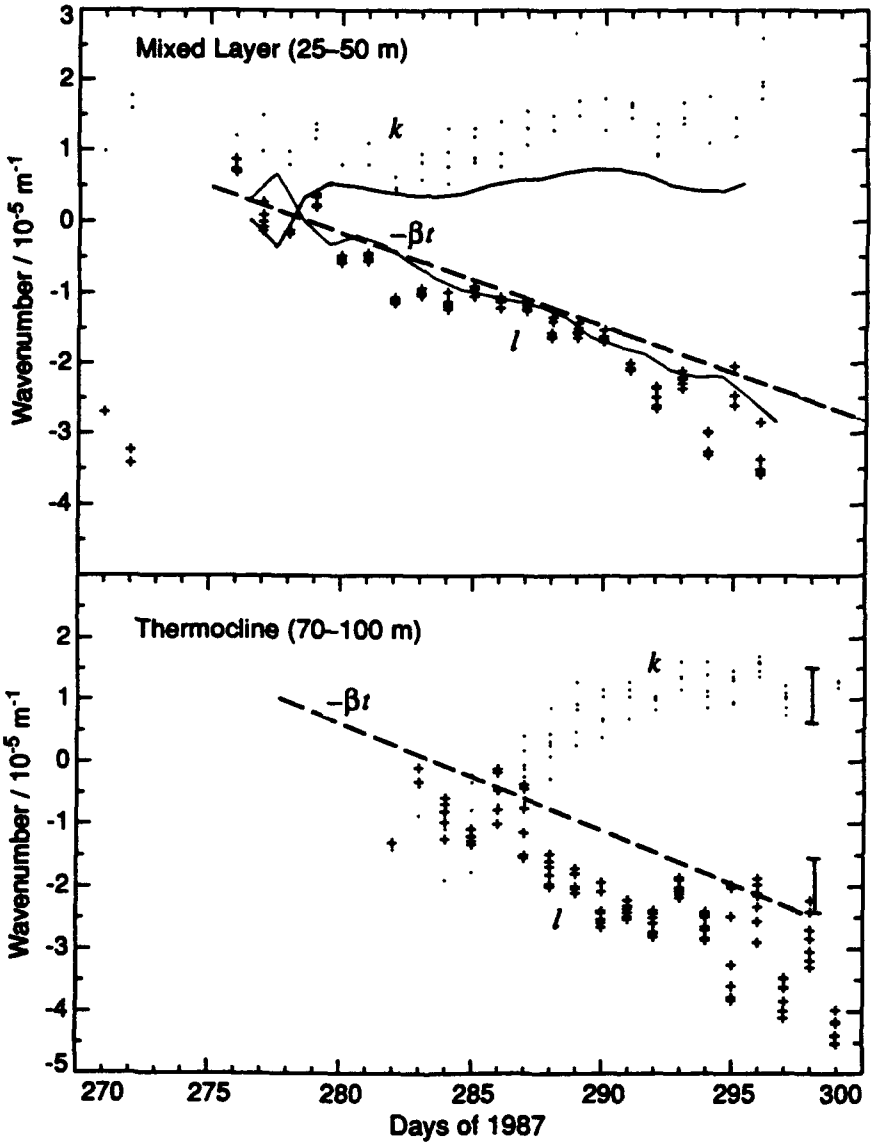

D'Asaro et al., Part II, Fig. 12

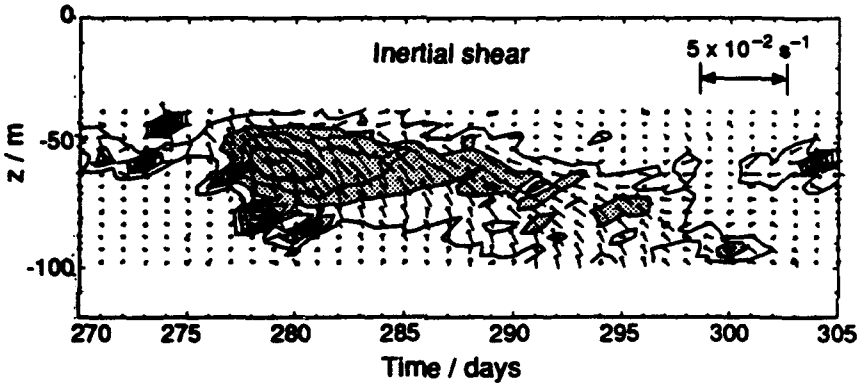

D'Asaro et al., Part II, Fig. 13

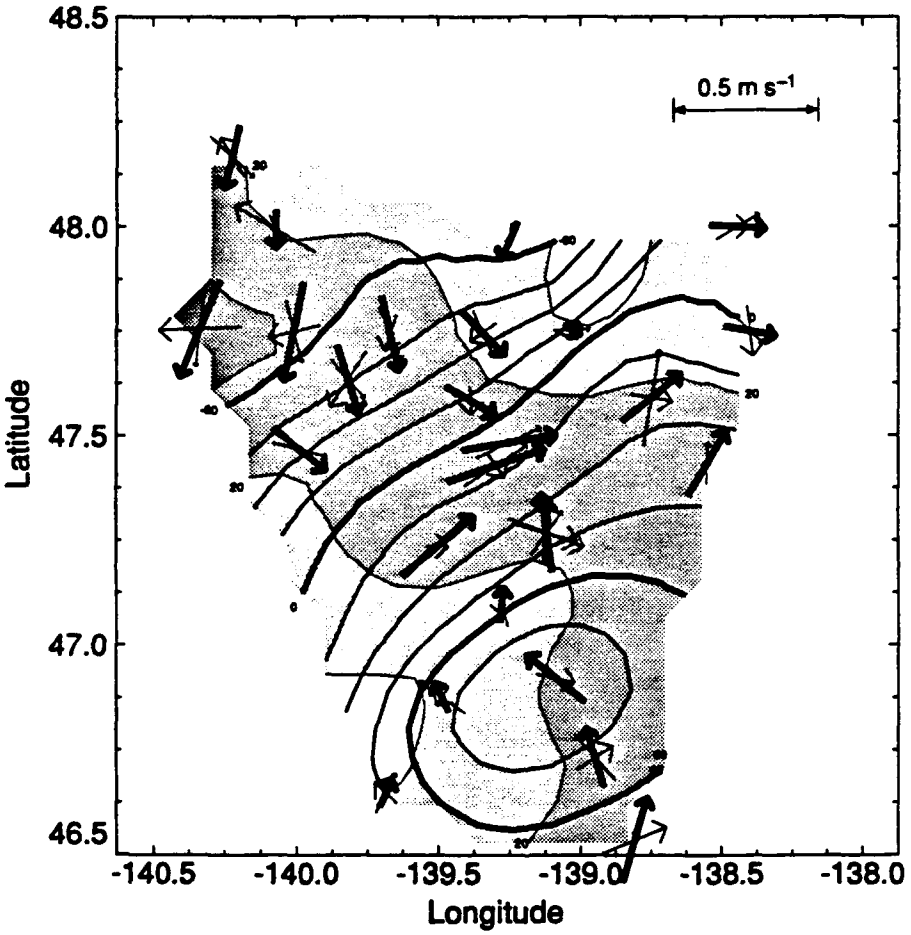

D'Asaro et al., Part II, Fig. 14

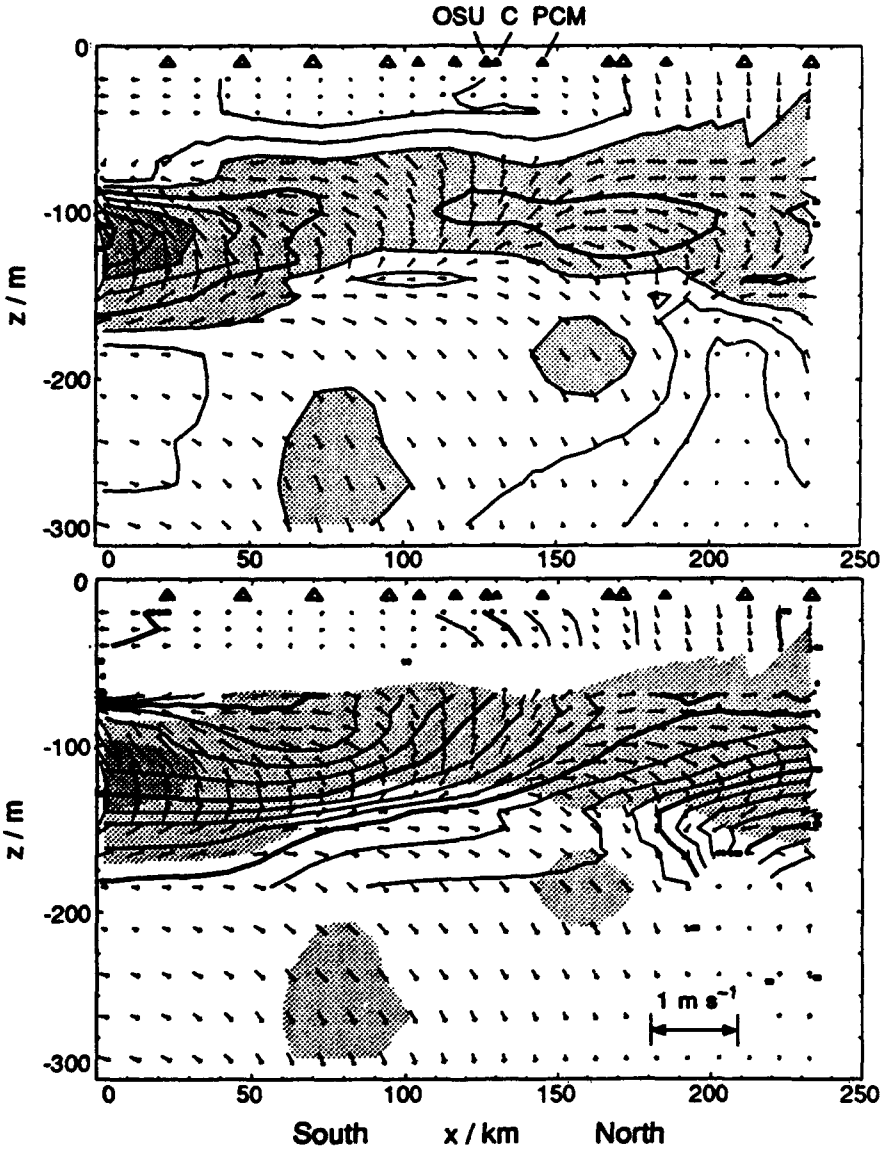

D'Asaro et al., Part II, Fig. 15

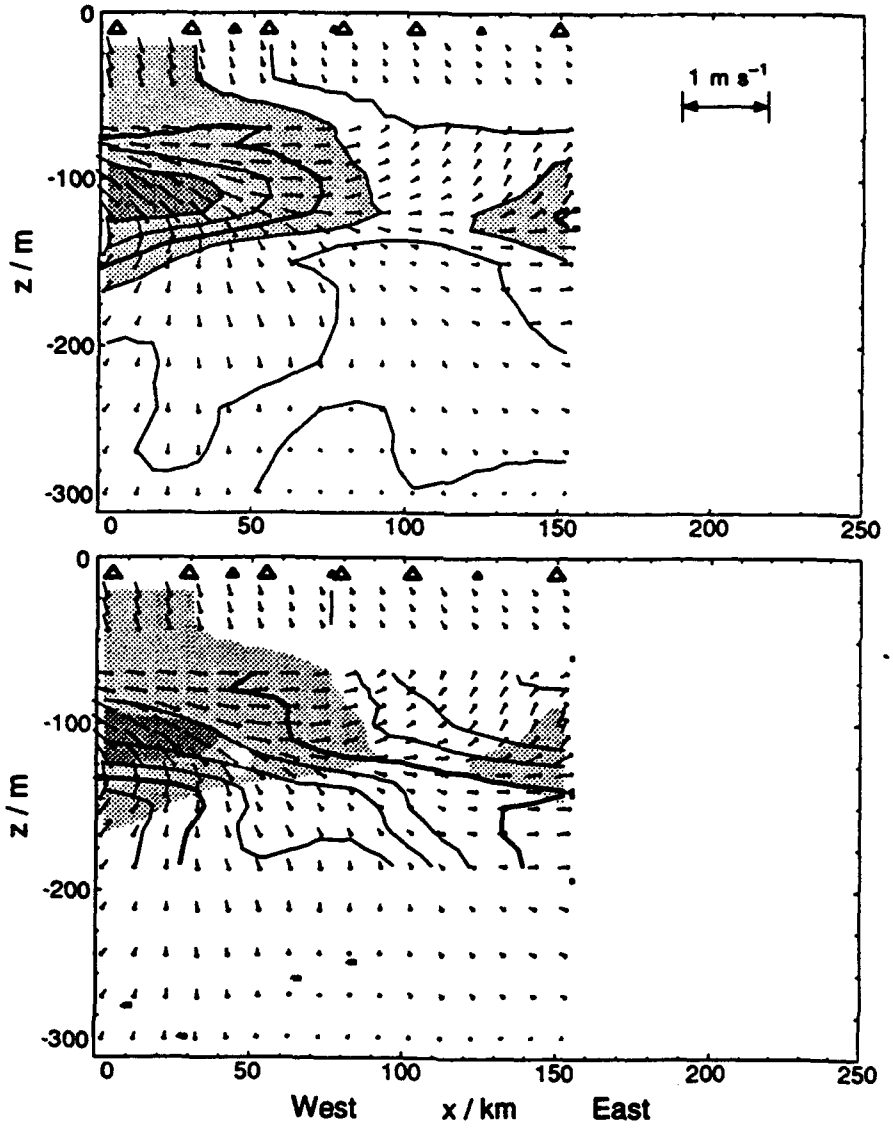

D'Asaro et al., Part II, Fig. 16

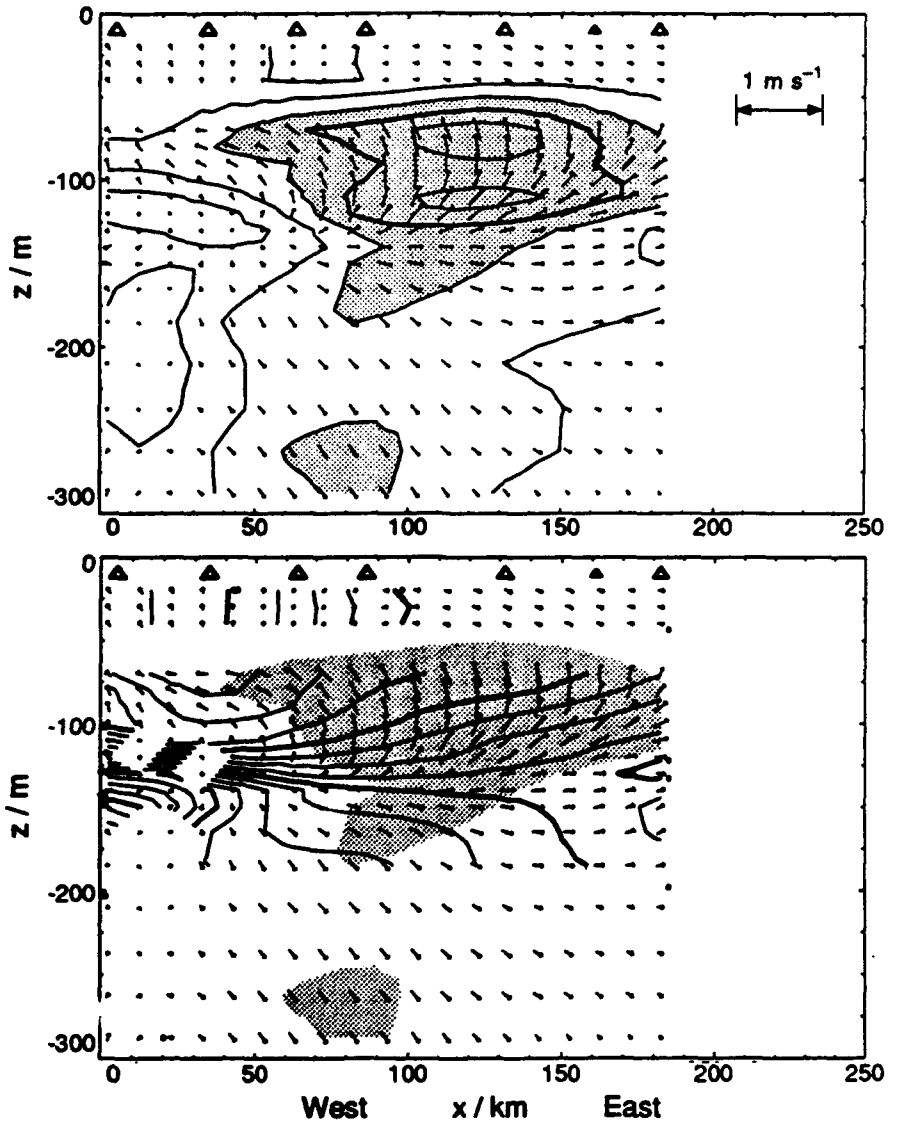

D'Asaro et al., Part II, Fig. 17

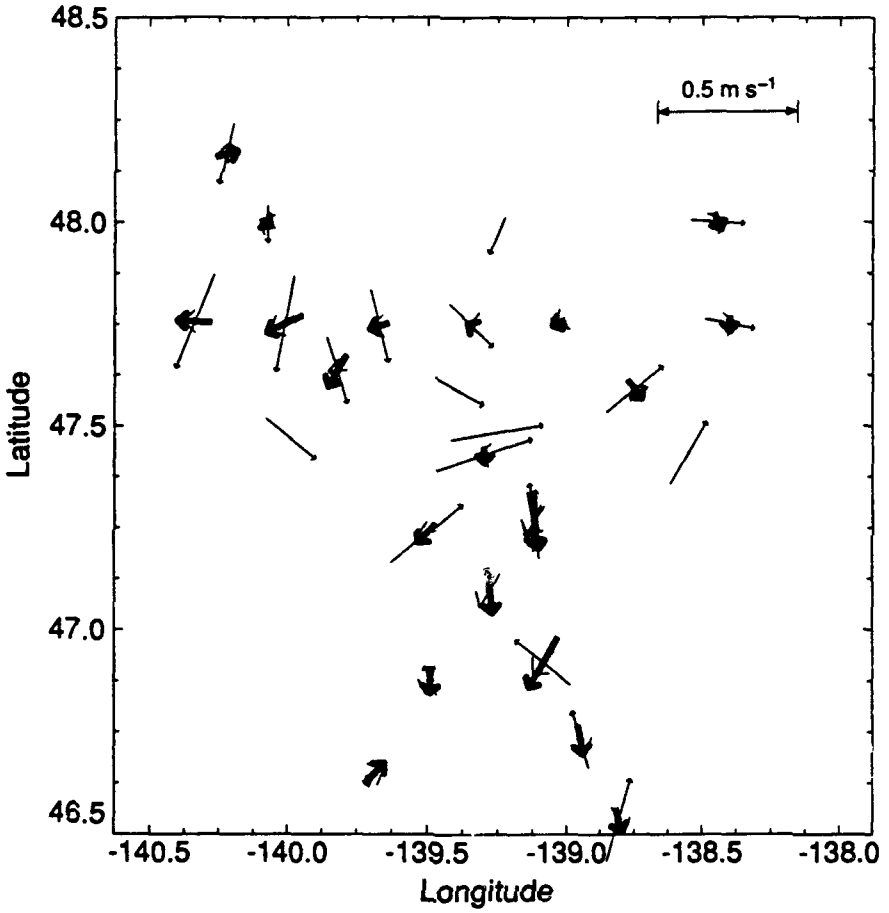

D'Asaro et al., Part II, Fig. 18

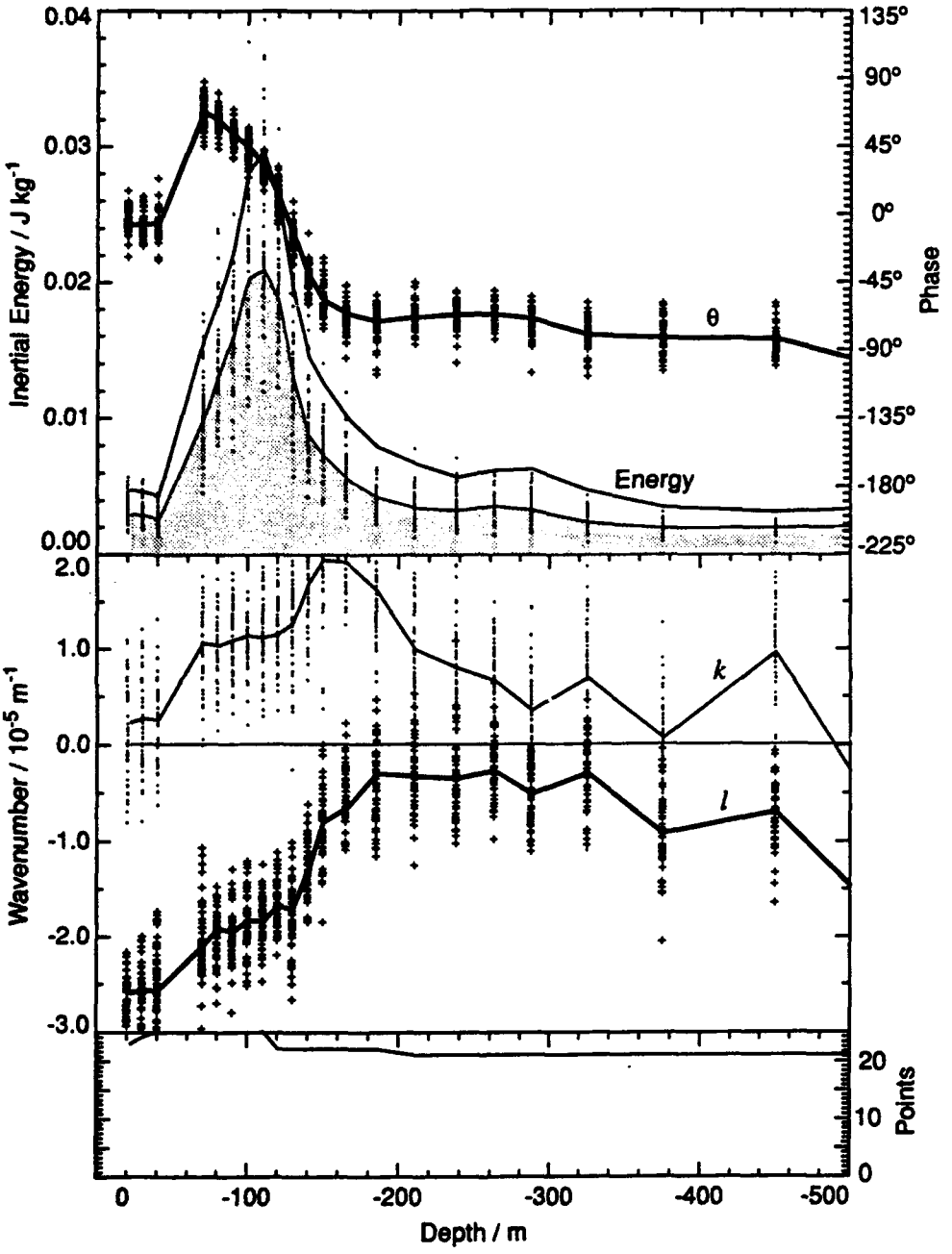

D'Asaro et al., Part II, Fig. 19

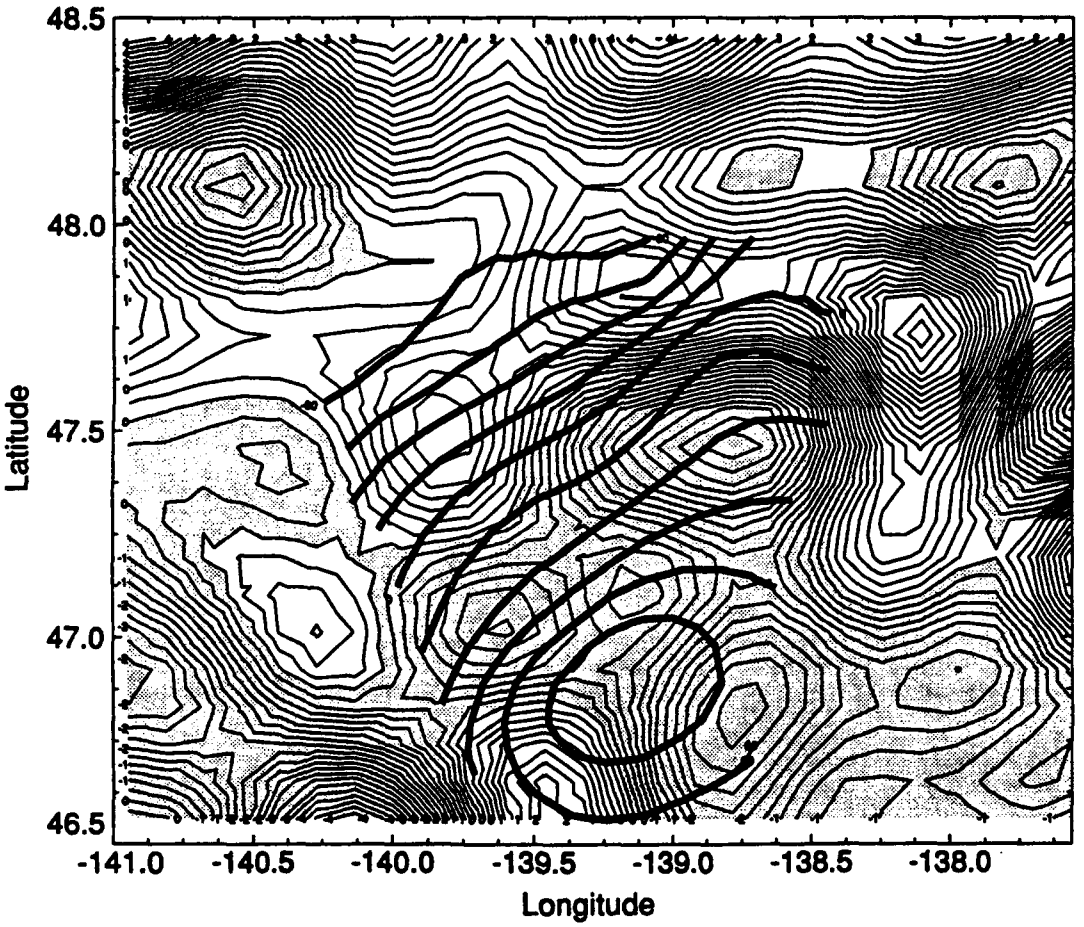

D'Asaro et al., Part II, Fig. 20

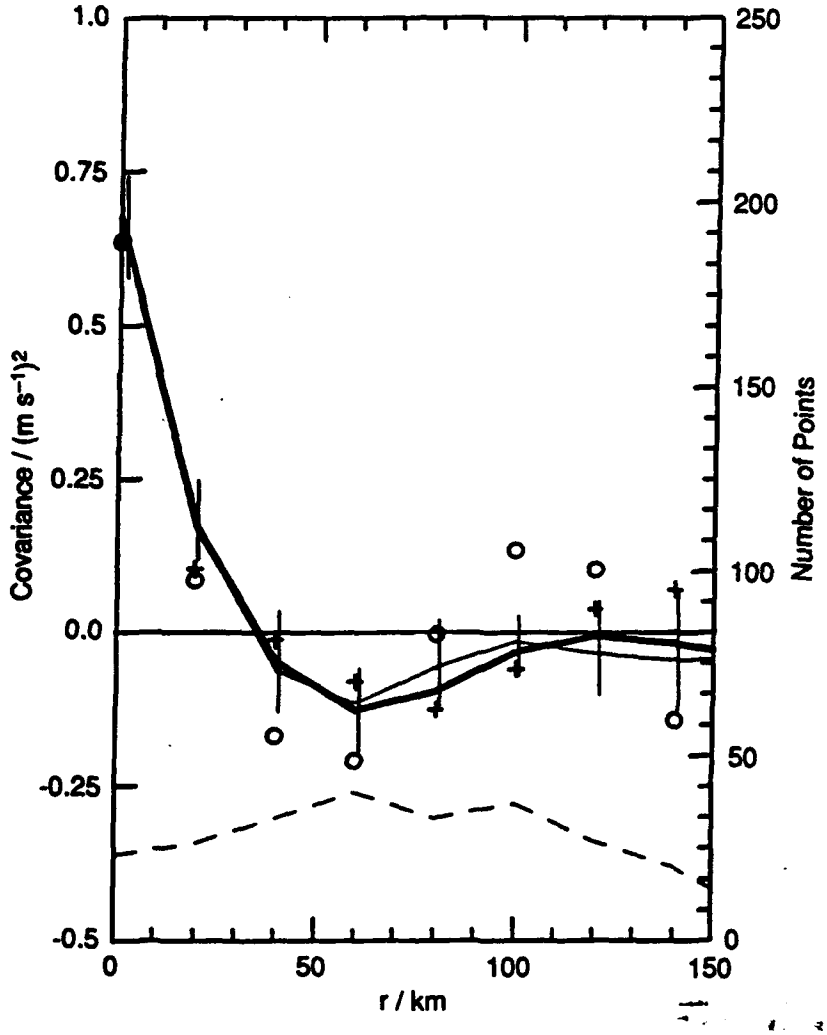

D'Asaro et al., Part II, Fig. A1